UNIVERSITY OF COPENHAGEN

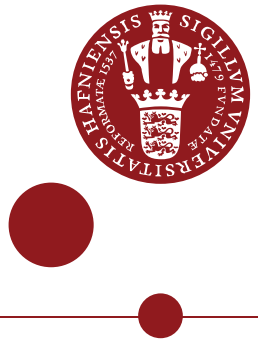

MSc in Physics

Mass and Magnification in Abell 370

Updating the lens model of a Hubble Frontier Fields galaxy cluster with JWST

Rachel Gledhill

Supervised by Gabriel Brammer and Victoria Strait

June 2023

Rachel Gledhill
Mass and Magnification in Abell 370
MSc in Physics, June 2023
Supervisors: Gabriel Brammer and Victoria Strait

University of Copenhagen
The Cosmic DAWN Centre
MSc in Physics
Jagtvej 128
2200 Copenhagen N

Abstract

Gravitational lensing in galaxy clusters is a powerful tool with which to study both the large scale mass distribution of some of the most massive structures in the Universe and the magnified galaxies in their backgrounds. In this thesis, I will present a new parametric lens model of the matter distribution in the galaxy cluster Abell 370 made using new data from the James Webb Space Telescope. I use NIRCAM and NIRISS data to evaluate the systems of multiple images of background galaxies and discuss how they have been changed and improved by JWST. I use these systems as strong lensing constraints to construct a lens model. Using a magnification map derived from the model, I also discuss the properties of a newly spectroscopically confirmed multiply imaged galaxy at z=7.69. I constrain its properties with SED fitting and discuss the impact of different prior assumptions on the results.

Acknowledgements

First and foremost, I want to express my deepest gratitude to my advisor, Victoria Strait for all of her excellent guidance while working on this thesis. She has been unwaveringly patient and I am immensely grateful to her for challenging and encouraging me through this process. I couldn't have asked for a better advisor.

I also want to thank Gabe Brammer for his valuable feedback during this thesis, and also for his work on the data reduction and processing pipelines, without which this project would not have been possible.

I would like to express my sincere appreciation for the CANUCS team for including me in their meetings and allowing me access to the JWST data. Special thanks is owed to the gravitational lensing team: Guillaume Desprez, Maruša Bradač, Gregor Rihtarsic, and Nicholas Martis, who were so generous with their time and advice while I was working on my lens model. I feel privileged to have been able to learn from so many excellent scientists.

Finally, I want to thank my husband Luke for all his support, care, and patience during this degree. He believed in me even when I didn't and I truly could not have done this without him.

Contents

List of Figures

List of Tables

1 Introduction

Gravitational lensing is the effect in which light is deflected around large concentrations of mass. Galaxy clusters are some of the most massive structures in the Universe and the path light takes around them is a powerful tool used to learn about the distribution of mass in a cluster. It is estimated that on average, galaxy clusters are made of ∼15% baryonic matter in stars, gas, and dust, and 85% non-baryonic dark matter. Light from background galaxies is deflected by the mass of the cluster, which can create multiple magnified images of a single galaxy around the cluster. The type of matter in the cluster makes no difference to the deflection, making it possible to use this effect to study the total mass distribution, including galaxies, intracluster stars, gas, dust, and dark matter. Lens modelling clusters allows us to estimate the total mass and draw conclusions about where the mass is distributed in the cluster.

Lensing in clusters is also a powerful way to study some of the most distant galaxies in the Universe. Galaxies behind the cluster are magnified as they are lensed, making them brighter and more spatially resolved. The lensing effect does not depend on wavelength, which allows us to take spectra of objects that appear brighter than they would be without lensing. This helps us observe more galaxies in more detail and expands our understanding of the overall population of galaxies at high redshift. When we plot the luminosity function (the number density of galaxies as a function of UV absolute magnitude), we find that faint galaxies are far more abundant than bright galaxies at all redshifts. Without being magnified by a galaxy cluster, many faint galaxies would not be visible. Before properties such as stellar mass and star formation rate can be estimated, it is necessary to derive the magnification of the source using a lens model (Schneider, 2006, Strait *et al.*, 2018).

Abell 370, a galaxy cluster with a redshift of z=0.375, is one of the most massive galaxy clusters (e.g. Umetsu *et al.*, 2011). It is non-spheroidal in shape with two large galaxies at its centre and is believed to be the result of two galaxy clusters of approximately equal size merging together (e.g. Molnar

et al., 2020). As such, it has a more complex structure than many other clusters (e.g. Allingham *et al.*, 2023, Mahler *et al.*, 2023) - previous studies (e.g. Strait *et al.*, 2018, Lagattuta *et al.*, 2019) have found that it requires at least two large concentrations of dark matter to model the mass distribution in Abell 370. It is also one of the clusters with the largest number of multiple image lensing systems, which are used as constraints when lens modelling (e.g. Lagattuta *et al.*, 2019). For these reasons, creating a lens model for Abell 370 is not a trivial task.

The James Webb Space Telescope (JWST) can observe distant galaxies with better resolution and sensitivity than previous instruments, on top of its spectroscopic capabilities in the infrared that will enable detailed studies of many more sources than previously possible. In this project I create a lens model of Abell 370 using new observations from JWST, improving it from previous versions which used only images from the Hubble Space Telescope (HST) and Spitzer. I also use new photometry and slitless spectroscopy from JWST to explore the properties of a lensed background source in the early Universe, demonstrating the power of lensing to observe distant galaxies.

Theory

2

2.1 Gravitational lensing

Gravitational lensing is the effect in which light is deflected around large concentrations of mass. The idea that if light could be considered a particle, its trajectory could be changed by a gravitational field was first proposed in 1784 (Michell, 1784). When Albert Einstein described general relativity, he calculated the angle by which light would be deflected by the mass of a star. However, he predicted that the separation would be far too small to be resolved (Einstein, 1936). Fritz Zwicky was the first to suggest, in 1937, that "extragalactic nebulae", i.e. galaxies, contain enough mass to produce resolvable images of lensed objects and predicted that these could be used to measure the mass of the galaxies (Zwicky, 1937a, Zwicky, 1937b).

The first gravitationally lensed object discovered was a quasar identified by Walsh *et al.* (1979). The two images were separated by 5.7 arcseconds and had identical spectra with a redshift of 1.4. Soon after, a small galaxy cluster between the two images was identified as the lens (Young *et al.*, 1988). Several more lensing systems were discovered by chance in the following decade, until systematic searches with HST revealed many more (Schneider *et al.*, 2006).

Another important discovery in lensing was the identification of giant luminous arcs; strongly curved features found in galaxy clusters, including Abell 370. Their nature was a mystery until a redshift measurement of one in 1988

(Soucail *et al.*, 1988) revealed that the redshift of the arc was much larger than that of the cluster. Smaller, less distorted images are called arcs or arclets.

According to general relativity, light travels along the null geodesics of space-time. For our purposes, however, we can describe light rays with an approximation called gravitational lens theory. Because the distances between the observer, lens, and source are so large, it is acceptable to describe light rays as straight lines, as illustrated in Fig. 2.1. There are two conditions for using this approximation.

First, the Newtonian gravitational field strength must be small. The field strength can be determined using the dimensionless ratio between the gravitational potential Φ and the speed of light c squared. If $\Phi/c^2 \ll 1$, then the field is weak. The virial theorem tells us that $\Phi \sim v^2$ for a mass distribution in equilibrium. Since a typical velocity for a galaxy in a cluster environment is 1000 km/s (Schneider, 2006), $v^2/c^2 \sim \Phi/c^2 \sim 10^{-5} \ll 1$. Therefore, under the conditions present in lensing clusters, this condition always holds.

The second condition is that the impact parameter ξ must be much larger than the Schwarzchild radius of the mass, R_S, defined in Equation 2.1. M is the mass that is causing the lensing, c is the speed of light, and G is Newton's gravity constant. The impact parameter ξ is defined as the perpendicular distance between the light ray and the lens in the lens plane.

$$R_S = \frac{2GM}{c^2}. \tag{2.1}$$

The deflection angle of a light ray passing by a spherically symmetric mass M is given by Equation 2.2.

$$\hat{\alpha} = \frac{4GM}{c^2\xi} \tag{2.2}$$

For gravitational lensing, the field equations of general relativity can be linearized. In this context, linearizing means that for an ensemble of mass points, the deflection angle is the vector sum of the deflections from each individual

mass. We can express this in terms of the surface mass density distribution Σ as shown in Equation 2.3.

$$\hat{\alpha}(\xi) = \frac{4G}{c^2} \int d^2\xi' \Sigma(\xi') \frac{\xi - \xi'}{|\xi - \xi'|^2} \tag{2.3}$$

A diagram of a simple lens system is shown in Fig 2.1. Light from a source at a distance of D_s is deflected by a mass distribution at a distance of D_d. D_{ds} is the distance between the two. The dashed line in the diagram is the optical axis, and the source and lens planes are defined as planes perpendicular to this line at their respective distances from the observer.

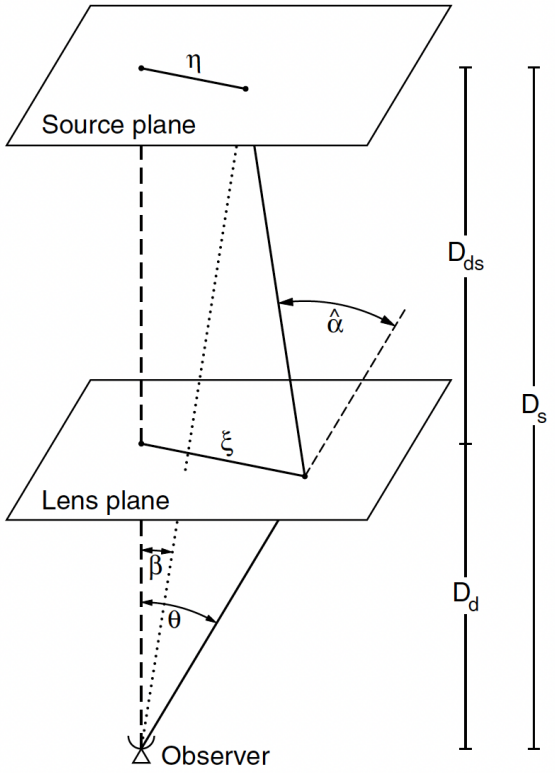

Figure 2.1: Diagram of a gravitational lens system (Schneider *et al.*, 2006)

The lens equation expressed in Equation 2.4 describes mapping the source's position in the lens plane θ to its position in the source plane β. The set of images in the lens plane that correspond to a single galaxy in the source plane is called a system.

$$\beta = \theta - \alpha(\theta) \tag{2.4}$$

$\alpha(\theta)$ is the scaled deflection angle, which can be expressed in terms of the surface mass density as follows,

$$\alpha(\theta) = \frac{1}{\pi} \int_{R^2} d^2\theta' \kappa(\theta') \frac{\theta - \theta'}{|\theta - \theta'|^2} \tag{2.5}$$

κ is called the convergence and is the dimensionless surface mass density, described in Equation 2.6.

$$\kappa(\theta) = \frac{\Sigma(D_d\theta)}{\Sigma_{cr}} \tag{2.6}$$

$$\Sigma_{cr} = \frac{c^2}{4\pi G} \frac{D_s}{D_d D_{ds}} \tag{2.7}$$

Σ_{cr} is the critical surface mass density and is a characteristic value for the surface mass density of the lens. If the lens mass distribution has $\Sigma > \Sigma_{cr}$ anywhere, then multiple images will be produced for some source positions and it is called a 'strong' lens.

Another way to describe the lens equation is shown in Equation 2.8. φ is called the lens potential and is related to the gravitational potential ϕ by Equation 2.9. Note that the lens potential is related to the distance to the source - background sources at different distances will have different deflection angles.

$$\beta = \theta - \nabla\varphi(\theta) \tag{2.8}$$

$$\varphi(\theta) = \frac{2}{c^2} \frac{D_{ds}}{D_s} \phi(\theta) \tag{2.9}$$

In the process of lensing, the images of the source are magnified. This is because the light rays from a source are differentially deflected - if we imagine a light beam passing through the lens plane, the light rays closer to the lens are deflected more than light rays further away. As a result, the solid angle subtended by the source changes. When the solid angle is larger, the surface brightness is preserved but the flux, which is the product of surface brightness and solid angle, increases.

A critical curve is the smooth line in the lens plane where the magnification diverges for a source at a given distance. The critical curve mapped back to the source plane is called a caustic and does not need to be smooth. The number of images and the degree of distortion in the images a source produces in the lens plane depends on its proximity to the caustic line in the source plane. Fig. 2.2 shows two analytical examples (1, 2) of a solution to the lens equation: an ellipsoidal mass distribution deflects the galaxies at the source plane positions in the cartoon on the right (b) such that they appear at the lens plane positions shown in the cartoon on the left (a). For more complicated mass distributions, this problem can only be solved numerically.

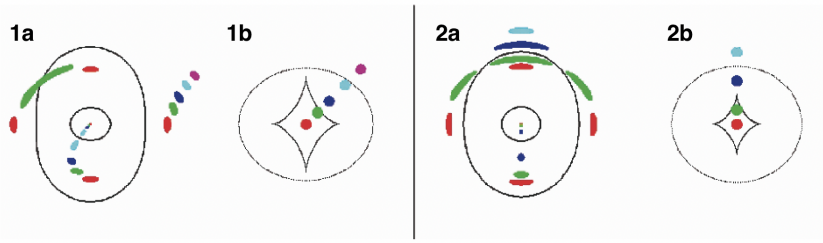

Figure 2.2: Two analytical examples of objects in the source plane (b) and their corresponding images in the lens plane (a). The surface mass density of the lens is ellipsoidal in this case. The lines represent caustics in the source plane and critical curves in the lens plane. Note that the green image closest to the caustic in both examples is the most distorted in the lens plane. By contrast, the points furthest from the centre of the mass distribution (purple in panel 1 and pale blue in panel 2) are not multiply imaged but simply distorted - at these positions in the lens plane $\Sigma < \Sigma_{cr}$ (Schneider, 2006).

The shape distortion of lensed images is caused by the tidal gravitational field and described by the shear γ, a complex quantity that can be related to the gravitational potential via the Jacobian matrix $\mathcal{A}$ shown in Equation 2.10.

$$\mathcal{A} = \frac{\delta\beta}{\delta\theta} = \begin{pmatrix} 1-\kappa-\gamma_1 & -\gamma_2 \\ -\gamma_2 & 1-\kappa+\gamma_1 \end{pmatrix} \tag{2.10}$$

$$\gamma = \gamma_1 + i\gamma_2 \tag{2.11}$$

The magnification of a source is the inverse of the determinant of the Jacobian (Equation 2.12). Note that the magnification can be positive or negative; this is called the 'parity' of an image. Another way to conceptualize the critical curve is that it is where $\det\mathcal{A} = 0$, causing the magnification to diverge. Note that the magnification does not truly diverge - infinite magnification is unphysical. However, the magnification can get very large as we approach the critical curve, on the order of 1000 times brighter. As we cross the critical curve, the parity flips. Two images on either side of a critical curve will be mirror images of each other.

$$\mu = \frac{1}{det\mathcal{A}} = \frac{1}{(1-\kappa)^2 - |\gamma|^2} \tag{2.12}$$

Lensing is an achromatic effect - the deflection of photons does not depend on their frequency.

A second type of lensing effect is weak lensing. In constrast to strong lensing, weak lensing does not produce mulitple images, but distorts a single image. This can be observed in the purple image in example 1 and the pale blue image in example b in Fig. 2.2 - there remains a single image in the lens plane but they are stretched into a different shape. Weak lensing generally occurs further away from the centre of the gravitational potential, where the magnification and distortion effects are weaker.

The deflection of light is determined by only the gravitational field through which the light propagates, making lensing just as sensitive to luminous matter as dark matter. Since the gravitational field is related to the mass distribution, lensing can provide great insight into how mass is distributed across a cluster.

2.2 Does light trace mass?

It is well established that galaxies contain more mass than is explainable by the stars, gas, and dust they contain. The same is true of galaxy clusters. The expected mass fractions in clusters is 2% stellar mass, 13% gas mass, and 85% non-baryonic dark matter (Umetsu *et al.*, 2022). The degree to which the total mass distribution of a galaxy cluster matches the distribution of its light-emitting matter is an area of active investigation.

A famous example is the Bullet Cluster, a merging cluster at z = 0.296. Shown in Fig. 2.3, the cluster has two main galaxy concentrations, separated by 0.72 Mpc. The majority of the cluster's baryonic mass is in intracluster gas detected via X-ray observations with Chandra (Markevitch, 2006). These observations show that the highest concentrations of gas are significantly offset from the galaxies. However, lens modelling analysis shows that the total mass distribution follows the galaxies quite closely, with the centres significantly separated from the gas (Bradač *et al.*, 2006, Clowe *et al.*, 2004).

The theory behind this is that during the merger, the two clusters passed through each other. While the galaxies act as collisionless particles, the gas experienced drag during the collision, pulling it towards the centre. Though the intracluster gas is far more massive than the stars in the galaxies, the lensing analysis shows that the bulk of the mass in the cluster also passed through during the merger. This is interpreted as strong evidence for the existence of dark matter (Clowe *et al.*, 2006).

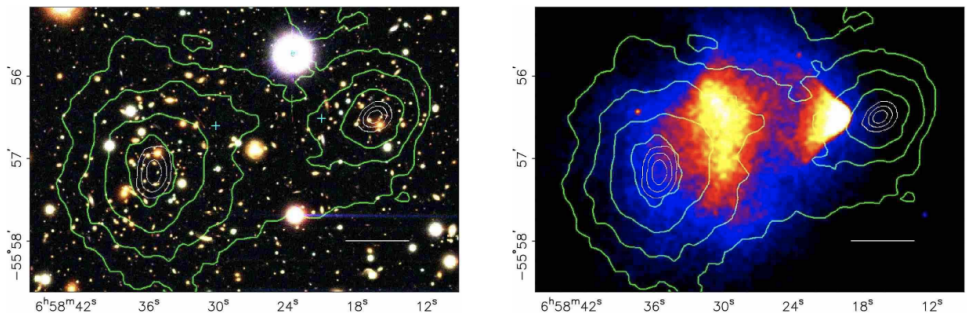

Figure 2.3: The Bullet Cluster. The green contours in both panels represent the total mass distribution derived from gravitational lens modelling. The left panel shows an optical image of the cluster, while the right panel shows the X-ray emission. Note that the contours follow the stellar light from the cluster member galaxies much more closely than the more massive X-ray-emitting gas.

Abell 370 is also believed to be the result of two clusters merging, because it is bimodal in its light distribution and the gas is offset towards the centre of the cluster (Molnar *et al.*, 2020, Umetsu *et al.*, 2022). Fig. 2.4 shows a map of the X-ray emission in Abell 370. The effect where the gas is offset from the overall mass distribution is not as pronounced as in the Bullet Cluster, but it is evidence that Abell 370 is a merging cluster approaching equilibrium.

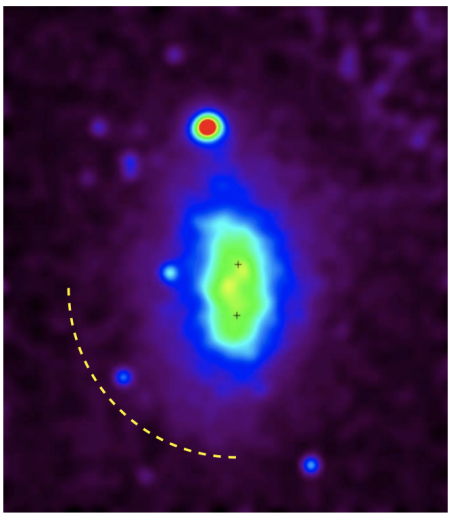

Figure 2.4: A heat map of the smoothed X-ray surface brightness in Abell 370 taken with Chandra. The black crosses mark the peaks of the mass distribution found with a lensing study (Strait *et al.*, 2018). Note that while the gas is centrally concentrated, the yellow peaks of the gas distribution do not match the total mass distribution. The bright spot to the north-east is a foreground galaxy and not part of the cluster. Credit: Molnar *et al.*, 2020

When lens modelling, one of the central assumptions of many codes is that 'light-traces-mass', i.e. that the dark matter distribution of the cluster follows the light distribution in the cluster to some degree. Whether this is a good assumption is a matter of debate; this will be discussed in context of my lens model and others' in Section 5.1.3.

2.3 High-redshift galaxies

Galaxies lensed by clusters include some of the most distant known in the Universe (e.g. Atek *et al.*, 2023, Harikane *et al.*, 2023). Without lensing, many of these would have a brightness below observational limits, but a cluster can magnify the image of a background galaxy by factors of sometimes more than 100. Lensing can also make galaxies more spatially resolved then they would be otherwise, and sometimes magnify them enough that detailed spectroscopy can be performed (e.g. Livermore *et al.*, 2015, Mason *et al.*, 2017). Fig. 2.5 shows an example of spatially resolved emission line maps of magnified galaxies.

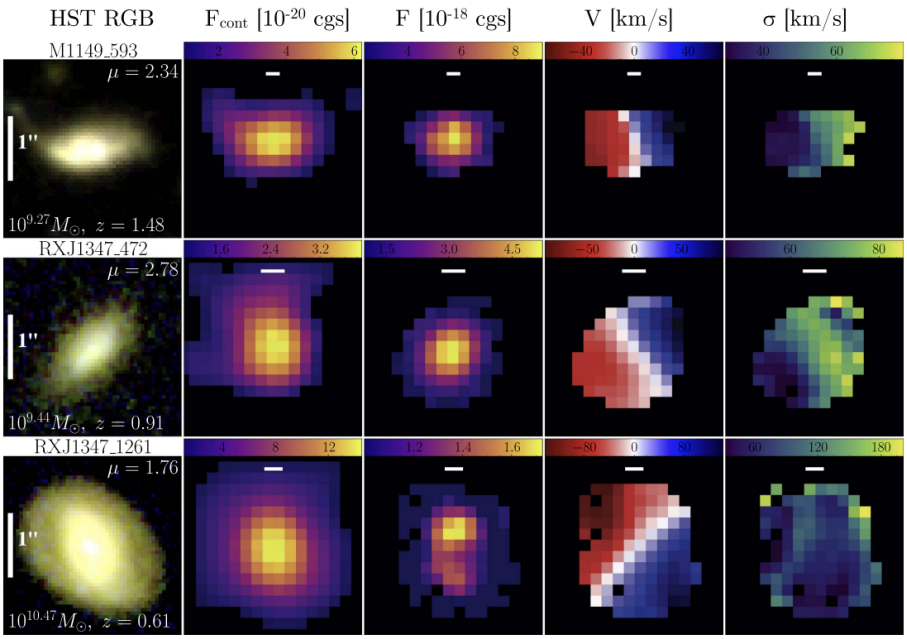

Figure 2.5: An example of 2D emission line maps and velocity maps of lensed galaxies from z∼0.5-2. Mason *et al.*, 2017

Another benefit of studying lensed galaxies is that it gives us greater insight into the overall populations of galaxies at different redshifts. How galaxies' size, morphology, star formation rate, and other parameters have evolved over the history of the Universe is one of the most important open questions in astronomy. As distance increases however, only the brightest objects remain visible, creating a biased view of the galaxy populations at a given redshift. Luminosity functions (see example in Fig. 2.6) demonstrate that there are far more faint galaxies than bright ones. If we can observe more faint galaxies with gravitational lensing, we can gain a more balanced picture of the populations at high redshift.

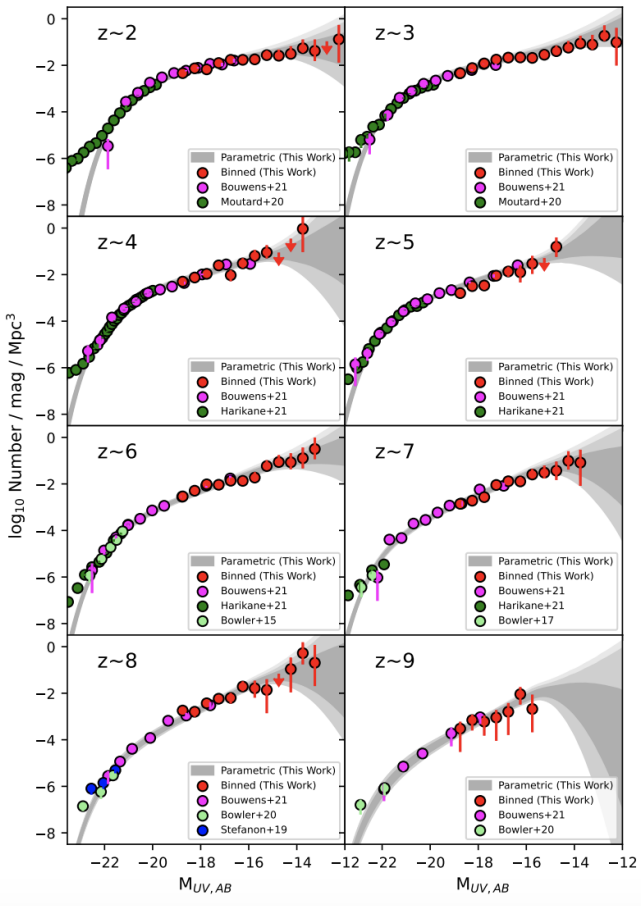

Figure 2.6: UV luminosity functions in redshift bins from z∼2-9. Note that at all redshifts, faint galaxies are far more abundant than bright galaxies. (Bouwens *et al.*, 2022)

Before most detailed information about lensed galaxies can be learned, it is important that we understand the distribution of mass and magnification in the cluster lensing field. Some properties of a galaxy, such as its estimated

age, depend only on the shape of its spectrum, which is not affected when it is lensed. Other properties, such as the stellar mass and star formation rate, depend on the magnitude of its spectrum, which is different than it would be without the magnification effect. A major goal of lens modelling is to create maps of the magnification across the cluster for any given source redshift such that accurate parameters for the background galaxies can be derived. The relationship between mass and magnification allows us to use lens modelling to derive information about the mass distribution of the cluster itself, while also providing us with the information necessary to study background galaxies.

3 Methods

3.1 Data

This section will describe the data used for this project. I used HST and JWST imaging (Sections 3.1.1 and 3.1.3) for both visually inspecting the background galaxies that make up the constrains of my lens model and also for spectral energy distribution (SED) fitting. Archival spectra from the Multi Unit Spectroscopic Explorer (MUSE) instrument on the Very Large Telescope (VLT) (Section 3.1.2) were used to confirm multiple image systems, and I used slitless specta from JWST (Section 3.1.3) to spectroscopically confirm certain redshifts.

3.1.1 HST imaging

This work focuses on the galaxy cluster Abell 370. It was included in the Hubble Frontier Fields (HFF) survey with HST, one of the deepest surveys ever undertaken by Hubble (Lotz *et al.*, 2017). The cluster was followed up by JWST in December 2022 as part of the Canadian NIRISS Unbiased Cluster Survey (CANUCS) program, 3 months after the start of this thesis. As such, I started the lens modelling project by constructing a preliminary model using HST Wide Field Camera 3 (WFC3) images. The HST images used for visual inspection included WFC3 images F105W, F160W (19.4 hours), and F125W, and F140W (9.6 hours).

A photometry catalogue containing fluxes in the filters F160W, F140W, F125W, F105W, F814W, F606W, and F435W was also provided to be used in the SED fitting section of the project (Gabe Brammer, private communication).

3.1.2 MUSE spectra

Between November 2014 and September 2016, MUSE was used to take spectra in the Abell 370 field. MUSE is an integral field unit spectrograph (IFU) with a field of view of 1 square arcminute, capable of taking medium-resolution spectra with wavelengths in the optical range of 475-930 nm (Richard *et al.*, 2021).

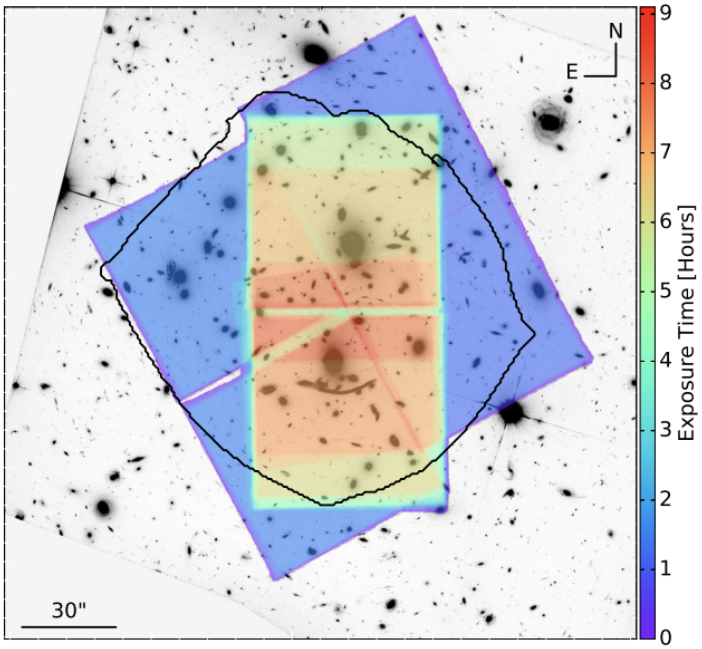

Figure 3.1: The MUSE exposure time across the Abell 370 field. The central region received longer exposures to reduce the impact of intracluster light. The black line shows the region inside which strongly lensed galaxies up to z=10 can be found. Source: Lagattuta *et al.*, 2019

Lagattuta *et al.* (2019) used this data to determine the redshfits of many objects in the field to 4 significant figures, including cluster members, and many of the systems of multiple images. The authors provided images of the emission lines that they used to determine the redshift of a system, as well as the catalogue of objects in the field for which they obtained spectra in the supplemental material of the paper. I used these materials as a starting point for making the lens model, as described in more detail below.

3.1.3 JWST imaging and slitless spectra

JWST is a space-based observatory launched to the L2 Lagrange point of the Sun-Earth system on December 25th, 2021. Its main instruments are the Near Infrared Camera (NIRCAM) (Rieke *et al.*, 2005), the Near Infrared Imager and Slitless Spectrograph (NIRISS) (Doyon *et al.*, 2012), the Near-Infrared Spectrograph (NIRSpec) (Jakobsen *et al.*, 2022): a near-infrared spectrograph, and the Mid Infrared Instrument (MIRI) (Rieke *et al.*, 2015), which can take images and spectra in the mid-infrared. This project uses data from NIRCAM and NIRISS.

NIRCAM is a near-infrared camera and consists of two near-identical modules that can simultaneously observe 2.2'x2.2' fields in wavelengths from 0.6-5 microns. Each module has two channels, one for observing short wavelengths and one for long. It uses a dichroic to observe both wavelengths at the same time (*JWST User Documentation* 2022).

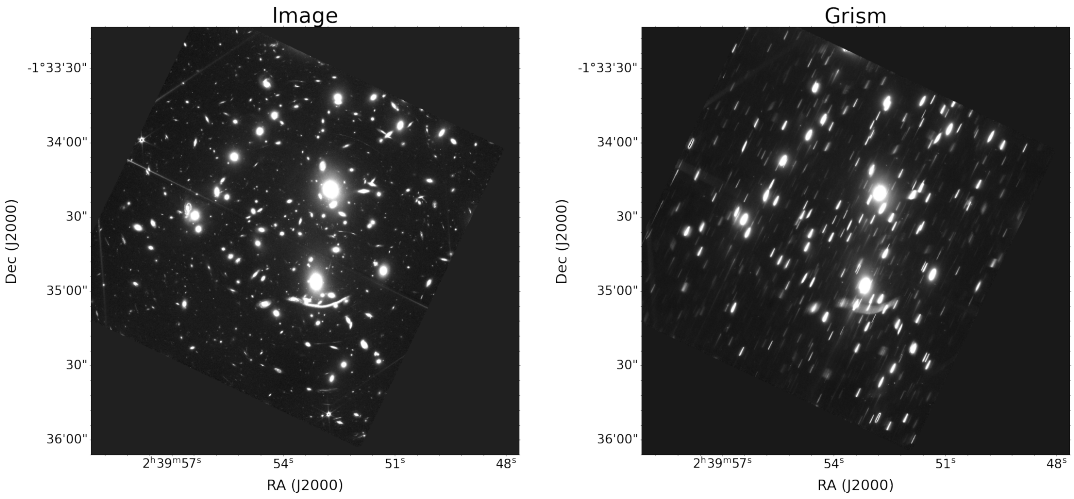

Figure 3.2: An example of a NIRISS image of the Abell 370 field next to the same image dispersed with a grism. The light from each source is dispersed into a low-resolution spectrum on the image.

NIRISS performs wide-field slitless spectroscopy with the same field of view as NIRCAM and a wavelength range of 0.8-2.2 microns. This allows for low resolution spectroscopy of every object in the field of view. Fig. 3.2 shows an example of a dispersed image beside the equivalent direct (non-dispersed) image. The filter wheel for this mode of observation includes two grisms with a mean resolving power of $\lambda/\Delta\lambda$=150. The two grisms are different only in

that they disperse light in directions orthogonal to each other. Using both dispersion directions helps to disentangle blended spectra and in some cases allows for spatially resolved spectra (Willott *et al.*, 2022).

NIRCAM and NIRISS images of Abell 370 were obtained as part of the CANUCS survey. The goal was to observe 5 strong lensing clusters with NIRCAM, NIRISS, and NIRSpec over approximately 200 hours of observing time. The specific cluster fields were chosen for their strong gravitational lensing and the abundance of existing multi-wavelength data available. Fig. 3.3 shows the observations taken in the Abell 370 field. The primary science goal of CANUCS is to understand the evolution of low-mass galaxies over cosmic time. NIRISS observations are taken in 3 filters: F115W, F150W and F200W, with an exposure time of 9.7 kiloseconds per configuration. NIRCAM images are taken with F090W, F115W, F140M, F150W, F162M, F182M, F210M, F250M, F277W, and F300M with 2.9 hr exposures and F335M, F360M, F410M, and F444W with 1.6 hour exposures (Willott *et al.*, 2022).

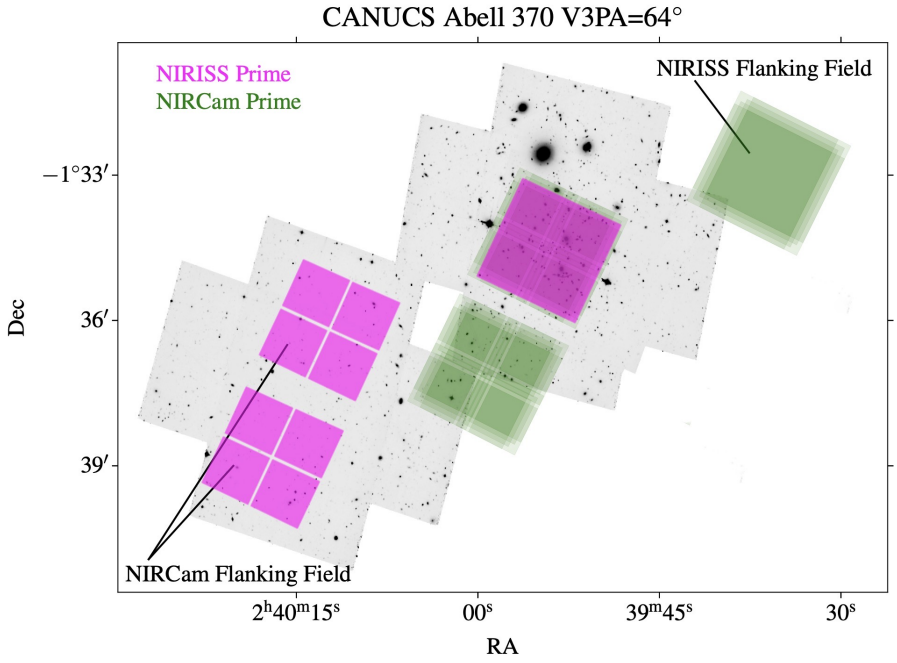

Figure 3.3: The cluster and flanking fields for which observations were taken in Abell 370 as part of the CANUCS program. (Willott *et al.*, 2022)

3.1.4 Data reduction with GRIZLI

GRIZLI (Brammer, 2023) is a a wide-ranging software pipeline developed to process imaging data from HST and JWST, as well as to extract and fit grism slitless spectroscopy like that produced by NIRISS. It processes the data from beginning to end, starting by processing the raw observations by flat fielding, sky subtraction, astrometric alignment, and removing hot pixels and cosmic rays, similar to the process described in Simons *et al.* (2021) and Matharu *et al.* (2022). All NIRISS and NIRCam data in this thesis have been processed and reduced by Gabe Brammer using GRIZLI. For wide field slitless data, GRIZLI also models the contamination that arises from overlapping spectra in the image. Fig. 3.4 shows how multiple grism orientations can help remove the contamination from overlapping spectra.

The pipeline is capable of fitting spectra and deriving the redshift of an object. A set of flexible stellar population synthesis (FSPS) models with emission lines added (Conroy *et al.*, 2009, Conroy and Gunn, 2010) are projected to the pixel grid of the 2D exposures and fit to the observed 2D spectra. A range of redshifts over which to search can be provided to GRIZLI. The final redshift is that which minimizes the χ^2 statistic of the fit. Simons *et al.* (2023) compared grism redshifts derived with GRIZLI to ground-based slit spectroscopy redshifts of the same sources and found that the difference was negligible.

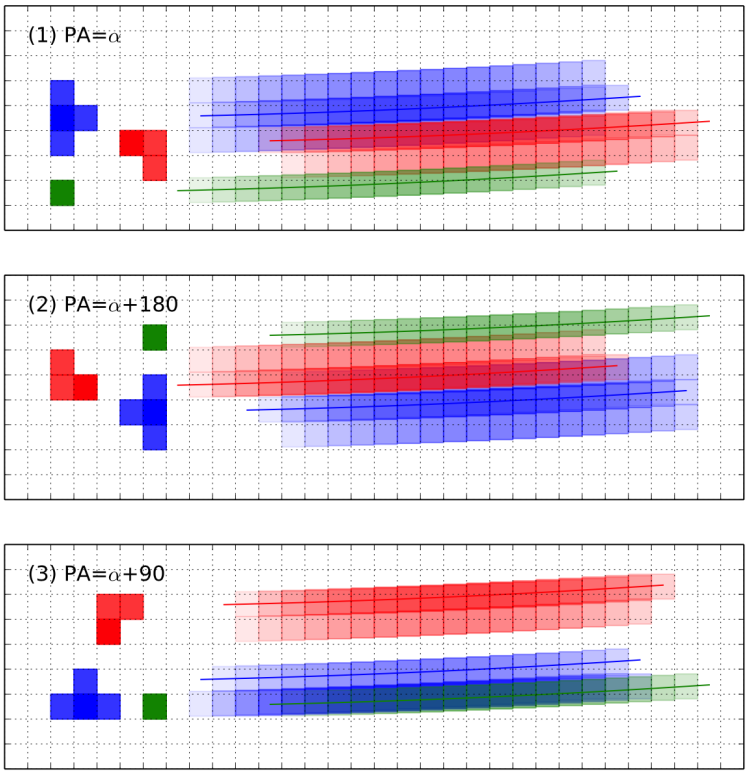

Figure 3.4: Contamination from nearby sources is a problem when using slitless spectra - the spectra often overlap. Taking multiple exposures with different position angles on the sky results in different types of contamination and helps GRIZLI disentangle the different spectra. Credit: *JWST User Documentation* (2022)

The output of a GRIZLI extraction will show the 2D spectrum in each filter alongside a postage stamp image of the object in a direct (i.e., not dispersed) image. Each orientation will be shown in the first 2 rows, followed by a third row containing the 2 spectra added together and the continuum subtracted. If there are strong emission lines in the spectrum, they should be visible in this row. Sometimes the spectrum contains contamination from other sources, which is primarily visible as emission off center in the 2D exposures. An example of a face-on spiral galaxy from the galaxy cluster MACS-0417 is shown in Fig. 3.5; note the clear spatially resolved emission lines in the bottom left panel.

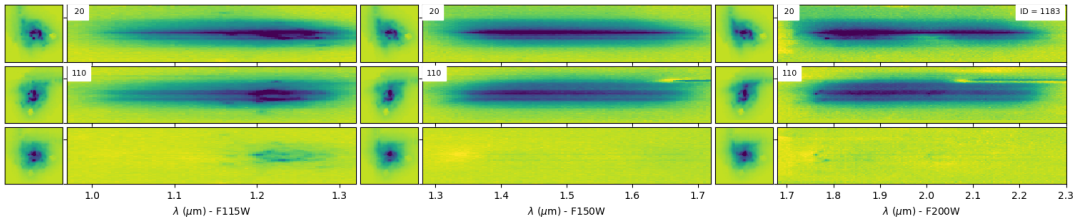

Figure 3.5: The 2D spectrum of an example of a spatially resolved galaxy lensed by the cluster MACS-0417. It is clear to see that the images in the first 2 rows are the same object rotated 90 degrees and that the continuum-subtracted spectrum shows spatially-resolved emission lines.

When redshift-fitting, GRIZLI outputs the probability distribution of redshift over the range it was given alongside a 1D spectrum with the fitted model. Note that there are small gaps in wavelength between the filters and that removing contamination may also cause gaps in the spectra. I will discuss my use of NIRISS spectroscopy in more detail in Sections 4.2.4 and 5.2.1.

3.2 Lens modelling

3.2.1 Lenstool

LENSTOOL is a lens modelling code first developed by Kneib *et al.* (1993) to model strong lensing in galaxy clusters. It has been updated several times since (Kneib *et al.*, 1996, Jullo *et al.*, 2007, Jullo and Kneib, 2009). It is parametric, meaning that it makes assumptions about the shape of the distribution of mass and fits the best parameters for those distributions. Starting from a model containing the cluster member galaxies, one or more cluster-scale 'halos' with a given density profile, and a set of constraints given by the positions of the multiple image systems in the cluster, LENSTOOL uses a Markov Chain Monte Carlo (MCMC) sampler to find a best fit model for the distribution of mass such that when the multiple images are projected to the source plane, and then back to the lens plane, it reproduces the original images as closely as possible.

There are several options for the profile of the mass distribution, including a point mass, elliptical singular isothermal sphere, and a Navarro-Frenk-White profile (NFW). Here I will use a pseudoisothermal elliptic mass distribution

profile (PIEMD) as defined by Kassiola and Kovner (1993). It is similar to the NFW profile in shape, but flattens out within the core radius. Studies (e.g. Grillo *et al.*, 2015) that have compared NFW and PIEMD profiles have found that PIEMD profiles provide a better fit to the data when lens modelling galaxy clusters.

This profile takes the following quantities as parameters: the coordinates of the centre, ellipticity, orientation angle, core radius r_c, cut radius r_{cut}, and central velocity dispersion σ. The mass density ρ is defined in Equation 3.1 (Limousin *et al.*, 2005).

$$\rho(r) = \frac{\rho_0}{\left(1 + \frac{r^2}{r_c^2}\right)\left(1 + \frac{r^2}{r_{cut}^2}\right)} \tag{3.1}$$

$$\rho_0 = \frac{\sigma^2}{2\pi G}\left(\frac{r_{cut} + r_c}{r_c^2 r_{cut}}\right) \tag{3.2}$$

The PIEMD profile is characterized by density ρ_0 in the central region. ρ_0 is related to the velocity dispersion σ (Equation 3.2), which is a measurement of the depth of the potential well and thus related to the mass of the halo. In the transition region where $r_c < r < r_{cut}$, the density falls isothermally as $\rho \propto r^{-2}$. Outside of r_{cut}, the density drops more steeply, falling from $\rho \propto r^{-2}$ to $\rho \propto r^{-4}$ (Limousin *et al.*, 2007, Lagattuta *et al.*, 2017).

The minimization process is done with an MCMC sampler, which applies Bayesian methods to the problem of finding the best-fit parameters (Jullo *et al.*, 2007).

The inputs for LENSTOOL include:

- A catalogue of cluster member galaxies including their positions, semi-major and -minor axes, angle, and magnitude.
- A catalogue of multiple image systems found in the cluster. The columns start with an id number specifying which system each source belongs to, then positions, ellipticity, redshift, and magnitude.

- A file describing various parameters of the model:
  - Runmode: Contains arguments that turn optimization on and off, tells LENSTOOL whether to calculate convergence (defined in Equation 2.6) and shear (Equations 2.10 and 2.11), and provides the reference coordinate for the cluster.
  - Grille: Describes the grid used for optimization and specifies how many 'halos' will be optimized.
  - Potential: There should be one of these sections for each mass halo. It requires an estimate for the position, ellipticity, orientation, core and cut radii, and velocity dispersion of the mass.
  - Image: Provides the filename of the catalogue of multiple image systems and defines the position error of the images.
  - Limit: Tells LENSTOOL whether to optimize each of the parameters from the potential section(s) and if so, inside what range and with what step-size.
  - Potfile: Characterizes the distribution of the cluster member galaxies. Their size and velocity distributions are scaled according to their magnitudes (Kneib *et al.*, 1996) and the surface mass density follows a PIEMD profile. It is also possible to decide whether or not these parameters are optimized.
  - Cline: A list of redshifts for which to calculate critical and caustic curves, and which algorithm is used for that computation.
  - Cosmology: Defines the values for cosmological constants. I assume a ΛCDM cosmology with $H_0 = 68$ km s^{-1} Mpc^{-1}, $\Omega_m = 0.27$, and $\Omega_\Lambda = 0.73$.
  - Field: Defines the size of the field for map outputs like shear and convergence in arcseconds. Here I use a square of 300x300 arcseconds centered on the northern brightest cluster galaxy (BCG).

LENSTOOL returns numerous output files, some by default and some that one must request in the parameter file. These include:

- Critical curves: Defines where in the image the magnification is maximized. This changes depending on the redshift. LENSTOOL can calculate up to 9 critical curves during a single run.

- Convergence: Produces a map of the convergence.

- Shear: Produces a map of the shear.

- Best.par: A text file giving the parameters of the best fit solution found by LENSTOOL during its run. This file also includes a χ^2 statistic calculated from multiple image predicted positions, the number of degrees of freedom, and the Bayesian evidence (defined in Equation 3.9).

- Image.all: Contains the positions, semi-major and -minor axes, and angles of the images reconstructed by LENSTOOL as it projects the images to the source plane and back to the image plane.

- Bayes.dat: Contains the parameters for each iteration in the MCMC process.

3.2.2 Selecting the sample of cluster members

The catalog of MUSE observations provided in the supplemental material of Lagattuta *et al.* (2019) included many galaxies near the cluster redshift. For this project, I take everything within ± 0.1 of the cluster redshift 0.375 as a cluster member, as shown in Fig. 3.6. This is a total of 280 galaxies. I show a map of the cluster members on an RGB image in Fig. 3.7.

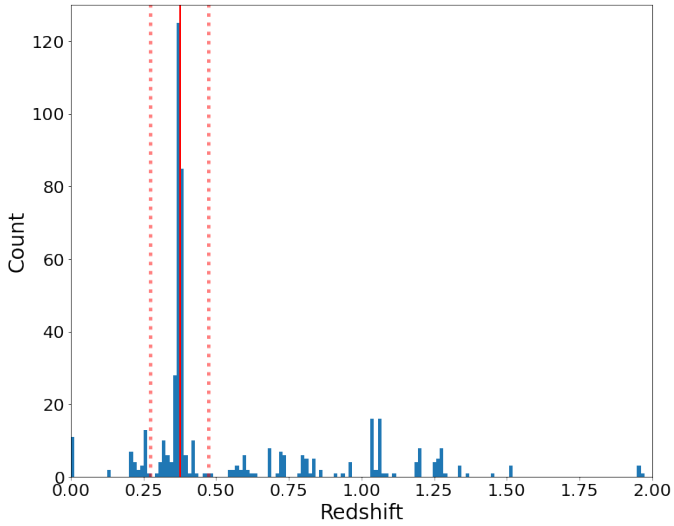

Figure 3.6: A histogram of the MUSE redshifts showing the peak at the cluster redshift 0.375. The dotted lines show the region from which I extracted the cluster members catalogue.

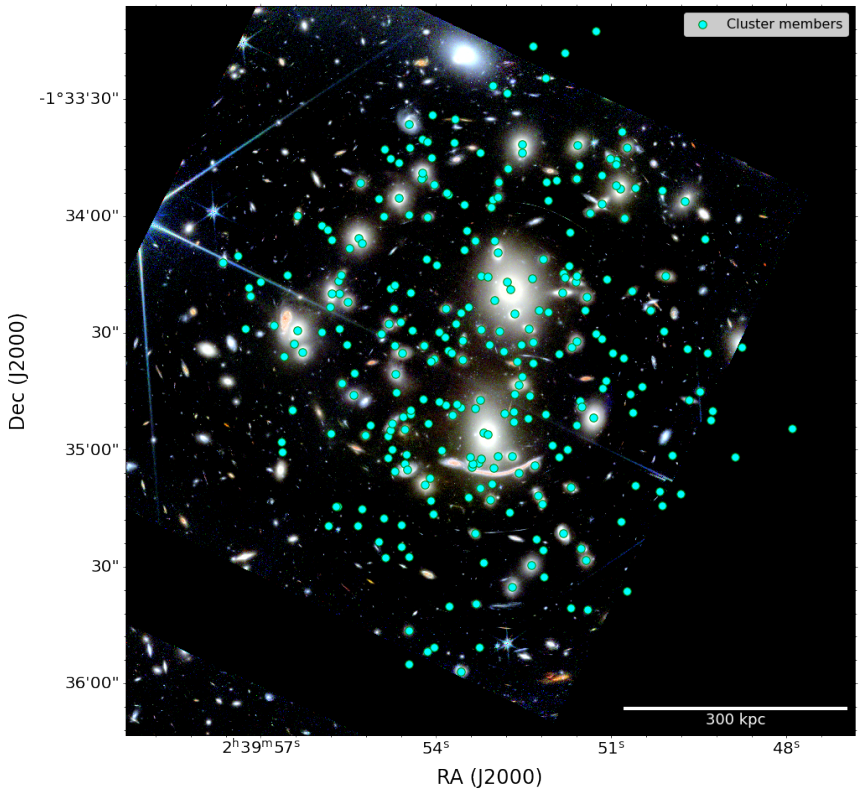

Figure 3.7: The sample of galaxies within ±0.1 of the cluster redshift plotted on top of a NIRCAM RGB image.

Like the cluster-scale dark matter halos, the cluster member potentials are fit with PIEMD profiles. The parameters of the cluster member galaxies vary, but in a more restrained manner compared to the halos. The core radius r_{core}, velocity dispersion σ, and cut radius r_{cut} of the cluster member galaxies are scaled according to their luminosities as described in Equations 3.3, 3.4 and 3.5 respectively (Kneib *et al.*, 1996). L^* is a luminosity derived from a scaling magnitude that must be provided to LENSTOOL. It is set to 20.701, the magnitude of the brightest galaxy in the field in the F814W filter. Following the example of Lagattuta *et al.* (2017), r^*_{core} is fixed at 0.15 kpc; because it should be small compared to r_{cut} and because it is strongly degenerate with σ (Jullo *et al.*, 2007). r^*_{cut} is allowed to vary uniformly between 10 and 50 kpc and the scaling velocity dispersion σ^* is fitted using a Gaussian prior with a mean of 158 km/s and standard deviation of 27 km/s.

$$r_{core} = r^*_{core}\left(\frac{L}{L^*}\right)^{\frac{1}{2}} \tag{3.3}$$

$$\sigma = \sigma^*\left(\frac{L}{L^*}\right)^{\frac{1}{4}} \tag{3.4}$$

$$r_{cut} = r^*_{cut}\left(\frac{L}{L^*}\right)^{\frac{1}{2}} \tag{3.5}$$

For a PIEMD profile where $r_{core} \ll r_{cut}$, the total mass is shown in Equation 3.6. It is possible to change the exponents on the r_{cut} and σ relations to reflect different mass-to-light ratios. The exponents shown in the equations above correspond to a constant mass-to-light ratio.

$$M_{tot} = \frac{\pi}{G}\sigma^2 r_{cut} = \frac{\pi}{G}(\sigma^*)^2 r_{cut}\left(\frac{L}{L^*}\right) \tag{3.6}$$

3.2.3 Choosing arcs

A LENSTOOL lens model is constrained by the positions of the systems of multiply imaged galaxies provided to it. As such, I am motivated to include

only the systems where I have a very high level of confidence that the images are indeed the same galaxy, and that the redshifts I have are accurate. Starting from the catalogue of multiple images in Lagattuta *et al.* (2019), I inspected all images in RGB composites of the NIRCAM filters combined in various different ways: F150W-F115W-F090W, F356W-F277W-F200W, F200W-F115W-F090W, F410M-F277W-F277W, F200W-F150W-F090W, F444W-F356W-F277W, F200W-F150W-F115W, F444W-F410M-F356W, and F277W-F200W-F150W. Because magnification from gravitational lensing is achromatic, the colour of all images in a system should match each other in each RGB composite. In addition, certain morphological features may only appear in certain bands so it is possible for a galaxy to appear non-descript in one composite and unique (i.e. more easily identified) in another.

To account for different levels of confidence in the systems, I construct three separate catalogues. The Gold model includes systems with very high confidence, the Silver model includes systems for which I am less sure, but still have a reasonable probability of being good constraints for the model, and the Bronze model includes all systems found in previous works (Lagattuta *et al.*, 2019) including those which have a low confidence level. I describe the criteria for each model in more detail below.

Studies on simulated lensing clusters have shown that accurate redshifts are important when using them as constraints for lens models (Johnson and Sharon, 2016). In general, increasing the sample size of multiple image systems reduces the systematic error in lens modelling, but above a certain number of systems (N>25), Johnson and Sharon (2016) found that adding a system with an inaccurate or missing redshift increased the error rather than decreasing it. In this project, I strongly prioritized high confidence in the accuracy of a system's redshift when choosing in which category of catalogue to place a system.

A Gold system is one that has a clear emission line in all its images, and where the colours and morphology in the NIRCAM images make it clear that they are the same galaxy. System 6, shown in Fig. 3.8, is an example of a very high confidence system. The redshift-determining emission line in Lagattuta *et al.* (2019) is clearly visible for all images, and the morphology of the images make it clear that they are all the same galaxy.

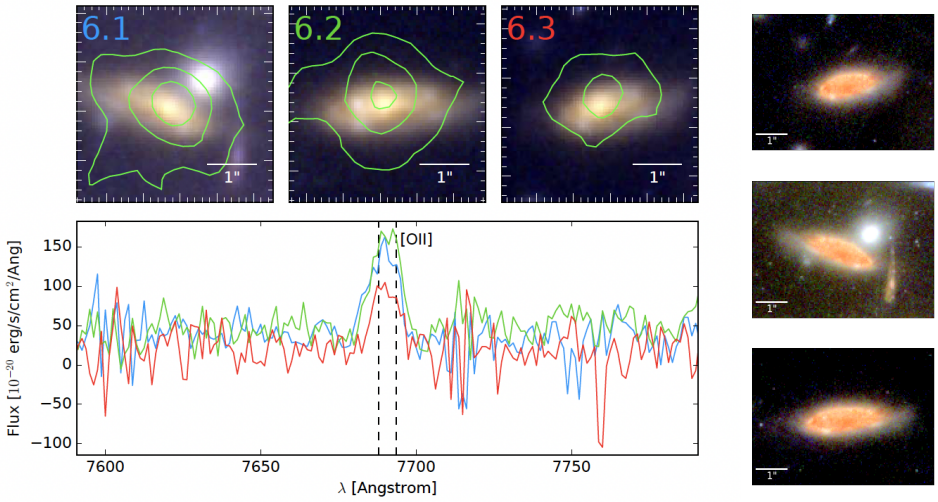

Figure 3.8: Left: The MUSE spectrum of the three images of System 6 zoomed in to the OII line that determined their redshift, with HST images (Lagattuta *et al.*, 2019). Right: the three images in an RGB (F277W-F200W-F150W) NIRCAM image. The redshift is well determined and the morphology of the galaxy in NIRCAM images matches.

A Silver system is one that is either convincing in its redshift determination, or in its morphology, but generally not both. Systems without spectroscopic redshifts altogether are automatically excluded from the Gold catalogue. Our Silver catalogue included System 8 and System 11 for this reason, but the latter was later promoted to Gold after the analysis described in Section 4.2. Some systems have some images that are counted as Gold while others are only included in the Silver catalogue.

An example of a Silver system is System 23, shown in Fig. 3.9. All images show emission at the same redshift, but the signal is significantly stronger in 23.1 compared to the other two. The colours of the images are similar, but the 2 knots seen in 23.1 are not visible in 23.2. 23.3 is detected but somewhat obscured by the brightness of a nearby cluster member.

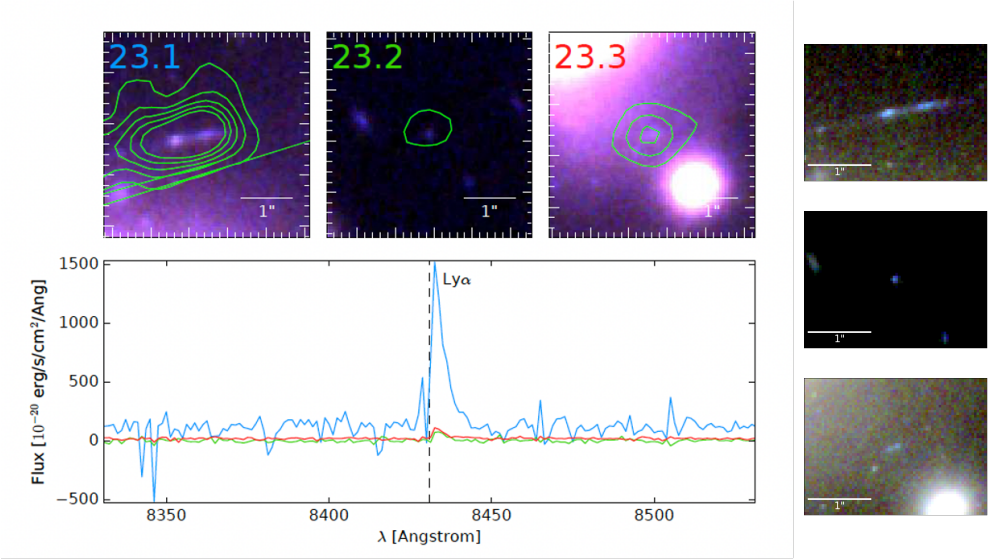

Figure 3.9: Left: The MUSE spectrum of the three images of System 23 zoomed in to the Ly-α emission that determined their redshift, alongside HST images (Lagattuta *et al.*, 2019). Right: the three images in an RGB (F200W-F150W-F090W) NIRCAM image. The colours are similar, but the morphology is somewhat different in the 3 images.

A special case is System 9. It was originally included in the Silver catalogue because, as shown in Fig. 3.10, 2 out of 3 of its redshift-determining lines were uncertain. In order to include as many systems as possible, I used GRIZLI to extract the NIRISS spectra of a number of Silver and Bronze systems to find out if it was possible to confirm their redshifts through lines with wavelengths too red to be detected with MUSE. Getting reasonable signal-to-noise with NIRISS spectra requires a relatively bright source and most of the systems for which this was attempted were too faint and thus too noisy. System 9, however, shows 2 very strong emission lines. By identifying these lines as the OIII doublet and Hα, we can say that the NIRISS spectra supports that System 9 has the same redshift found by Lagattuta *et al.* (2019), 1.5182. As a result, System 9 was promoted to the Gold catalogue. The 2-D NIRISS spectra for each image of System 9 is shown in Fig. 3.11 and the corresponding 1-D spectra and redshift probability distribution are shown in Fig. 3.12.

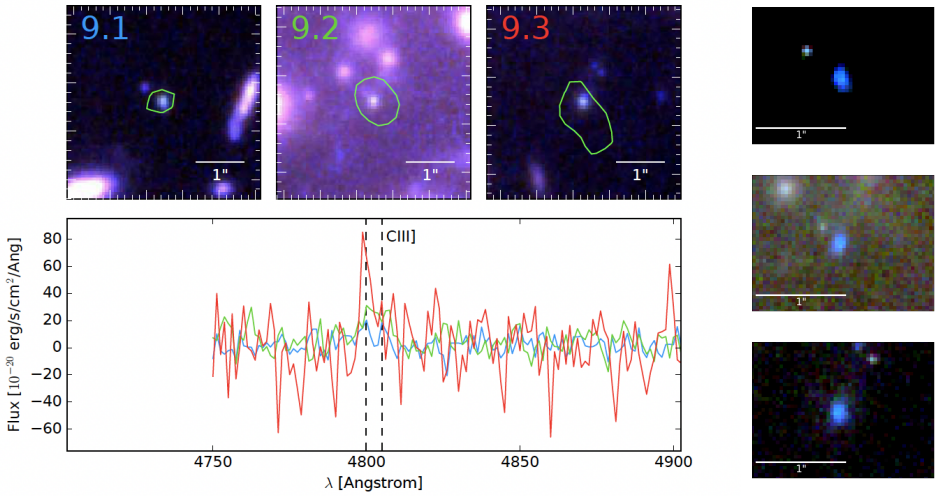

Figure 3.10: Left: The MUSE spectrum of the three images of System 9 zoomed in to the CII emission used to determined their redshift, alongside HST images (Lagattuta *et al.*, 2019). Right: the three images in an RGB (F200W-F150W-F090W) NIRCAM image.

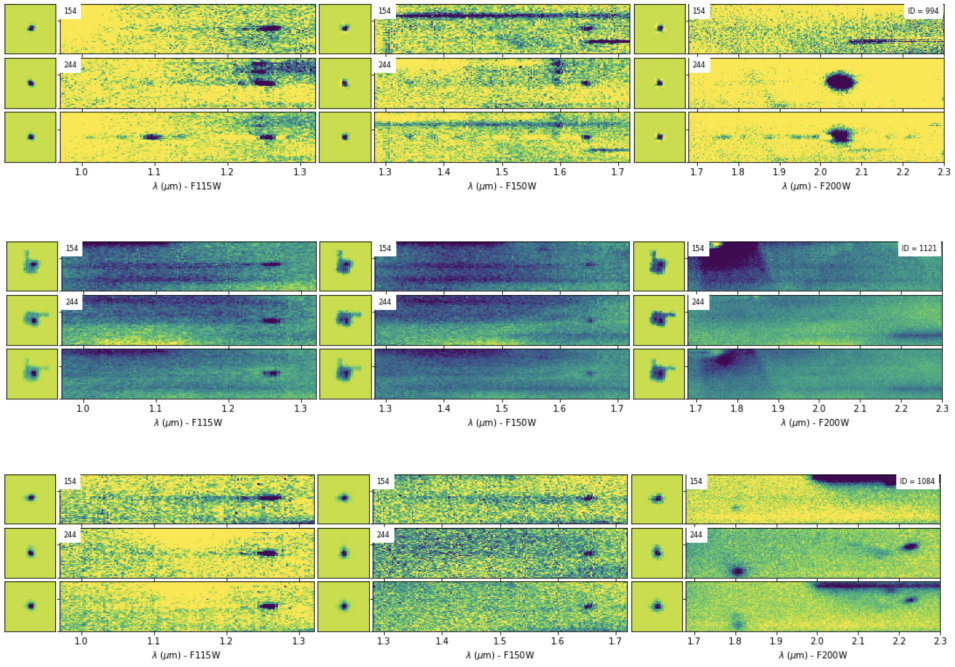

Figure 3.11: The 2D spectra of the 3 images of System 9. The two emission lines at approximately 1.25 and 1.65 microns are visible in all three images.

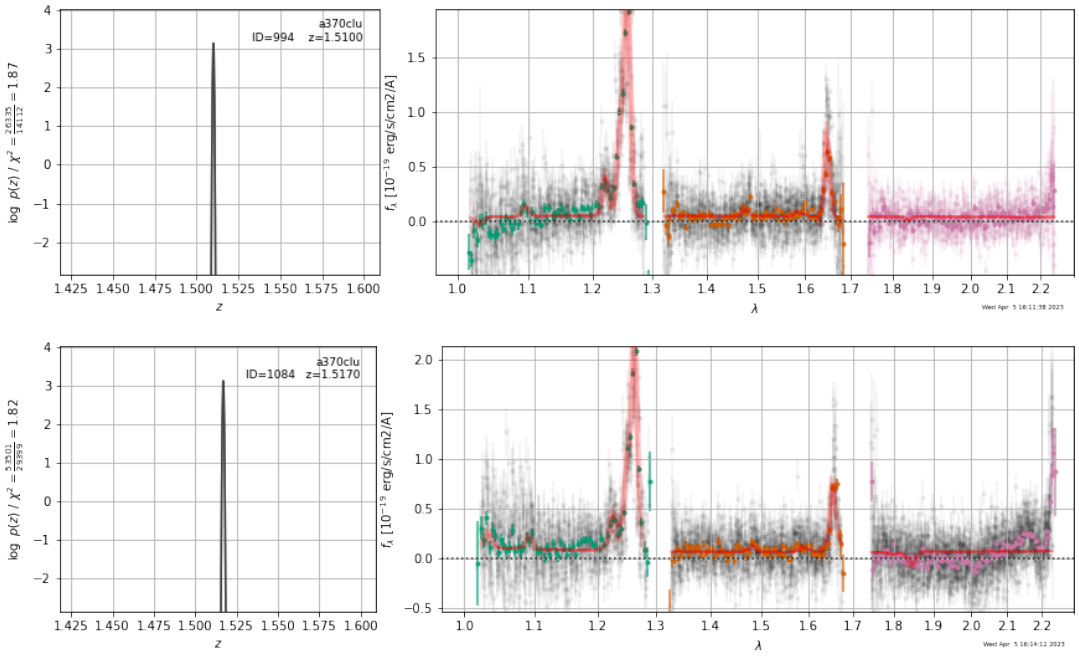

Figure 3.12: The 1D spectra and redshift posterior probability function for images 9.1 (top) and 9.3 (bottom). The [OIII]5007+4960 doublet and Hα lines are clearly visible and the redshifts are consistent with each other and the literature value from Lagattuta *et al.* (2019). GRIZLI could not extract a 1D spectrum for image 9.2, however as shown in Fig. 3.11, the emission lines are at an identical wavelength.

A Bronze system is one left out of the Gold and Silver catalogues, which can be for a couple of different reasons. One example is System 21 (Fig. 3.13), where the morphology in the NIRCAM images is simply too different for us to be confident that the images are the same galaxy in the source plane, even if they do have the same redshift.

A second reason that a system could be categorized as Bronze is that Lagattuta *et al.* (2019) identified a number of systems that had strong emission lines (mostly Ly-α) but were not detectable in the NIRCAM images. It is possible that these are real multiple image systems - one of them, System 30 was not detected in the HST images, but its 2 faint images were detected with NIRCAM. I included it in my Silver catalogue. However, without being able to compare the colours and morphology of the majority of these systems, I cannot discount the possibility that they are separate sources with similar redshifts. Fig. 3.14 shows System 36, an example of one of these systems.

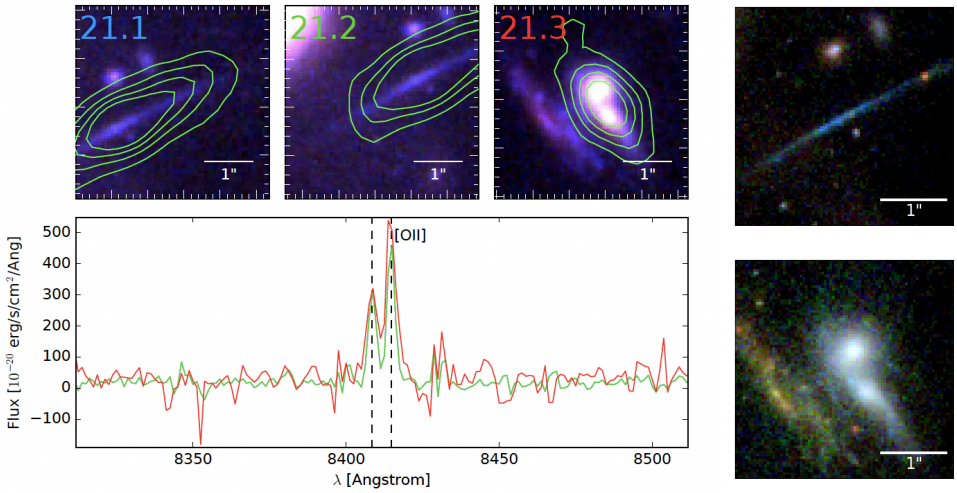

Figure 3.13: Left: The MUSE spectrum of the three images of System 21 zoomed in to the Ly-α emission that determined their redshift, alongside HST images (Lagattuta *et al.*, 2019). Right: the two images in an RGB (F200W-F150W-F090W) NIRCAM image, showing their differing morphologies. The discrepancy in the number of images is because Lagattuta *et al.* (2019) separated the thin arc into two separate images.

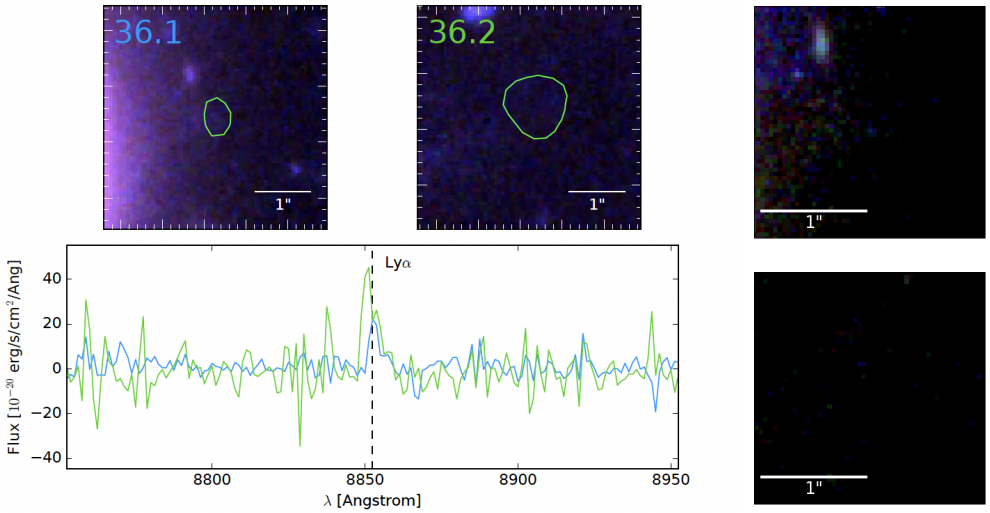

Figure 3.14: Left: The MUSE spectrum of the three images of System 36 zoomed in to the Ly-α emission that determined their redshift, alongside HST images (Lagattuta *et al.*, 2019). Right: the coordinates in an RGB (F200W-F150W-F090W) NIRCAM image, showing that there is no detection in the image at those locations.

3.2.4 Knots

While some of the lensed galaxies appear relatively featureless on the image, others are spatially resolved enough to see the same features recurring in different images. In order to provide LENSTOOL with as much information as possible, some of these systems were separated into multiple 'knots'. This is particularly helpful when the image is very stretched and spatially extended over a large region of sky. For example, System 3, as shown in Fig. 5.3, is composed of 2 extended thin arcs, and one more compact image. The green centre of the galaxy is one knot and the bright spot at the edge of the galaxy is another. Images 3a.1 and 3b.1 in the top panel of Fig. 5.3 are separated by 4.7 arcseconds. Including more spatial information helps LENSTOOL model the critical curve at the system redshift more precisely.

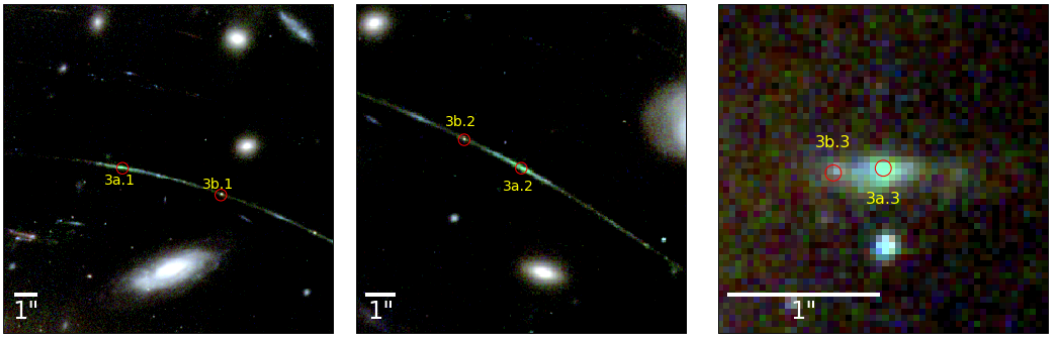

Figure 3.15: The knots in System 24. Though many knots are visible, it is better to include only 2 to avoid weighting this system more highly than other lensed galaxies.

The risk of including knots in the model is that it introduces weights on the image systems, something that is otherwise not included in LENSTOOL. For example, System 24 has 6 individual knots visible in each image of the galaxy. Including all of these knots would weight the galaxy 6 times higher in the model than a galaxy that appears as a single source. For this system, it was decided to keep knots c and d (see Fig. 3.17) in order to capture the spatial extent of the images and discard the others in order to avoid biasing the model too much.

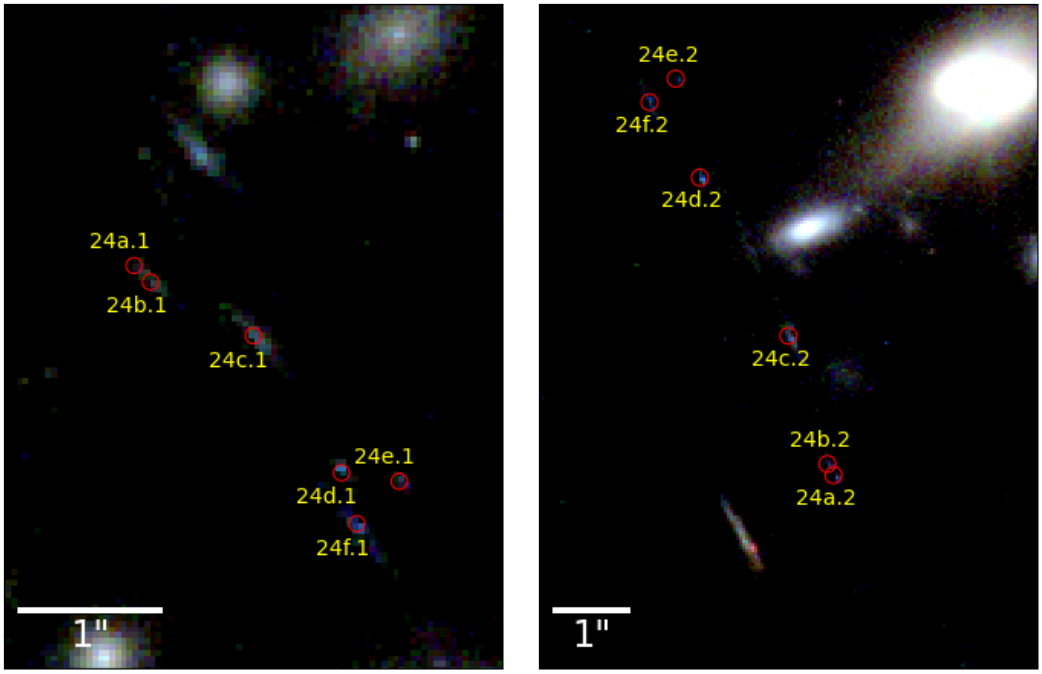

Figure 3.16: The knots in System 24. Though many knots are visible, it is better to include only 2 to avoid weighting this system more highly than other lensed galaxies.

3.2.5 Choosing potentials

Making a lensing model is a process involving many iterations. The first step is to start with a model that roughly approximates the shape of the mass distribution. Inspired by previous works (Lagattuta *et al.*, 2017, Strait *et al.*, 2018) and inspecting the images of Abell 370 by eye, I started with 2 mass halos centered on the two BCGs in the centre of the cluster. Reducing the number of constraints helps make the shape of the model simpler, so I began by restricting the multiple image catalogue to systems 1-5. At this point in the project, I did not yet have access to the JWST and MUSE data that would allow me to fully evaluate the confidence level of each system as described in Section 3.2.3. However, the first five systems were known to be spectrocopically confirmed, and their morphologies in the HST images are very convincing.

Without optimization, I manually adjusted the halo parameters - position, core radius, velocity dispersion, ellipticity, and angle until the critical curves corresponding to the redshift of each strong lensing system passed through the images in that system. The cut radius is fixed at a large value, 800 kpc,

because for mass halos on these scales the cut radius is expected to lie outside the strong lensing radius of the cluster and therefore cannot be constrained with our data (Lagattuta *et al.*, 2019, Mahler *et al.*, 2023). The critical curve should pass between two images that are a mirror image of each other as the parity of the magnification will be opposite on either side of the critical curve.

Once the model is approximately correct by eye, I re-run the model with optimization on. I also introduce the final cluster member and multiple image catalogues to the model. There are several ways to quantitatively evaluate how well the model fits the data. One is the χ^2 statistic, which is a measurement of the distance between the images reconstructed by LENSTOOL and the true position of the image. A perfect fit within the position error σ would have a χ^2 value equal to the number of degrees of freedom ν. The χ^2 statistic is described in Equation 3.7. System i has n_i images. $x^j(\theta)$ represents the position of image j predicted by a model with parameters θ and the error on the observed position of the image, x^j_{obs}, is σ_{ij}. For all images in my model I take the position error to be 0.3 arcseconds.

$$\chi^2_i = \sum_{j=1}^{n_i} \frac{(x^j_{obs} - x^j(\theta))^2}{\sigma^2_{ij}} \tag{3.7}$$

Another measure of how good the fit is is the root-mean-square (rms) displacement of the reconstructed images. For image i in a system with N images, the distance to each predicted image $\hat{x}_{ij}$ is measured in arcseconds, and then the root-mean-square of the distances is calculated as in Equation 3.8.

$$RMS_i = \sqrt{\frac{\sum_{j=1}^{N}(\hat{x}_{ij} - x_i)^2}{N}} \tag{3.8}$$

In a perfect model, a system with N images should have N reconstructed images on top of each of its real images. I measured the rms for each system individually; it was useful to know how well the model predicts the different images.

Last, I also examine the Bayesian evidence of the fit.

$$Pr(\theta|D,M) = \frac{Pr(D|\theta,M)Pr(\theta|M)}{Pr(D|M)} \tag{3.9}$$

Bayesian evidence is the denominator in Bayes' equation (Equation 3.9), and describes the probability of getting the observed data D given the assumed model M. In this case, the model is the parameterization provided to LENSTOOL. Unlike the χ^2 statistic, Bayesian evidence favours simple models over complex ones. When comparing models, an improvement in χ^2 but a decrease in evidence is a sign that the model is overfitting (Jullo *et al.*, 2007). Note that evidence is not particularly meaningful on its own, but it is a useful tool when comparing different models.

At the end of every run, I calculate the reduced chi-squared statistic χ^2/ν and the rms deviation and examine the Bayesian evidence output by LENSTOOL. I take the best fit parameters for the potential halos and input them into the next model. When the best fit parameters are near the edge of the range given in the limit section of the parameter file, I need to adjust the limits to ensure that there is not a better fit out of range. When the parameters begin to stabilize near the middle of their ranges, the limits can be narrowed to allow LENSTOOL to get more granular in the parameter space over the number of iterations it can perform. It is worth noting that the reason I use an iterative process is to limit computation time. The parameter space of a lens model is large and there are many degeneracies, both between the parameters of a single potential (especially r_{core}, r_{cut}, and v_{disp}) and between the size and shape of the different potentials. This makes lens modelling a computationally expensive process; to explore the full parameter space would require far more time and power.

When the model was no longer improving after several iterations, it was necessary to go back a few steps and change the number and configuration of mass halos. For example, the fit improved when some of the cluster member galaxies were included as individual halos. These were the two BCGs in the centre of the cluster and one of the galaxies very near the giant luminous arc. Later, I also added cluster member galaxies near Systems 3 and 5 as individually optimized masses because their proximity to those systems was distorting the shape of the critical curve. Adding other halos where there

is an overdensity of larger cluster members also improved the fit. The final configuration of potentials is shown in Fig. 4.2.

3.3 SED fitting

Fitting the SED of a galaxy is a way to estimate its properties such as mass, age, and star formation rate from imaging data in different bands. In this project, I use new photometry from JWST alongside photometry from HST to constrain the properties of a z$\sim$7 galaxy in the Abell 370 field.

3.3.1 BAGPIPES

Bayesian Analysis of Galaxies for Physical Inference and Parameter EStimation (BAGPIPES) is an SED fitting code based in Python and designed to model the stellar continuum and nebular emission from galaxies using photometry. (Carnall *et al.*, 2018).

BAGPIPES generates model galaxy spectra based on several factors. The first is stellar population synthesis (SPS) models. These are derived from the models made by Bruzual and Charlot (2003) (Bc03), and updated in 2016 with spectra from the Medium-resolution Isaac Newton Telescope (MILES). They are constructed of simple stellar population models (SSP), which are a function of wavelength, the age of the population, the metallicity of the galaxy, and the initial mass function (IMF). BAGPIPES uses the IMF defined by Kroupa and Boily (2002). Age and metallicity are varied on a grid to make the set of models loaded into BAGPIPES.

One assumption that goes into creating the model spectra is the star formation history SFR(t): the star formation rate as a function of time. SFR(t) can be composed of one or a sum of multiple star formation history forms. The star formation rate is calculated for all $t_i = t(z_{obs}) - a_i$ where $a_i < t_i$ and a_i represents the age bin of the SPS model. The bins have uniform width in $log_{10}(\Delta a/Gyr)$. Here I use simple parametric models for the star formation rate, either a single delayed exponential, or constant star formation, defined below.

The star formation rate in the delayed exponential model is given by Equation 3.10. T_0 represents the starting time for star formation in the galaxy, and τ is the timescale parameter that governs the speed of the exponential decline (if τ is positive) or increase (if τ is negative) in star formation rate (Carnall *et al.*, 2019). In the constant star formation version, star formation 'turns on' to a constant value at some point in its history. The time at which it starts forming stars, and the magnitude of the constant SFR are parameters fit by BAGPIPES.

$$SFR(t) = \begin{cases} (t - T_0)\ \exp(-\frac{t-T_0}{\tau}) & t > T_0 \\ 0 & t < T_0 \end{cases} \tag{3.10}$$

Next, BAGPIPES considers the transmission of the ionized interstellar medium (ISM) in the galaxy; line emission, absorption, continuum emission, and emission from warm dust. This model is implemented using the CLOUDY photoionization code from Byler *et al.* (2017). CLOUDY is run using each Bc03 SSP and varying the ionization parameter $log_{10}(U)$; U is a dimensionless quantity that describes the ratio of ionizing photons to the density of hydrogen atoms in the ISM. In BAGPIPES, the density of hydrogen atoms is fixed at 100 atoms/cm^3.

Lastly, BAGPIPES includes the transmission of the neutral ISM from dust attenuation and emission. There are a few options for dust attenuation laws, for this project I use the dust law from Calzetti *et al.* (2000) because it is the dust law most used for extragalactic studies (e.g. Grillo *et al.*, 2015, Carnall *et al.*, 2018, Strait *et al.*, 2021). Dust emission is governed by a single-temperature blackbody function modified by a factor of ν^β where ν is frequency and β represents the spectral emissivity. The general form of the dust law used by BAGPIPES is described in Equation 3.11, while the specific form of $k(\lambda)$ and the value of R_V are from the Calzetti law. a_{BC} is the lifetime of stellar birth clouds, which I have set to 0.01 Gyr. A_V is the extinction, which I allow to vary over a range between 0 and 2 magnitudes, and η is a constant factor that accounts for the additional attenuation near HII regions.

$$log_{10}(T^0(a_i,\lambda)) = \begin{cases} -\frac{0.4\eta A_V k_\lambda}{R_V} & a < a_{BC} \\ -\frac{0.4 A_V k_\lambda}{R_V} & a < a_{BC} \end{cases} \tag{3.11}$$

These components are combined to give the luminosity of the galaxy as a function of wavelength in the manner shown in Equation 3.12. N_c and N_a are the number of star formation components and age bins respectively. $SFR_j(a_i, \lambda, Z_j)$ represents the star formation history as a function of age, wavelength, and metallicity. $T^+(a_i$ is the transmission function of the ionized ISM, $T^0(a_i, \lambda)$ is the transmission function of the neutral ISM due to dust, and Δa_i is the size of the bin.

$$L_\lambda(\lambda) = \sum_{j=1}^{N_c} \sum_{i=1}^{N_a} SFR_j(a_i, \lambda, Z_j) T^+(a_i, \lambda) T^0(a_i, \lambda) \Delta a_i \tag{3.12}$$

In Equation 3.13 luminosity is converted to observed flux by redshifting to z_{obs} and accounting for the luminosity distance D_L. Note that redshift z_{obs} can be set to a specific value if it is known, or allowed to be a free parameter over some range. T_{IGM} describes the transmission function of the inter-galactic medium (IGM) according to the model defined by Inoue *et al.* (2014).

$$f_{\lambda_{obs}}(\lambda_{obs}) = \frac{L_\lambda(\lambda)}{4\pi D_L(z_{obs})^2 (1 + z_{obs})} T_{IGM}(\lambda, z_{obs}) \tag{3.13}$$

The goal of BAGPIPES is to fit the models described above to observational data according to the principles of Bayesian inference. We hypothesize that the model parameterization (number and type of SFH components, type of dust model, etc.) describes the data and define prior probability distributions for the parameters of this model. We then provide observational data and uncertainties which are used to constrain those parameters.

The likelihood $\mathcal{L}$ describes the probability of obtaining the observational data under the distribution we have defined. The likelihood function used by BAGPIPES (Equation 3.14) assumes that the uncertainties σ_i on the observed data points f_i are Gaussian and independent. $f_i^{\mathcal{H}}(\Theta)$ is the predicted flux corresponding to f_i.

$$ln(\mathcal{L}) = -0.5 \sum_i ln(2\pi\sigma_i^2) - 0.5 \sum_i \frac{(f_i - f_i^{\mathcal{H}}(\Theta))^2}{\sigma_i^2} \tag{3.14}$$

Given the model, prior distribution, and observational data, BAGPIPES uses the MULTINEST nested sampling algorithm defined by Feroz and Hobson (2008) and implemented in Python by Buchner *et al.* (2014) to find the best-fit posterior distribution. The outputs include the posterior spectrum, its posterior star formation history, and a corner plot showing the posterior probability distributions of each parameter and any correlations between parameters. These will be shown in Section 4.2.

3.3.2 Fitting the SED of System 11

System 11 is a multiply imaged galaxy with 2 images. Both images have a photometric redshift of 7.84±0.02 (Strait *et al.*, 2018) and had not been previously spectroscopically confirmed. For this project, I investigated the spectrum of this galaxy using GRIZLI to extract its NIRISS spectrum and BAGPIPES to constrain its properties by fitting its SED.

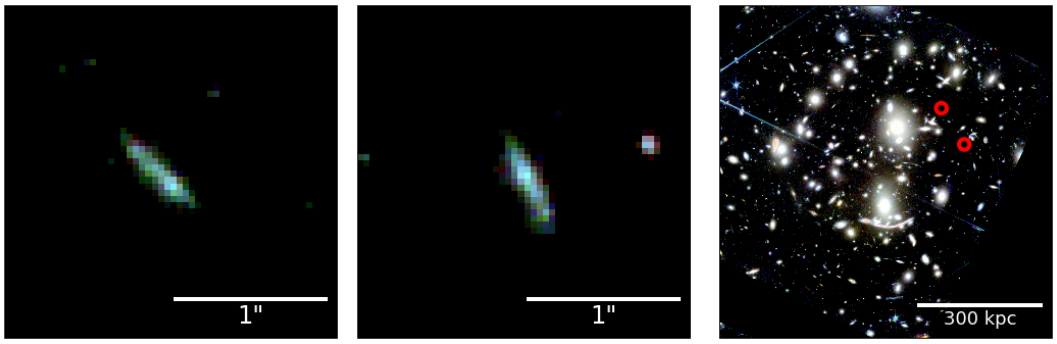

Figure 3.17: The two images of System 11 in a F200W-F150W-F090W RGB image from NIRCAM (left and centre) and their positions in the cluster field (right)

Practically, the first step to fitting an SED with BAGPIPES is to provide the throughput for each of the filters for which you plan to provide photometric measurements. BAGPIPES also requires a photometric catalogue, which is derived from the same segmentation of the NIRCAM images used by GRIZLI in Section 3.1.4. I used the Python module *xmatch* to match coordinates from the multiple image catalogue to the correct ID in the photometric catalogue. For

comparison purposes, I ran BAGPIPES with data that includes measurements from HST only and HST+JWST.

It is worth noting that there may be a third image of this galaxy. Lagattuta *et al.* (2019) found that their lens model predicted the position of a fainter image with similar colours. However, this image is very close to two cluster member galaxies and was not segmented separately in the image. As such, it does not have its own ID in the photometric catalogue and cannot be investigated at this time.

Next I define the priors described above in Section 3.3.1. The dust type is set to the Calzetti form, and the extinction A_V and factor ϵ are allowed to vary between [0, 2] and [1, 10] respectively. log(U), the ionization parameter, is set to -2. The star formation history form is set to either 'delayed' or 'constant'. The prior distribution for τ in the delayed exponential form is uniformly distributed (Carnall *et al.*, 2019).

To start, I allowed the redshift to vary between 1 and 10, but when the program consistently found a redshift between 7.5 and 8.0, I narrowed the limits to this range to reduce the parameter space over which BAGPIPES needs to explore.

Note that some of the posterior parameters of background galaxies are only estimable if we know the magnification of the images, in particular the stellar mass and the star formation rate. Other parameters, like the age and metallicity of the galaxy are derived from the shape of the fitted spectrum and not its brightness and do not need to be scaled.

4 Results

In Section 4.1 I will present the Gold, Silver, and Bronze catalogues of multiple image systems and describe the best-fit lens model found for Abell 370 during the course of this research. In Section 4.2, I will present the results from fitting the SED of the System 11 galaxy and extracting its NIRISS spectrum.

4.1 Lens modelling

The final Gold model features 23 systems of multiply imaged galaxies. The Silver catalogue contains an additional 4 full systems, and additional images for 3 systems in the Gold catalogue. The Bronze catalogue contains 14 extra systems. Figure 4.1 shows a NIRCAM RGB image of the cluster with the positions of the images (colour-coded by catalogue) plotted on top.

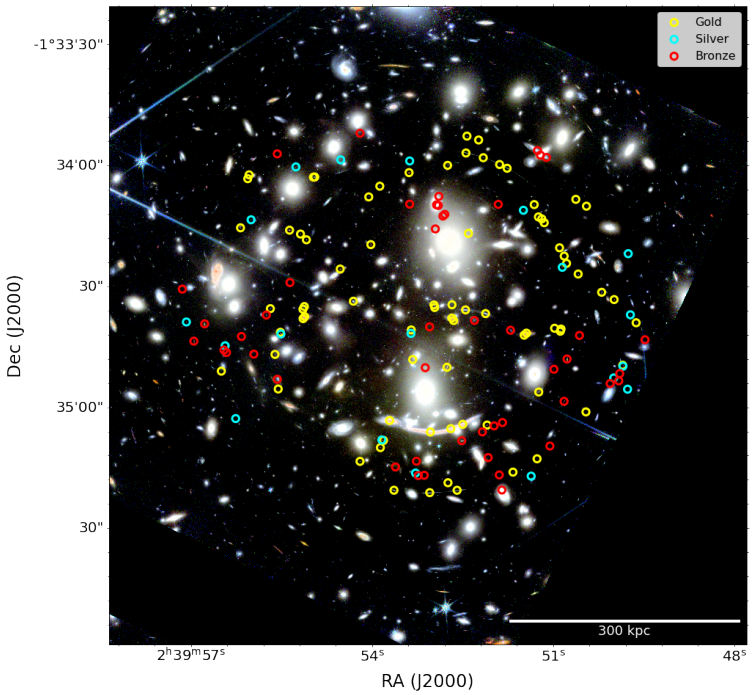

Figure 4.1: A NIRCAM RGB image of Abell 370 with the positions of all the multiple images in Abell 370 colour coded by the catalogue in which they are a member.

The positions and redshifts of the multiple images used in the Gold, Silver, and Bronze models are listed in Table 4.1.

ID	RA	Dec	Redshift	Catalogue
1.1	39.97629	-1.576023	0.8041	Gold
1.2	39.967161	-1.576876	0.8041	Gold
1.3	39.968546	-1.576618	0.8041	Gold
2a.1	39.973789	-1.584241	0.7251	Gold
2a.2	39.970973	-1.585035	0.7251	Gold
2a.3	39.968741	-1.584507	0.7251	Gold
2a.4	39.96956	-1.584804	0.7251	Gold
3a.1	39.9685154	-1.5658046	1.9553	Gold
3a.2	39.965677	-1.5668566	1.9553	Gold
3a.3	39.9789537	-1.5674604	1.9553	Gold
3b.1	39.9673222	-1.5661306	1.9553	Gold
3b.2	39.9661958	-1.5665973	1.9553	Gold
3b.3	39.9790446	-1.567469	1.9553	Gold
4a.1	39.9796721	-1.5763896	1.2728	Gold
4a.2	39.9707234	-1.5762784	1.2728	Gold
4a.3	39.9619525	-1.5779415	1.2728	Gold
4b.1	39.9797684	-1.5765674	1.2728	Gold
4b.2	39.9706752	-1.5764562	1.2728	Gold
4b.3	39.9620043	-1.5780896	1.2728	Gold
5.1	39.973486	-1.58905	1.2775	Gold
5.2	39.971018	-1.589217	1.2775	Gold
5.3	39.96913	-1.589053	1.2775	Gold
6a.1	39.9797577	-1.5772207	1.0633	Gold
6a.2	39.9693676	-1.577354	1.0633	Gold
6a.3	39.9644985	-1.5783614	1.0633	Gold
6b.1	39.9796515	-1.5770878	1.0633	Gold
6b.2	39.969486	-1.5771825	1.0633	Gold
6b.3	39.9643411	-1.5782225	1.0633	Gold
7.1	39.9698256	-1.580573	2.7512	Gold
7.3	39.968808	-1.5856333	2.7512	Bronze
7.4	39.986554	-1.5775806	2.7512	Bronze
7.5	39.961542	-1.5800056	2.7512	Bronze
7.6	39.9683489	-1.5713448	2.7512	Gold
8.1	39.9645508	-1.5697533	2.98	Silver
8.2	39.961868	-1.5736833	2.98	Silver
9.1	39.9624	-1.5778861	1.5182	Gold
9.2	39.969483	-1.5762667	1.5182	Gold
9.3	39.982017	-1.5765333	1.5182	Gold
11.1	39.963804	-1.5693611	7.6942	Gold
11.2	39.960771	-1.5741472	7.6942	Gold
12b.1	39.9840783	-1.5709608	3.4809	Gold
12b.2	39.9697827	-1.5666566	3.4809	Gold

12b.3	39.9591524	-1.5754052	3.4809	Gold
13.1	39.979532	-1.5717869	4.248	Gold
13.2	39.9752263	-1.5688311	4.248	Gold
13.3	39.9567692	-1.5775058	4.248	Gold
14a.1	39.9813269	-1.5781642	3.1309	Gold
14a.2	39.9722981	-1.5780015	3.1309	Gold
14a.3	39.9721943	-1.5800387	3.1309	Gold
14a.4	39.9576976	-1.5804348	3.1309	Gold
14a.5	39.9742092	-1.5856151	3.1309	Gold
15.1	39.971328	-1.580604	3.7085	Bronze
15.2	39.971935	-1.5870512	3.7085	Bronze
15.3	39.971027	-1.5777907	3.7085	Bronze
15.4	39.984017	-1.5784514	3.7085	Bronze
16.1	39.964016	-1.5880782	3.7743	Silver
16.2	39.966037	-1.5890355	3.7743	Bronze
16.3	39.984414	-1.5841111	3.7743	Silver
17.1	39.969758	-1.5885333	4.2567	Gold
17.2	39.985403	-1.5808406	4.2567	Gold
17.3	39.960235	-1.5836508	4.2567	Gold
18.1	39.97583	-1.5870613	4.4296	Gold
18.2	39.981476	-1.5820728	4.4296	Gold
18.3	39.957362	-1.5820861	4.4296	Silver
19.1	39.971996	-1.5878654	5.6493	Silver
19.2	39.985142	-1.5790944	5.6493	Silver
19.3	39.958316	-1.5813093	5.6493	Silver
20.1	39.965271	-1.5878028	5.7505	Gold
20.2	39.963608	-1.5868833	5.7505	Gold
21.1	39.966575	-1.5846139	1.2567	Bronze
21.2	39.967383	-1.5850278	1.2567	Bronze
21.3	39.981539	-1.5814028	1.2567	Bronze
22a.1	39.9816997	-1.5796877	3.1309	Gold
22a.2	39.9744221	-1.5861106	3.1309	Gold
22.3	39.957906	-1.5810108	3.1277	Bronze
23.1	39.980254	-1.5667639	5.9386	Silver
23.2	39.957314	-1.572744	5.9386	Silver
23.3	39.977165	-1.5662748	5.9386	Silver
24a.1	39.9635133	-1.5702107	4.9153	Gold
24a.2	39.9615735	-1.5734148	4.9153	Gold
24c.1	39.9632836	-1.5703459	4.9153	Gold
24c.2	39.9617365	-1.572911	4.9153	Gold
24d.1	39.963114	-1.5706099	4.9153	Gold
24d.2	39.9620561	-1.5723396	4.9153	Gold
25.1	39.9873002	-1.5787754	3.8145	Bronze
25.2	39.9617448	-1.5829204	3.8145	Bronze
25.3	39.966984	-1.5867999	3.8084	Bronze

26.1	39.979939	-1.5713902	3.9359	Gold
26.2	39.974464	-1.5680938	3.9359	Gold
26.3	39.957165	-1.5769585	3.9359	Silver
27.1	39.972446	-1.567157	3.0161	Gold
27.2	39.980694	-1.571125	3.0161	Gold
27.3	39.95829	-1.5759068	3.0161	Gold
28.1	39.963492	-1.5822806	2.9101	Gold
28.2	39.967058	-1.5845583	2.9101	Gold
28.3	39.987816	-1.5774528	2.9101	Silver
29a.1	39.9834878	-1.5673115	4.4897	Gold
29a.2	39.9684473	-1.5646408	4.4897	Gold
29a.3	39.9601989	-1.5694708	4.4897	Gold
29b.1	39.9835804	-1.5675745	4.4897	Gold
29b.2	39.9676432	-1.5649075	4.4897	Gold
29b.3	39.9609326	-1.5690004	4.4897	Gold
30.1	39.983351	-1.5704081	5.6459	Silver
30.2	39.972404	-1.5663533	5.6459	Silver
31.1	39.972404	-1.5693301	5.4476	Bronze
31.2	39.980667	-1.5747346	5.4476	Bronze
31.3	39.956158	-1.5786786	5.4476	Bronze
32.1	39.966286	-1.5693446	4.4953	Bronze
32.2	39.988098	-1.5751871	4.4953	Bronze
32.3	39.960682	-1.5783795	4.4953	Bronze
33.1	39.962723	-1.5860035	4.882	Bronze
33.2	39.966217	-1.5879961	4.882	Bronze
34.1	39.970108	-1.5701499	5.2437	Bronze
34.2	39.971806	-1.5880395	5.2437	Bronze
34.3	39.958565	-1.5817008	5.2437	Bronze
34.4	39.985046	-1.579559	5.2437	Bronze
35.1	39.981541	-1.5658624	6.1735	Bronze
35.2	39.975826	-1.5644423	6.1735	Bronze
36.1	39.962444	-1.5807098	6.2855	Bronze
36.2	39.965996	-1.5843844	6.2855	Bronze
37.1	39.97039	-1.5687943	5.6489	Bronze
37.2	39.970428	-1.5694203	5.6489	Bronze
38.1	39.9771985	-1.5738047	3.1563	Gold
38.2	39.9750827	-1.5721194	3.1563	Gold
39.1	39.965442	-1.5780222	1.2777	Bronze
39.2	39.967933	-1.5773472	1.2777	Bronze
39.3	39.982296	-1.576975	1.2777	Bronze
40.1	39.963579	-1.5656333	1.0323	Bronze
40.2	39.962958	-1.5661111	1.0323	Bronze
40.3	39.963375	-1.5659528	1.0323	Bronze
41.1	39.970546	-1.5693801	4.9441	Bronze
41.2	39.969977	-1.5700367	4.9441	Bronze

41.3	39.985223	-1.5793885	4.9441	Bronze
41.4	39.971395	-1.58802	4.9441	Bronze
42.1	39.970632	-1.5710393	4.3381	Bronze
42.2	39.983162	-1.5796664	4.3381	Bronze
42.3	39.973383	-1.5874465	4.3381	Bronze
42.4	39.957967	-1.5815081	4.3381	Bronze

Table 4.1: All multiple image systems in the Abell 370 field with their positions, redshifts, and in which catalogue they were included. Systems with sub-IDs such as a, b, etc. denote knots in a system.

The final sample of cluster members with their positions and the magnitude I used when scaling their size and velocity dispersion is given in the Appendix. Whenever any cluster member galaxies were optimized separately from the rest, such as the 4 in the final model, they were omitted from the cluster member catalogue provided to LENSTOOL.

The final lens model of Abell 370 features 5 dark matter halos and 4 individually modelled galaxies - the 2 BCGs and 2 galaxies near enough to multiple image systems to require more detailed modelling, and 276 cluster member galaxies modelled according to a mass-to-light ratio.

Fig. 4.2 shows the position, ellipticity, and angle of the optimized potentials. Note that the size of these ellipses is not a physical size but is instead scaled to reflect the relative mass of the potentials. Two potentials, DM2 and DM3, capture the mass in the centre of the cluster, while a third large potential, DM1, accounts for the overdensity of galaxies to the north-east of the cluster centre. The model statistics improved when I added a smaller fourth potential, DM4, to the north-west of the cluster centre and when a fifth potential, DM5, was added to the south-west region of the cluster. The choice to add a potential to each region was motivated by an overdensity of galaxies that were not taken into account by the central potentials alone. The reduced χ^2 statistic decreased and the Bayesian evidence improved with each addition.

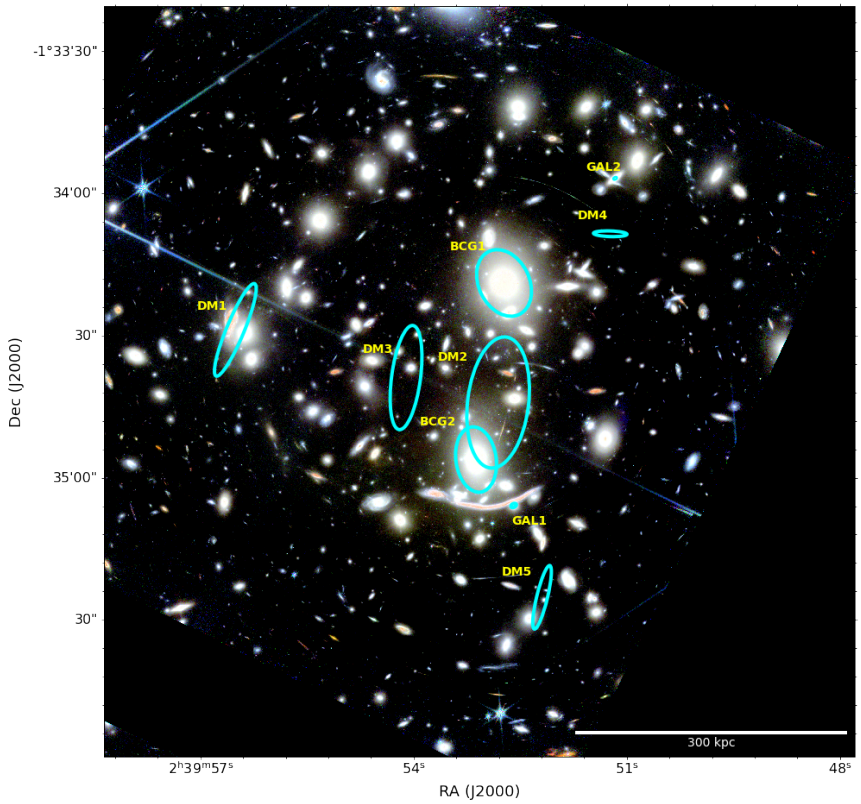

Figure 4.2: The positions of the optimized potentials in the best lens model found for Abell 370. Note that the sizes of the potentials are not physical sizes, but are scaled to show the relative masses of the different potentials. The fitted parameters for each potential are listed in Table 4.2.

Fig 4.3 shows best-fit convergence κ and magnification μ maps across the Abell 370 field. Both convergence and shear are calculated on a 4000x4000 pixel grid over a 300x300 arcsec field centered on the northern BCG in the cluster. Magnification is calculated from the convergence and shear using Equation 2.12. The maps correspond to the values for a background source at z = 9.0. The critical curve where the magnification is maximized is clearly visible in the magnification map.

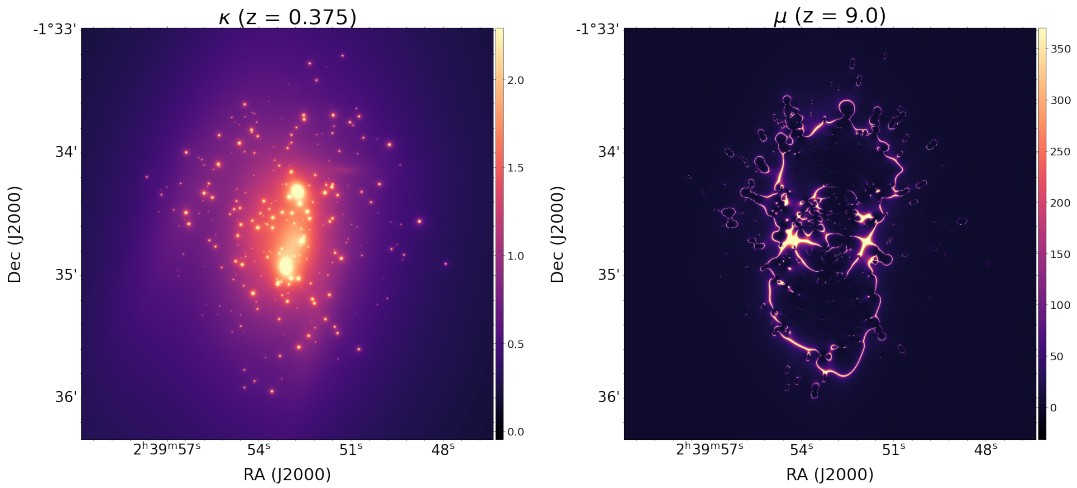

Figure 4.3: The convergence and magnification maps for the best model for a source at z = 9.0. The convergence closely resembles the galaxy light with a smooth distribution from the dark matter halos behind it.

Table 4.2 shows the best-fit parameters used in the final lens model of Abell 370. The names of the potentials match those in Fig. 4.2.

Potential	**Parameter**	**Best-fit value**
DM 1	$\Delta\alpha$ (")	-56.47
	$\Delta\delta$ (")	-9.13
	Ellipticity	0.88
	Angle (degrees)	67.4
	Core radius (kpc)	146.8
	Cut radius (kpc)	800 †
	Velocity dispersion (km/s)	586.6
DM 2	$\Delta\alpha$ (")	-1.02
	$\Delta\delta$ (")	-24.46
	Ellipticity	0.46
	Angle (degrees)	83.0
	Core radius (kpc)	56.4
	Cut radius (kpc)	800 †
	Velocity dispersion (km/s)	773.2
DM 3	$\Delta\alpha$ (")	-20.45
	$\Delta\delta$ (")	-19.20
	Ellipticity	0.71
	Angle (degrees)	82.5
	Core radius (kpc)	89.8

	Cut radius (kpc)	800 †
	Velocity dispersion (km/s)	615.5
DM 4	$\Delta\alpha$ (")	22.64
	$\Delta\delta$ (")	-19.20
	Ellipticity	0.71
	Angle (degrees)	178.2
	Core radius (kpc)	18.2
	Cut radius (kpc)	800 †
	Velocity dispersion (km/s)	196.7
DM 5	$\Delta\alpha$ (")	8.25
	$\Delta\delta$ (")	-65.57
	Ellipticity	0.89
	Angle (degrees)	76.4
	Core radius (kpc)	67.5
	Cut radius (kpc)	800 †
	Velocity dispersion (km/s)	383.3
BCG 1	$\Delta\alpha$ (")	0.24 †
	$\Delta\delta$ (")	0.77 †
	Ellipticity	0.20 †
	Angle (degrees)	-63.9 †
	Core radius (kpc)	0.15 †
	Cut radius (kpc)	436.5
	Velocity dispersion (km/s)	409.6
BCG 2	$\Delta\alpha$ (")	-5.67 †
	$\Delta\delta$ (")	-36.5 †
	Ellipticity	0.30 †
	Angle (degrees)	-81.9 †
	Core radius (kpc)	0.15 †
	Cut radius (kpc)	13.78
	Velocity dispersion (km/s)	385.6
GAL 1	$\Delta\alpha$ (")	2.26 †
	$\Delta\delta$ (")	-46.2 †
	Ellipticity	0.26 †
	Angle (degrees)	25.7 †
	Core radius (kpc)	0.15 †
	Cut radius (kpc)	38.3
	Velocity dispersion (km/s)	33.8

GAL 2	$\Delta\alpha$ (")	23.67 †
	$\Delta\delta$ (")	22.85 †
	Ellipticity	0.58 †
	Angle (degrees)	206.0 †
	Core radius (kpc)	0.15 †
	Cut radius (kpc)	25.0 †
	Velocity dispersion (km/s)	15.8
Cluster members	r^*_{cut} (")	2.51
	σ^* (km/s)	168.1

Table 4.2: Best-fit parameters for the halos and individually optimized galaxies in the best lens model. Fig. 4.2 shows these potentials plotted on an image of the cluster. Parameters marked with a † are fixed to those values and not optimized by LENSTOOL. Right ascension and declination are given relative to the reference coordinate of the cluster, (39.969767, -1.5721279), centered on the northern BCG.

I fixed certain parameters to reduce the parameter space and remove some of the degeneracies between parameters. For the cluster-scale halos, r_{cut} was fixed because it is expected to be larger than the strong lensing region of the cluster. For the individually optimized galaxy-scale halos, I fixed all known values - the positions, ellipticities, and angles were all taken from a HST-selected cluster member catalogue. The core radius for the optimized cluster members was fixed to 0.15 kpc in order to remove the strong degeneracy with velocity dispersion.

4.2 SED fitting and System 11

I ran BAGPIPES with the priors described in Table 4.3, and varied the form of the star formation history (SFH) to test how the output parameters would change. The fitted SEDs under the two different assumed star formation histories are given below, along with the posterior parameters and posterior SFHs.

Parameter	Prior
Star formation models	Bc03-MILES
Dust law	Calzetti
Dust extinction A_V	[0,2]
Dust factor ϵ	[1, 10]
Ionization parameter $log_{10}(U)$	-2
Redshift	[7.5, 8.0]

Table 4.3: Priors of the model provided to BAGPIPES to use when fitting the spectrum of the System 11 images. These priors were not changed when varying the form of the star formation histories.

4.2.1 Magnification

Some of the posterior parameters of background galaxies are only estimable if we know the magnification of the images, in particular the mass formed and the star formation rate. I derived the magnification of the System 11 images from the magnification map created with the best lens model. Image 1 is magnified by a factor of $6.0^{+1.7}_{-0.6}$ and Image 2 is magnified by a factor of $9.1^{+0.2}_{-0.9}$.

4.2.2 BAGPIPES Run #1: Constant star formation

The prior parameters for the first BAGPIPES run I did, where I assume constant star formation history, are stated in Table 4.4. The star formation is allowed to 'turn on' at any point in its history. The 'age minimum' prior, which dictates when star formation turns off, can also be allowed to vary. However, it was found to be consistent with 0 (meaning that star formation is ongoing) and so this was fixed to reduce computation time. The metallicity and the stellar mass M^* at the time of observation, $t(z_{obs})$, are allowed to vary over wide ranges that cover reasonable values for galaxies.

Parameter	Prior
Age minimum	0
Age maximum	[0,2]
Mass formed $log(M^*/M_\odot)$	[7, 11]
Metallicity $Z/Z_\odot$	[0,2]

Table 4.4: Priors of the constant star formation history model provided to BAGPIPES to use when fitting the spectrum of the System 11 images. Note that while the age can theoretically go up to 2 Gyr, the time since the Big Bang for a galaxy with a redshift z_{obs} of 7.6 is approx 0.6 Gyr and BAGPIPES automatically forbids any ages longer than the age of the Universe at the fitted redshift.

Fig. 4.4 shows the SEDs calculated by BAGPIPES under the assumption that the star formation history of the galaxy is constant and parameterized by the priors in Table 4.4. The blue points with errorbars are the measured fluxes in the available filters from HST and JWST. The yellow line is the posterior spectrum fitted to the data; note that its thickness reflects its 68% confidence limits. The orange rectangles represent the flux level expected given the spectrum. There is a small overlap of the HST and JWST filters near the break, which is why certain data points are very close together. Note also that the reason the expected values for the flux are lower than the spectrum near the break is because the bandwidth of the filters overlap with the break and therefore the average flux across the filter is lower.

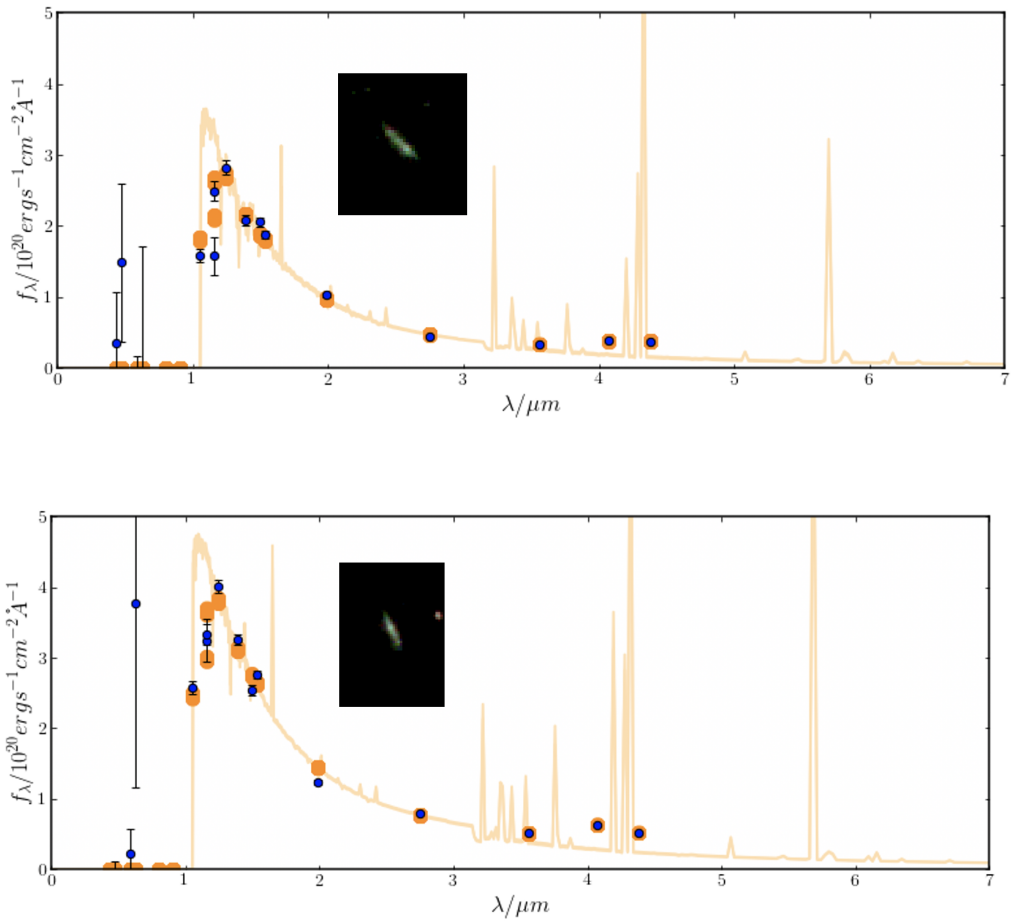

Figure 4.4: The SEDs of Image 11.1 (top) and Image 11.2 (bottom) fitted by BAGPIPES under the assumption of a constant star formation history. An RGB NIRCAM image of each image of the galaxy is overlaid on its SED. Note that the flux is the observed flux and has not been scaled by the magnifications of the images.

Table 4.5 shows the values and confidence intervals for the posterior parameters of the constant star formation history SED fit. Fig. 4.5 is a corner plot containing the posterior probability distributions of each of the free parameters. There is a strong degeneracy between A_V and η, as expected from their relationship in Equation 3.11. Both parameters increase the dust extinction; η is an extra factor included to account for increased dust around young stars. The values for the mass and star formation rate in the table have been scaled by the magnification of the images. The mass-weighted age is the weighted average age of the stellar population in the galaxy with the weights determined by mass.

Parameter	Posterior	
	Image 1	Image 2
Mass-weighted age (Gyr)	$0.007^{+0.001}_{-0.002}$	$0.006^{+0.002}_{-0.001}$
Mass formed $log(M^*/M_\odot)$	$7.60^{+0.05}_{-0.04}$	$7.61^{+0.06}_{-0.04}$
Star formation rate $M_\odot/yr$	$4.6^{+0.4}_{-0.4}$	$5.4^{+0.2}_{-0.2}$
Metallicity $Z/Z_\odot$	$0.29^{+0.07}_{-0.07}$	$0.09^{+0.01}_{-0.01}$
Dust extinction A_V	$0.10^{+0.04}_{-0.04}$	$0.09^{+0.02}_{-0.02}$
Dust factor η	$2.4^{+1.9}_{-0.7}$	$3.7^{+0.7}_{-0.7}$
Redshift	$7.667^{+0.007}_{-0.006}$	$7.648^{+0.006}_{-0.004}$

Table 4.5: Posterior parameters of the model with constant star formation history. The mass and star formation rate have been scaled by the magnification.

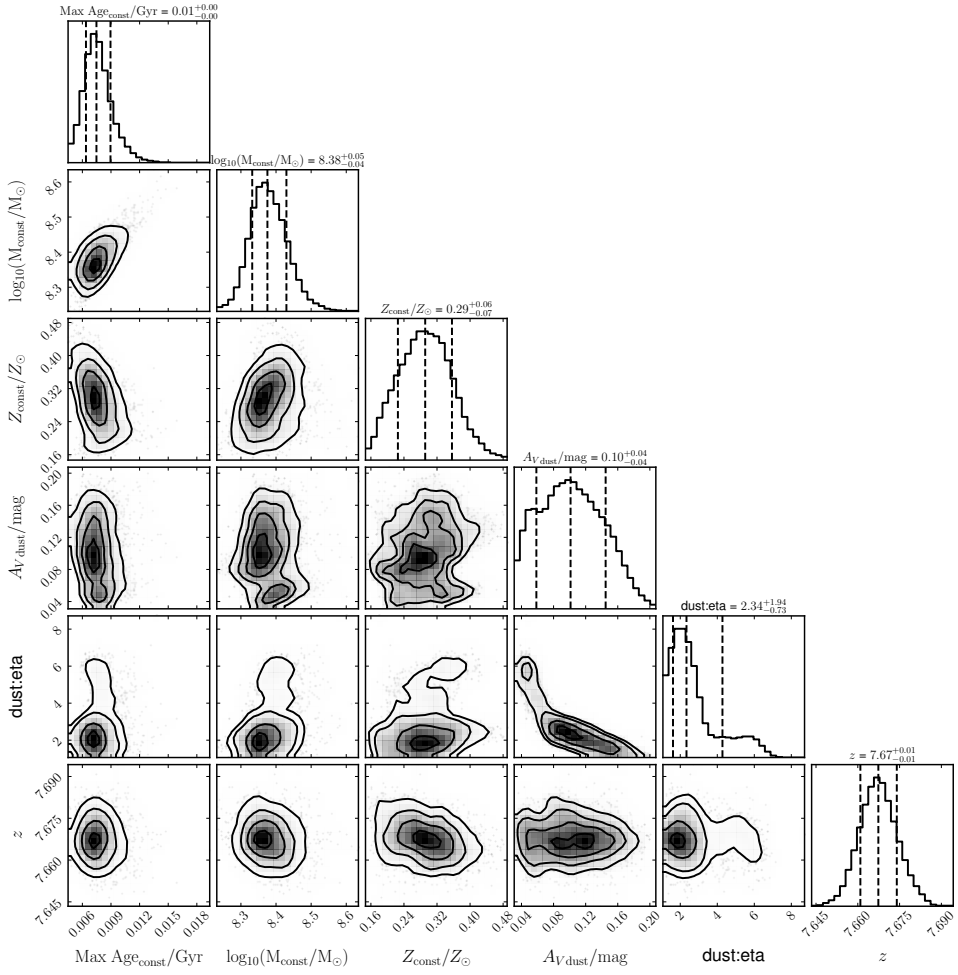

Figure 4.5: A corner plot showing the posterior probability distributions of each free parameter fit by BAGPIPES for Image 11.1 when the star formation history is constant.

The best-fit star formation history found by BAGPIPES is shown in Fig. 4.6. The posterior spectrum contains strong emission lines typical of a galaxy with strong star formation and abundant in young stars. As such, the SFH consists of a very strong recent burst of star formation.

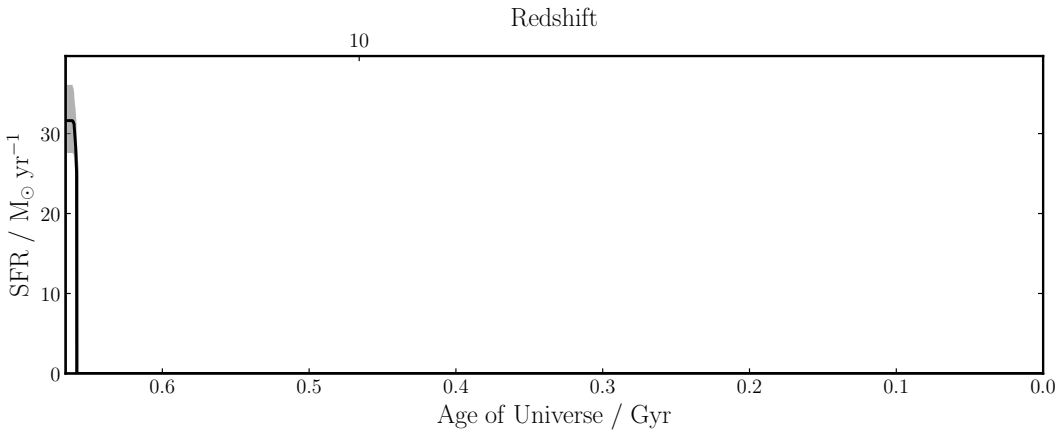

Figure 4.6: The star formation history estimated by BAGPIPES for image 11.1 under the assumption that its form is constant. The best fit SFH is very intense burst of star formation recently in the galaxy's history.

4.2.3 BAGPIPES Run #2: Delayed exponential star formation

Table 4.6 contains the priors for the delayed exponential star formation model. As in the constant star formation version, while the prior for the time since the start of star formation can be up to 2 Gyr, BAGPIPES will automatically prevent any ages longer than the age of the Universe at the fitted redshift. The Universe is approx. 0.7 Gyr old at z$\sim$7.5, and the age cannot be more than that.

Parameter	Prior
Age (time in Gyr since start of star formation)	[0, 2]
Timescale τ	[-1, -0.001]
Mass formed $log(M^*/M_\odot)$	[7, 11]
Metallicity $Z/Z_\odot$	[0,2]

Table 4.6: Priors of the delayed exponential model provided to BAGPIPES when fitting the spectrum of the System 11 images.

Parameter	Posterior	
	Image 1	Image 2
Mass-weighted age (Gyr)	$0.013^{+0.004}_{-0.003}$	$0.009^{+0.005}_{-0.002}$
Mass formed $log(M/M_\odot)$	$7.64^{+0.05}_{-0.05}$	$7.64^{+0.09}_{-0.04}$
Star formation rate $M_\odot/yr$	$4.7^{+0.6}_{-0.5}$	$5.6^{+0.2}_{-0.2}$
Metallicity $Z/Z_\odot$	$0.3^{+0.1}_{-0.1}$	$0.09^{+0.01}_{-0.01}$
Timescale τ	$-0.5^{+0.3}_{-0.3}$	$-0.5^{+0.3}_{-0.3}$
Dust extinction A_V	$0.10^{+0.06}_{-0.04}$	$0.09^{+0.03}_{-0.02}$
Dust factor η	$2.5^{+1.9}_{-1.0}$	$3.9^{+1.3}_{-1.0}$
Redshift	$7.667^{+0.006}_{-0.006}$	$7.650^{+0.005}_{-0.006}$

Table 4.7: Posterior parameters of the model with delayed exponential star formation history. The mass and star formation rate have been scaled by the magnification.

Table 4.7 contains the posterior parameters and their confidence intervals for the delayed star formation history SEDs shown in Fig. 4.7. The mass and star formation rate are scaled by the magnification of the images. The posterior probability distributions in the corner plot in Fig. 4.8 show the same degeneracy between A_V and η found in the constant version. The redshift, metallicity, and mass are well constrained. However, the timescale of star formation τ is poorly constrained by BAGPIPES, showing multiple peaks in probability across its range.

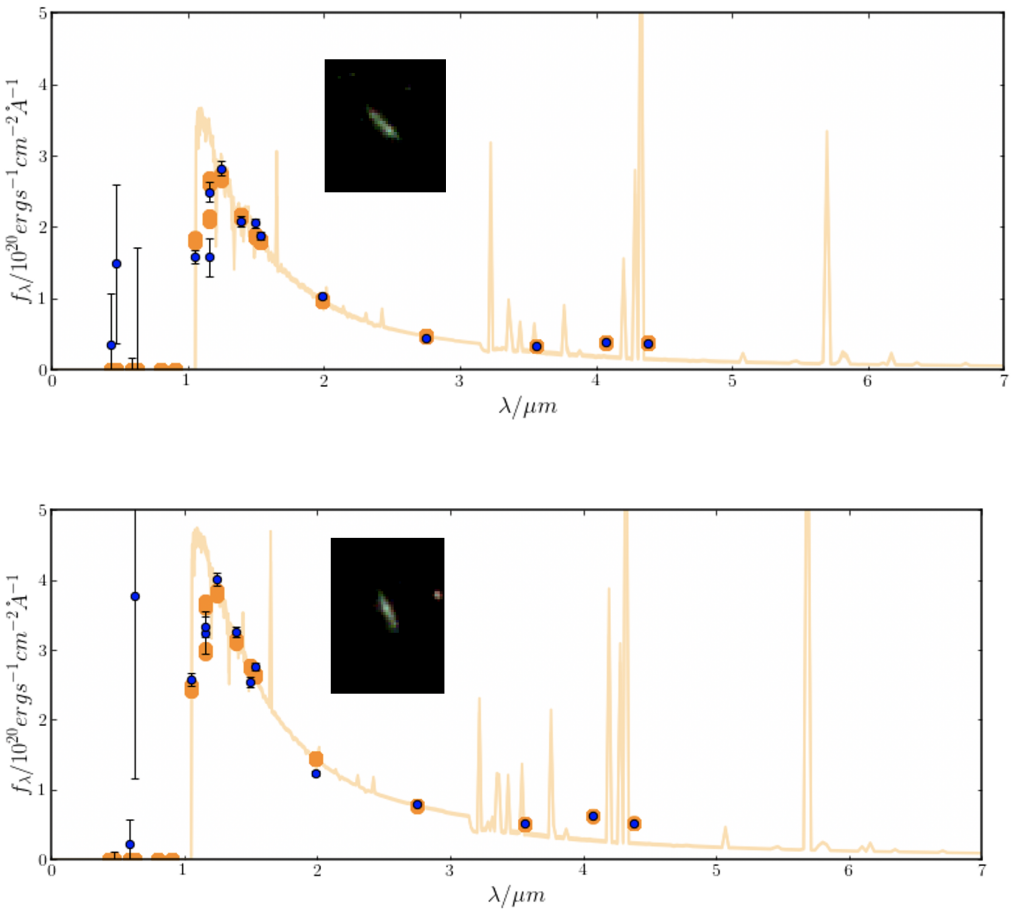

Figure 4.7: The SEDs of System 11 fitted by BAGPIPES under the assumption of a delayed exponential star formation history. An RGB NIRCAM image of the galaxy is overlaid on the plot. Note that the flux is the observed flux and has not been scaled by the magnifications of the images.

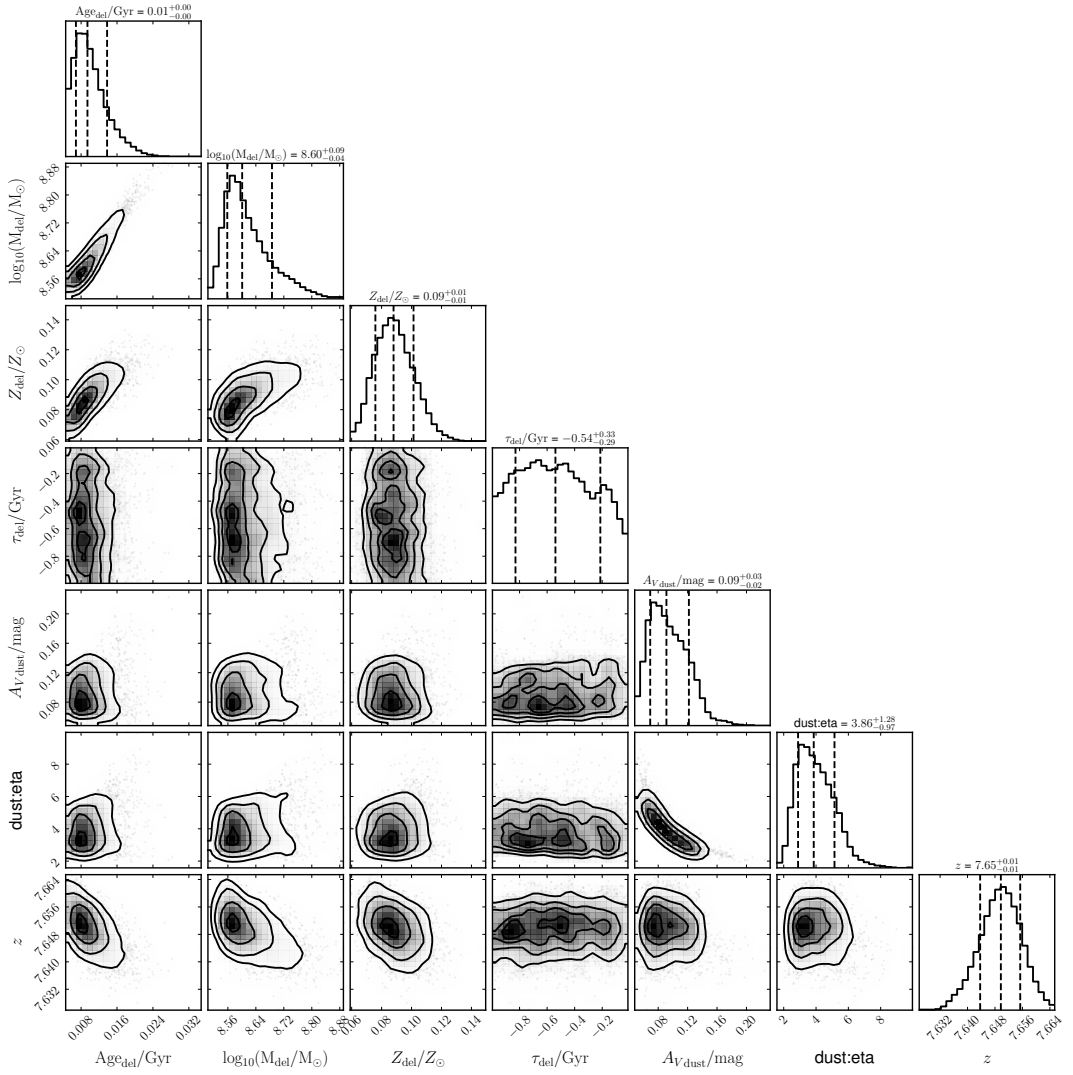

Figure 4.8: A corner plot showing the posterior probability distributions of each free parameter fit by BAGPIPES for Image 11.2 when the star formation history is a delayed exponential.

Similar to the constant star formation rate version, the estimated star formation history features a short intense burst of star formation in the galaxy's recent history (Fig 4.9).

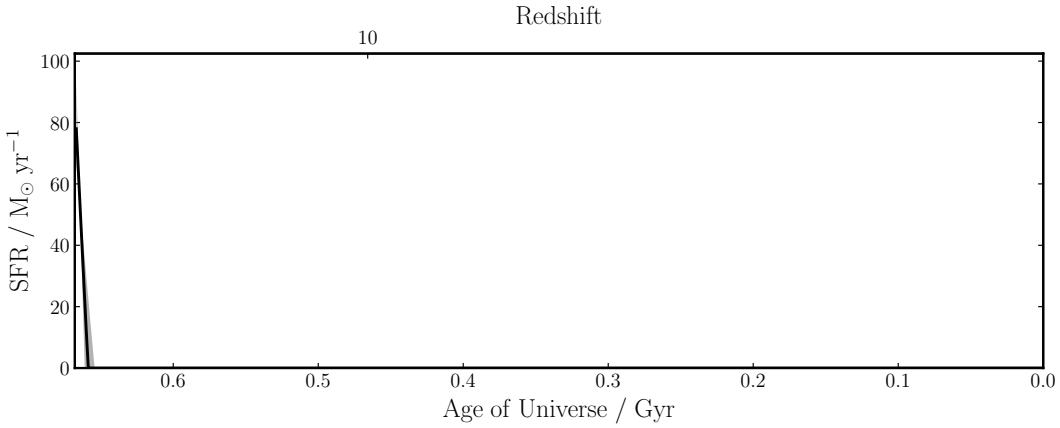

Figure 4.9: The star formation history estimated by BAGPIPES for image 11.2 under the assumption that its form is that of a delayed exponential. The best fit SFH is a rapid increase in star formation recently in the galaxy's history.

I will compare the two runs and discuss the effects of including JWST photometry compared to HST-only in Section 5.2.

4.2.4 NIRISS extraction

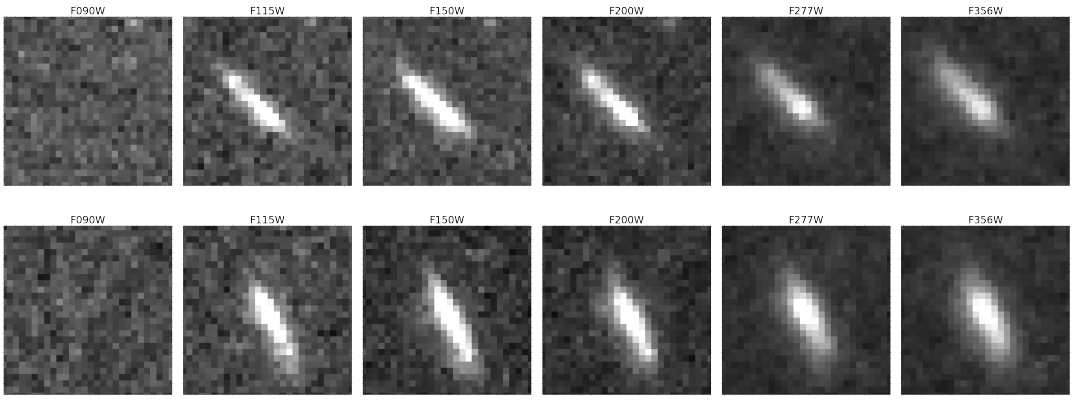

Figure 4.10: The images of System 11 (top: image 1, bottom: image 2) in each of the JWST NIRCAM filters. The dropout between the F115W and F090W filters is clearly visible.

System 11 was estimated to be one of the highest redshift galaxies in the Abell 370 field, with a photometric redshift of 7.84±0.02 (Strait *et al.*, 2018). Looking at the photometry, the galaxy drops out between the F115W and F090W filters, as seen in Fig. 4.10. Extracting the spectrum of both images with GRIZLI in Fig. 4.11 and Fig. 4.12, I find that while the spectrum has a low

signal-to-noise ratio, the Lyman break at approximately 1.1 microns is clearly visible in both images. From this spectral feature, I find a spectroscopic redshift of $7.76^{+0.03}_{-0.04}$ for image 1 and $7.624^{+0.032}_{-0.003}$ for image 2. The two measurements are consistent with each other within a 68% confidence interval. The mean of the two measurements, 7.69 ± 0.04 is taken as the redshift provided to LENSTOOL in the multiple images catalogue.

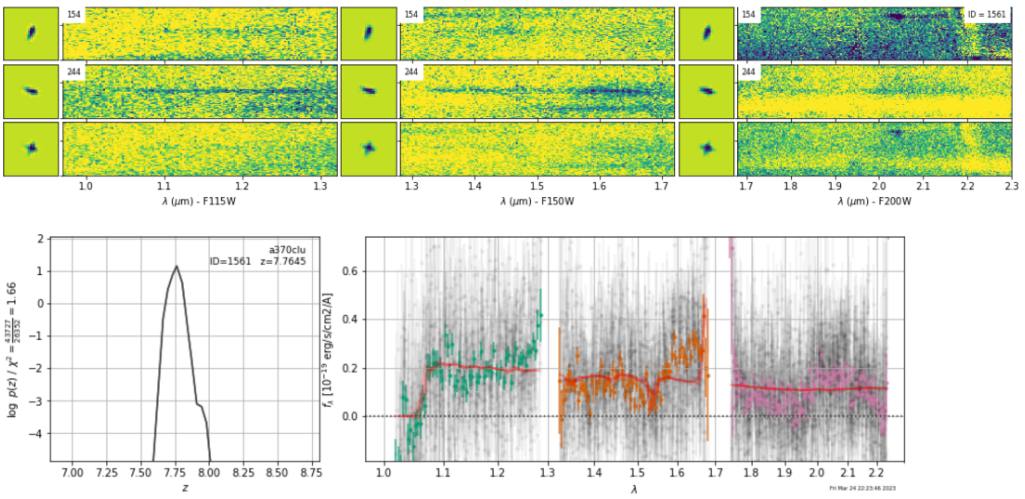

Figure 4.11: Top: The 2D NIRISS spectrum of System 11, image 1. Bottom left: The posterior probability distribution for redshift found by GRIZLI for this system. Bottom right: The 1D spectrum extracted by GRIZLI. The signal to noise is low but the Lyman break at approx. 1 microns is clearly visible.

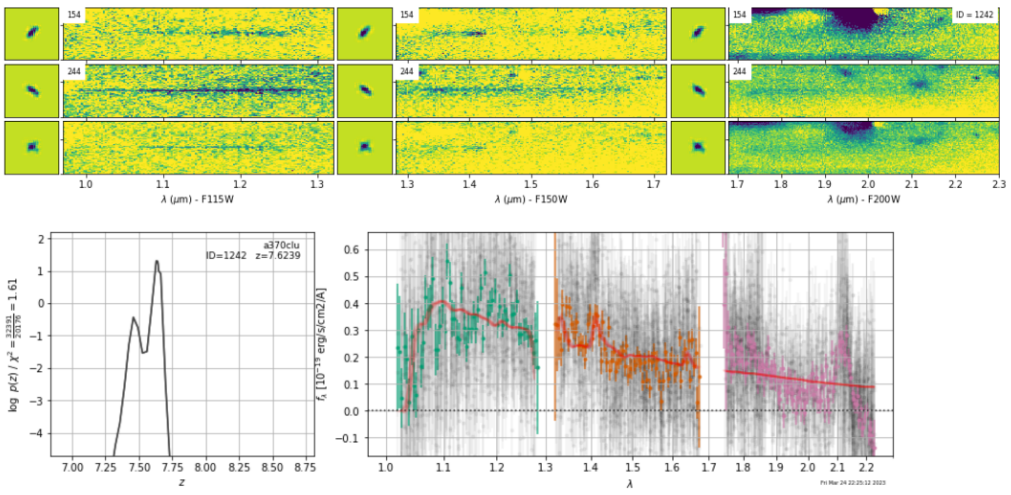

Figure 4.12: Same as Fig. 4.11 but for Image 2 in the system. The exact redshift found for the 2 images is slightly different, but the distributions overlap and the Lyman break is visible at the same wavelength.

5 Discussion

In this chapter, I will discuss how well my best-fit lens model of Abell 370 fits the data, and suggest some ways that the model can be improved in future work (Section 5.1). I will also compare the results of the different BAGPIPES runs with different prior assumptions and discuss the impact of adding JWST photometry to the pre-existing HST data in Section 5.2.

5.1 Lens model

The goodness of fit statistics for the final best lens model are given in Table 5.1.

	Statistic
Reduced chi-squared χ^2/ν	4.23
Degrees of freedom ν	59
Bayesian evidence	-10.7
Median rms deviation	1.09"

Table 5.1: Statistics describing the fit of the best lens-model. The χ^2 and evidence are provided as an output by LENSTOOL, while the rms deviation was calculated based on the distance between the images reconstructed by LENSTOOL and the actual positions of the real images.

The best model I found for Abell 370 during this project features 5 dark matter halos and 4 individually modelled galaxies; shown in Fig. 4.2 and described in Section 4.1. When any of these components were removed from the model

and LENSTOOL was run again with optimization on and moderate ranges for the other potentials, the statistics of the fit worsened to varying degrees, as demonstrated in Table 5.2. When an additional potential was added, the reduced chi-squared statistic improved slightly, but the evidence worsened; this indicates that the model was beginning to over-fit the data. While it is likely that I have not explored the complete parameter space for my lens model, I can say that the choices of potentials are physically motivated and better than similar variations. Below, I will discuss improvements that can be made in future work.

Change in model relative to best-fit model	ν	χ^2/ν	Evidence
DM1 removed	65	8.26	-154.9
DM2 removed	65	16.6	-462.3
DM3 removed	65	6.50	-92.9
DM4 removed	65	4.45	-27.1
DM5 removed	65	5.31	-57.7
Extra halo potential added	53	4.13	-20.9
GAL1 removed	61	4.17	-30.2
GAL2 removed	60	4.13	-14.6

Table 5.2: Reduced chi-squared and Bayesian evidence statistics for versions of the best model without each of its potentials, and with an additional potential

5.1.1 Problem systems and possible improvements

For the most part, this model reconstructs the positions of the multiple image systems well. Figure 5.1 shows an example: the red circles mark the actual positions of the images of System 1. The green ellipses represent the reconstructed images. A perfect model would have 3 reconstructed images exactly on top of the real images. There is a small separation, but the reconstructions are quite good - an average of 0.53 arcseconds separated from the original positions. Of the 78 images in the Gold multiple images catalogue, 70 have a root mean square deviation less than 2 arcseconds.

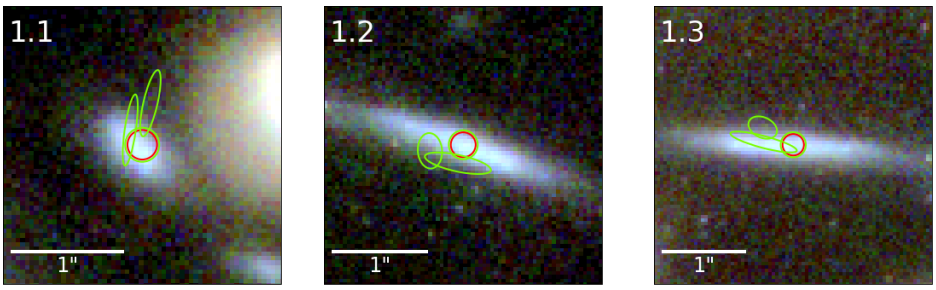

Figure 5.1: The images of System 1, given as an example of a system well-reconstructed by the best model. The original positions provided to LENSTOOL are plotted in red, while the reconstructed images are plotted in green

There are a few 'problem systems' where the model does not accurately predict where the images are. The first of these is System 2, the giant luminous arc in the cluster, shown in Fig. 5.2. This system is a particular challenge because it is difficult to be certain how many distinct images it contains. Previous works have used different numbers of images; Lagattuta *et al.* (2019) uses 5 images, Diego *et al.* (2018) also uses 5, with numerous knots, and Strait *et al.*, 2018 uses 4 images. Here I have decided to use 4 images centered on where we see the red core of the galaxy in the arc. This system is also complicated by the fact that the nearby cluster member near images 2.3 and 2.4 is galaxy-galaxy lensing the arc to some degree - if we look closely, we can see the arc curve around the galaxy. The cluster member was included as a separately optimized galaxy to attempt to account for it, but this only slightly improved the fit. More work is needed to model this system correctly.

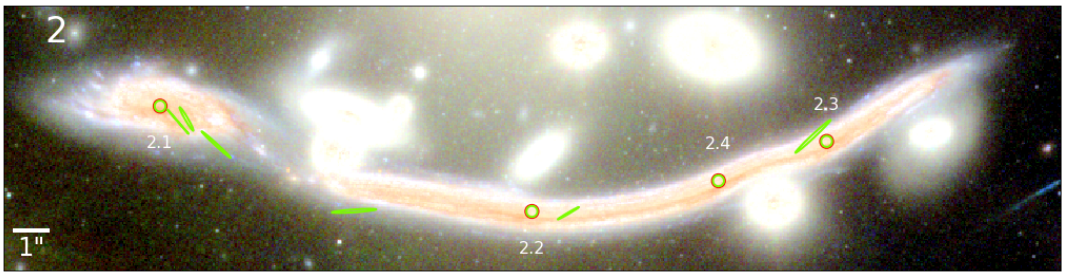

Figure 5.2: The original (red) and reconstructed (green) images of System 2, the giant luminous arc. The images in the arc are poorly predicted by my lens model.

System 3 is another system in which the model struggles to predict the images correctly. This is one of the systems where I included 2 knots. Adding the

DM4 potential to the north-west region of the cluster, and modelling nearby cluster member Gal 3 separately from the rest improved the fit somewhat, but as shown in Fig. 5.3, the fit is still poor. The next step to try with this system is to attempt to include more knots, which will hopefully provide LENSTOOL with enough information to model this system with more accuracy.

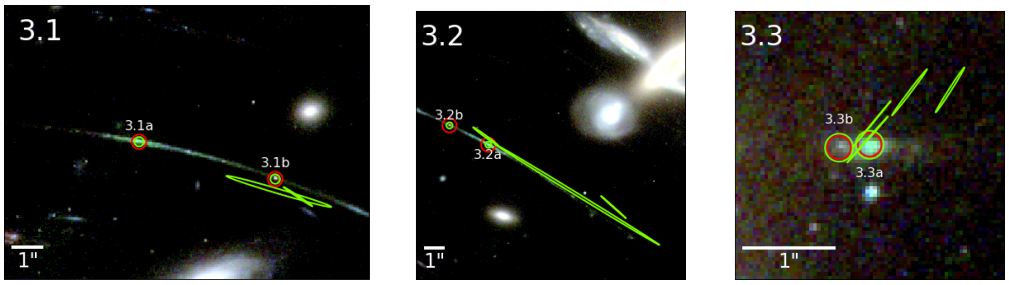

Figure 5.3: The images of System 3, The original positions provided to LENSTOOL are plotted in red, while the reconstructed images are plotted in green.

Possibly the worst constrained system in our sample is System 5, shown in Fig. 5.4. Adding DM5 to the south end of the cluster improved the fit; this changed the path of the critical curve for a source at System 5's redshift such that it weaves between the images. Except for Image 5.1, the images are very poorly predicted by the model. The next step in attempting to improve this system is to try to model the cluster member galaxy in between Image 5.1 and 5.2 as a separate potential.

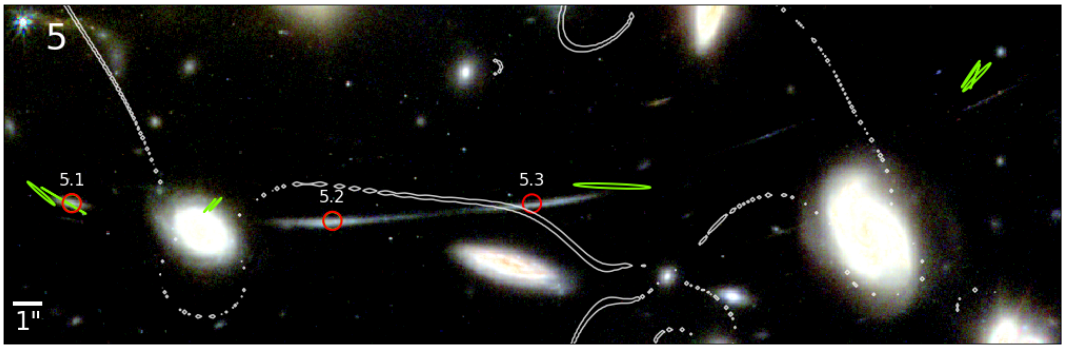

Figure 5.4: The original (red) and reconstructed (green) images of System 5. Contours of the magnification map showing the critical curve for a source with System 5's redshift, z = 1.2775 are also plotted in white. While the critical curve is close to where we would expect for the system, weaving between the images, the reconstructed images for this system are very poorly predicted by our lens model.

Note that the images with poor rms deviation are not concentrated in any particular area of the cluster, but scattered across the field.

In general, the model has more success predicting the positions of compact images compared to more extended ones, as evidenced by the fact that the only well predicted images of Systems 3 and 5 are the smaller images 3.3 and 5.1. One possible improvement I could make to try to combat this problem would be to try to include some ellipticity information in the multiple images catalogue. An even more detailed way to describe the shape of the lensed galaxies would be to also include flexion, a measurement of the curvature of the images; though to my knowledge no strong lens modelling code currently implements this (Cain *et al.*, 2011).

An additional possible improvement to the model would be to include ellipticities for the cluster members. At this time, I do not have ellipticity measurements derived from the JWST data; modelling the stellar light in the cluster is an upcoming step. I have ellipticity measurements for HST-selected cluster members, 80 out of the 280 in my sample and ran a test where the ellipticity information was removed from the catalogue and the same LENSTOOL parameter file was run both with and without ellipticity. The version with circular cluster members was only slightly worse in fit statistics (a difference in χ^2 of about 4%) than the version that included the shape of the galaxies. It is unlikely that the majority of the systems are much affected by the shape of the cluster members because their potentials are less massive and more compact than the larger dark matter halos in the model, however this may not be the case when an image is close to a cluster member galaxy, as in System 5 for example. In future versions of this model, we could fit Sersic profiles to the cluster member galaxies in order to provide more detailed shape information to LENSTOOL.

Future versions of this model could also use alternative parameterizations for the cluster members that produce different mass-to-light ratios. There is scatter in the mass-size-light relationship in any distribution of galaxies, which could result in individual galaxies needing to be treated separately by the model, but it is possible that other values for the exponents in Equations 3.4 and 3.5 may result in an improved fit.

Lastly, it is worth reiterating that lens modelling is a very computationally expensive process. There are many parameters, including those used to constrain the halo potentials, and those used to scale the mass to light ratio for the cluster member galaxies. In addition, some of the parameters are degenerate with each other, particularly velocity dispersion, core radius, and cut radius. The different potentials can also compensate for each other to some degree - one potential decreasing in mass or size while another increases can lead to similar results. By iterating the lens modelling process and adjusting the parameter ranges each time, we attempt to help LENSTOOL find a minimum, but there is a reasonable probability that it has found a local minimum instead of the global one. It is highly likely that more computational power and time would yield improved, better minimized results.

5.1.2 Magnification errors

I calculated the errors on the magnification across the cluster by taking the model parameters from the last 100 MCMC iterations performed by LENSTOOL during its optimization. I ran LENSTOOL without optimization for each model, making a κ and γ map each time. Using Equation 2.12, I calculated the magnification. I took the difference between the 16th and 84th percentiles of the distribution of magnifications in each pixel as the error on the magnification.

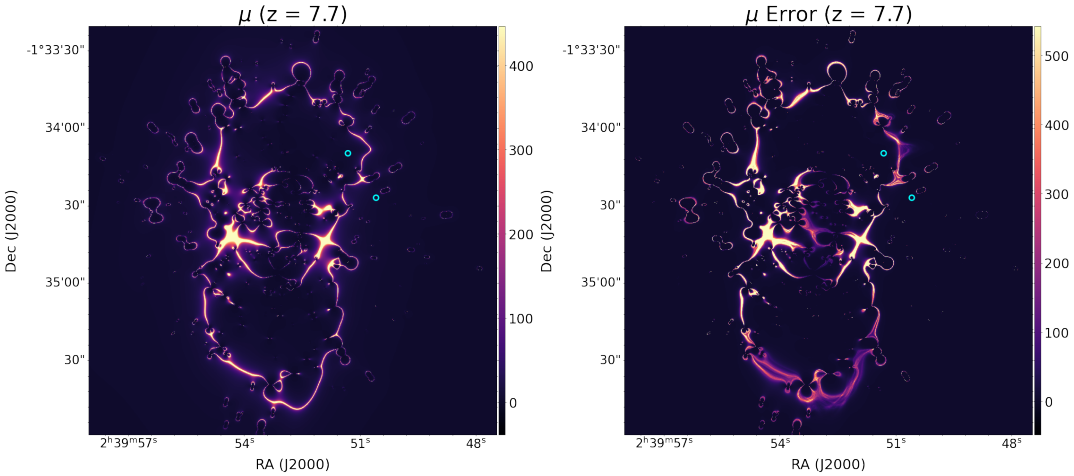

Figure 5.5: The magnification map of the best model (left) next to the magnification error for a source at the redshift of the System 11 galaxy. Note that the error increases to extremely high values near the critical curve. Blue circles mark the coordinates of the System 11 images.

Fig. 5.5 shows the distribution of the magnification error beside the magnification for a source at the same redshift, that of the System 11 galaxy. Note that the magnification error gets extremely high near the critical curve - high enough to make the value for the magnification on or close to the critical curve near-meaningless. When studying background galaxies in lensing clusters, the sources that are highly magnified are valuable because their high brightness makes them easier to study. However, it is important to consider that any absolute properties derived for the most magnified galaxies will be extremely uncertain.

5.1.3 Comparisons to other models

There are two main methods of lens modelling - parametric and non-parametric. Parametric codes, like LENSTOOL define a model, such as our set of PIEMD dark matter halos and cluster member galaxies, and then explore the parameter space of the assumed distributions to find the best fit to the data. By contrast, non-parametric lensing codes do not make direct assumptions about the shape of the matter distribution in a cluster. Instead, they divide the cluster into a grid, which can be a regular grid or an adaptive mesh, and place mass across the cluster.

Fig. 5.6 shows a magnification map for a source at z = 9.0 for my best model alongside the same plot for 3 other lens models of Abell 370. The top row - my model and that found by the Glafic team (Kawamata *et al.*, 2016, Oguri, 2010) are both parametric models. Glafic is similar to LENSTOOL in that it features a number of halos with optimized parameters, however there are some differences: their model features Navarro-Frenk-White (NFW) density profiles instead of PIEMD profiles for the larger halos, and uses a single parameter for the size instead of defining r_{core} and r_{cut} separately. The cluster member galaxies are also parameterized with a different profile.

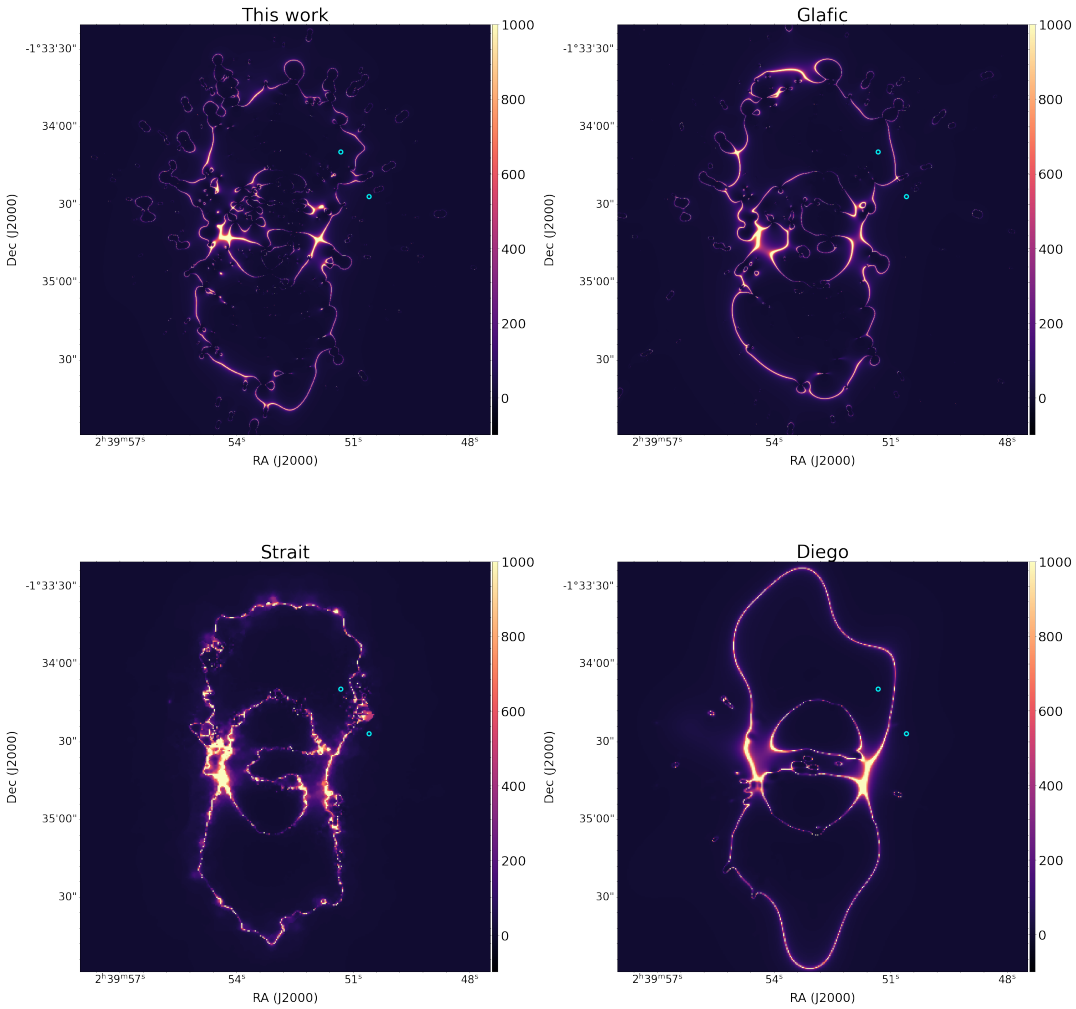

Figure 5.6: A comparison of magnification maps for a source at z = 9.0 found by several different works. The Glafic model is made using a different parametric lensing code, while Diego used a non-parametric code that assumes that light traces mass. Strait *et al.* (2018) also used a non-parametric code; one that does not assume light traces mass and also incorporated weakly lensed sources as constraints.

The bottom row of Fig. 5.6 are both non-parametric models. Diego *et al.* (2018) uses a code called WSLAP+ (Diego *et al.*, 2005). WSLAP+ models the surface mass density in the cluster by using a superposition of Gaussians to describe the overall mass, and assigning a mass to each cluster member based on its surface brightness. The field is divided into a regular grid, and each grid point contains a Gaussian function of surface mass density.

Strait *et al.* (2018) used the code Strong and Weak Lensing United, which uses both strong and weakly lensed sources as constraints. As a non-parametric code, it does not make any assumptions about the profile of the mass dis-

tribution beyond the choice of initial model. Unlike the Diego *et al.* (2018) model, it also does not assume that light traces mass, i.e. that the overall mass distribution must have concentrations where the light is in the cluster.

There are various methods and prior assumptions one can make when lens modelling. Opinions differ on whether parametric or non-parametric methods are more robust. Some argue that parametric methods are sufficient to describe the surface mass distribution in a cluster without adding unnecessary degrees of freedom to the model (Schneider *et al.*, 2006). Others would say that little is known about the true profile of dark matter in galaxy clusters and it is better to avoid making assumptions about the shape of its profile and/or to what degree the distribution of dark matter matches the distribution of stellar light (Saha *et al.*, 2006, Strait *et al.*, 2018).

When considering the question of how matter is distributed across Abell 370, it is valuable to have different models that all approximately reproduce the positions of the strongly lensed images in the cluster. The different models have approximately the same shape but differ in the exact position of the critical curve, as well as its smoothness. The magnification map is the main data product created in the lens modelling process - it is necessary for many applications when studying the background galaxies. Having many magnification maps available helps us understand the systematic uncertainties that arise from the different assumptions made when constructing lens models.

5.2 SED fitting System 11

In this section, I will discuss what we can learn from the SED of the 2 images of the System 11 galaxy. I will also explore the consequences of varying the star formation history and other priors on the SED fit, as well as the effects of including the new JWST photometry.

5.2.1 System 11 in context

Historically, it has been difficult to confirm the redshifts of distant galaxies. Because photometric redshifts derived from SED fitting can be unreliable -

the SED of a low-redshift galaxy with an old or dusty stellar population can be very similar to a high-redshift galaxy with a younger stellar population - it is very valuable to have a trustworthy redshift derived from spectroscopic data when attempting to constrain the properties of the galaxy (Fujimoto *et al.*, 2022, Arrabal Haro *et al.*, 2023). Fig. 5.7 shows both that the number of spectroscopically confirmed galaxies at high-redshift is small and that photometric redshifts have a high probability of being inaccurate (Adams *et al.*, 2023).

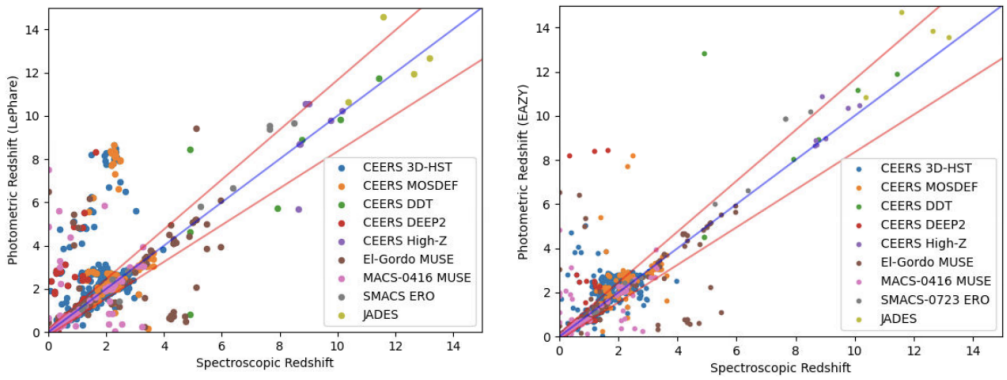

Figure 5.7: A comparison of photometric redshifts found with SED fitting codes LePhare (left) and EAZY (right) to spectroscopic redshifts for the same galaxies, drawing from the results of several studies. The blue line marks where the two methods would be equal and the red lines are 15% offsets in 1+z. Note that the error in photometric redshift can be very large. Credit: Adams *et al.*, 2023.

Until the recent availability of data from JWST, the number of spectroscopically confirmed galaxies at z>7 was low but it is now rapidly increasing. When investigating the evolution of galaxies over cosmic time, our understanding can only improve by having more reliable data with lower uncertainties. I calculated the absolute magnitude of the System 11 galaxy by scaling the F125W flux, which is the filter that best matches UV in the rest-frame by the magnification. I then converted the flux to AB magnitude, and used the luminosity distance to convert to absolute magnitude. Image 1 has M = $-21.51^{+0.22}_{-0.27}$ and Image 2 has M = $-21.43^{+0.09}_{-0.10}$; note that these values are in agreement.

5.2.2 HST vs JWST+HST

In addition to running BAGPIPES with different star formation histories, I also ran it with 2 different photometry catalogues - one including only measurements from HST, and one including both HST and JWST photometry. In this section, I will discuss the effects of adding JWST photometry to the pre-existing HST photometry when fitting the SED of the System 11 galaxy. The two best-fit spectra found by BAGPIPES with constant and delayed exponential star formation histories are displayed in Fig. 5.8 and Fig. 5.9 respectively. All priors for the fit were the same as described in Chapter 3, the only difference between the fits was the photometry data.

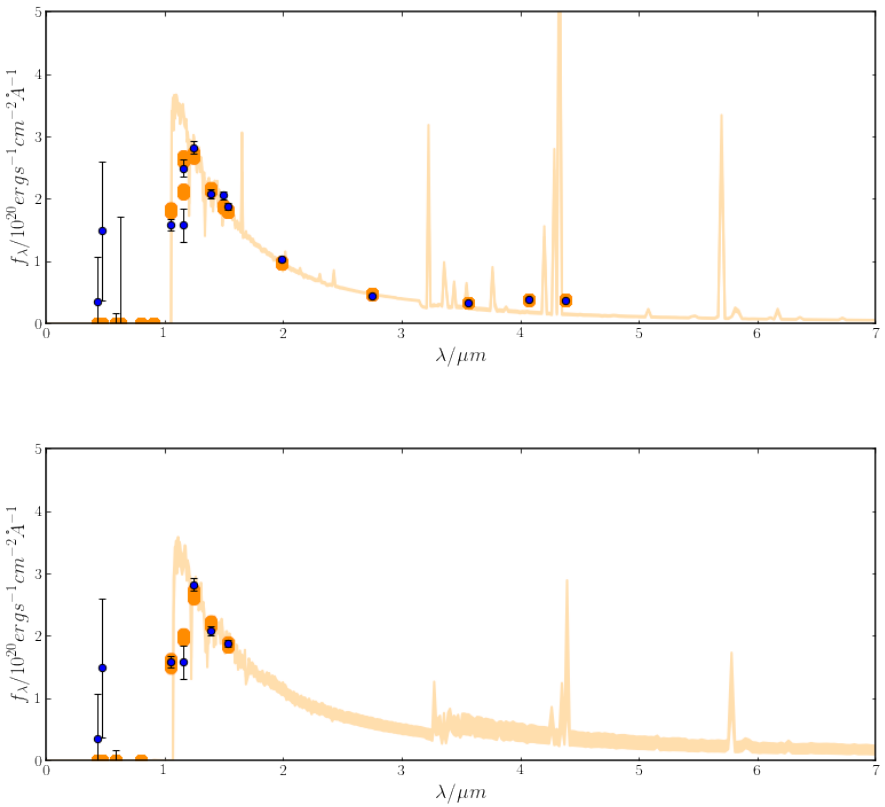

Figure 5.8: The SED fits under the assumption of exponential delayed star formation histories for Image 1 when the photometry is restricted to only HST filters (top) and when both JWST and HST filters are included.

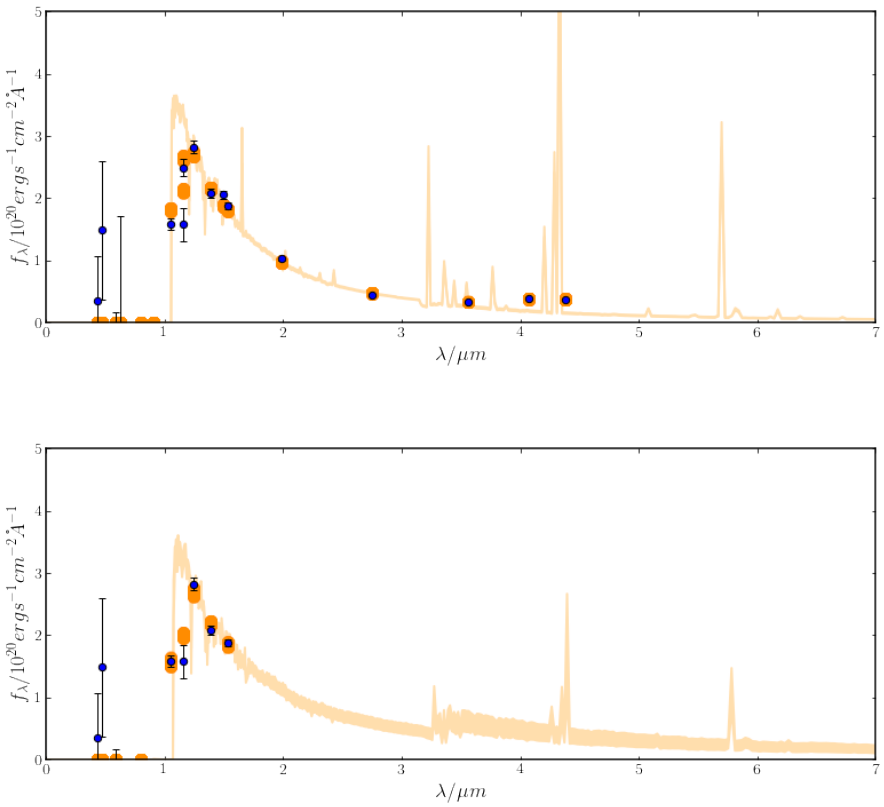

Figure 5.9: The SED fits under the assumption of constant star formation histories for Image 1 when the photometry is restricted to only HST filters (top) and when both JWST and HST filters are included.

Fig. 5.10 shows posterior distributions of the mass, mass-weighted age, and star formation rate over the 10 Myr prior to observation. The first thing to note is that the distributions including both HST and JWST photometry are narrower and therefore better constrained. The corner plot of the fit when only HST photometry is included, shown in Fig. 5.11, is another way to visualize this - compared to the corner plot in Fig. 4.8, the parameters are more poorly constrained. This is in part because as seen when comparing the star formation histories in Fig. 5.12 to those presented in Figs. 4.9 and 4.6, the uncertainty on the star formation history is much smaller when JWST photometry is included. Many of the emission lines that constrain star formation are found in the region of the spectrum too red for HST filters.

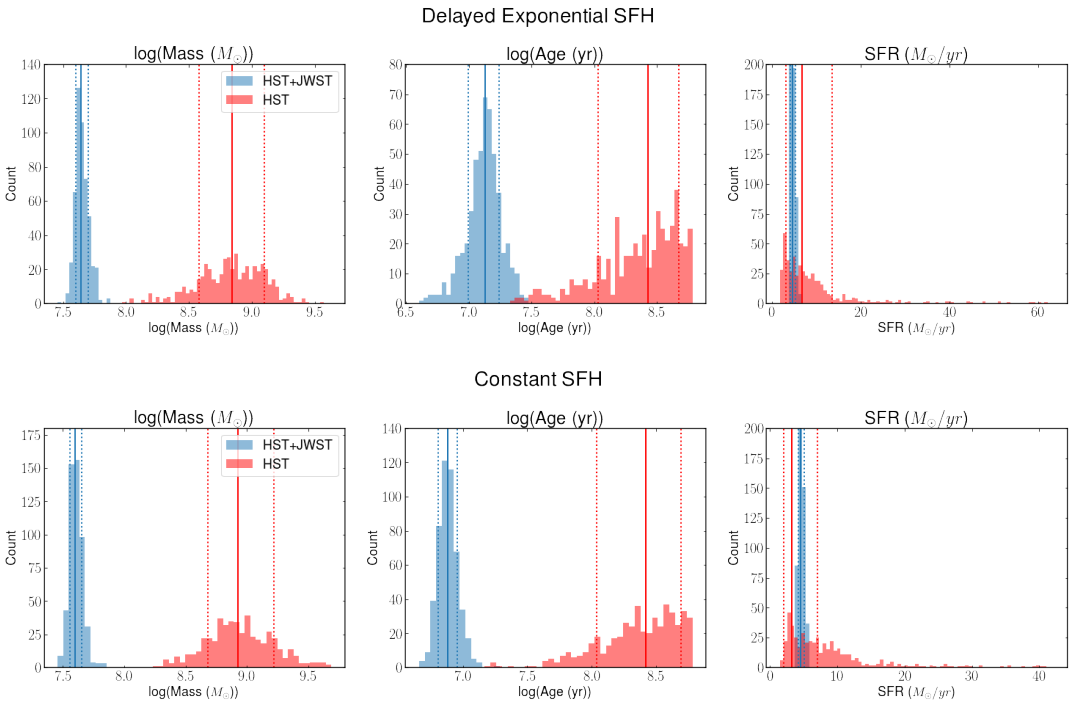

Figure 5.10: The posterior probability distributions of the mass, age, and average star formation rate over the last 10 Myr of Image 1 in the delayed exponential formation case (top) and the constant star formation case (bottom). The red histogram represents the posterior when the photometry data provided to BAGPIPES is restricted to HST filters only, while the blue histogram includes both HST and JWST filters. The solid vertical lines show the median of the distribution, and the dotted lines show the 16th and 84th percentiles.

The posterior distributions for the parameters show that the spectrum fit by BAGPIPES when the new JWST photometry is added is younger and less massive than that found with only HST photometry. Given the star formation histories shown in Fig. 5.12, it makes sense that the stellar population would be older as its history starts earlier.

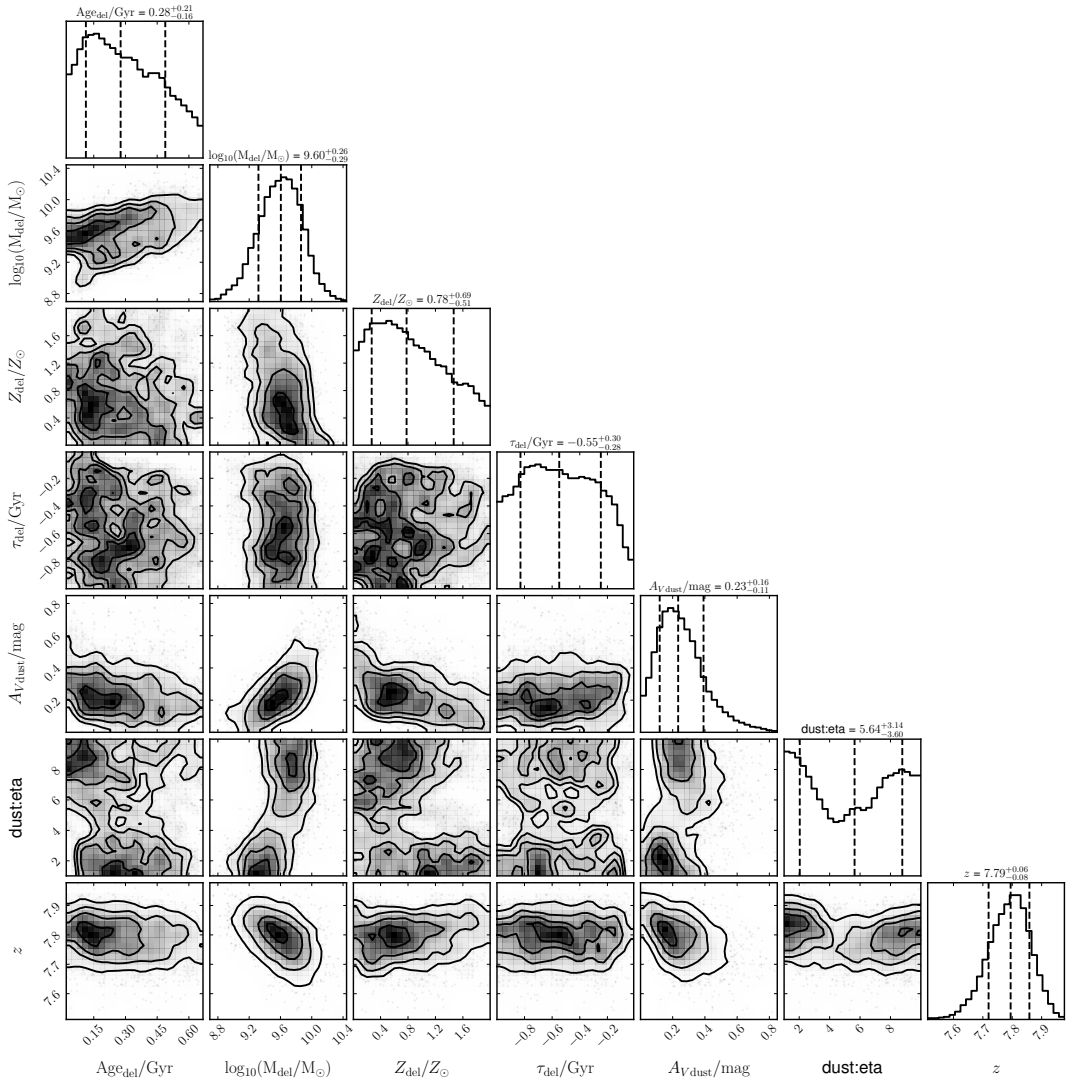

Figure 5.11: A corner plot showing the posterior distributions of the HST-only SED fit for Image 1 with exponential delayed star formation history. Compare to Fig. 4.8 for the equivalent plot when JWST photometry is included in the fit.

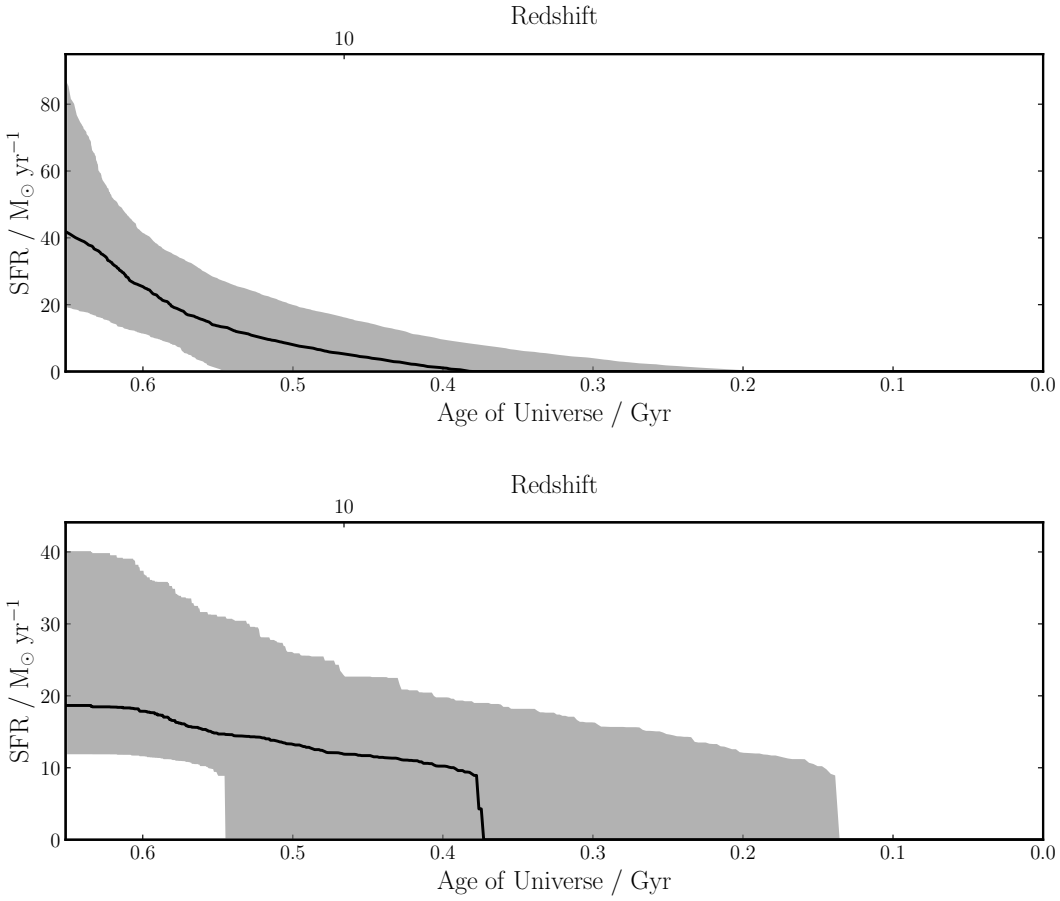

Figure 5.12: The posterior delayed exponential (top) and constant (bottom) star formation histories when BAGPIPES is run with HST photometry only. The grey region represents the uncertainty on the star formation history.

5.2.3 Constant vs. delayed exponential star formation history

When reporting the properties of a high-redshift galaxy derived from SED fitting, it is important to consider the effects one's choice of prior assumptions has on the results. Fig. 5.13 shows the posterior probability distributions of the mass, mass-weighted age, and star formation rate averaged over the 10 Myr prior to observation time for SED fits using both the delayed exponential and constant star formation histories. The delayed exponential SFH results in a slightly older and more massive stellar population than the constant SFH.

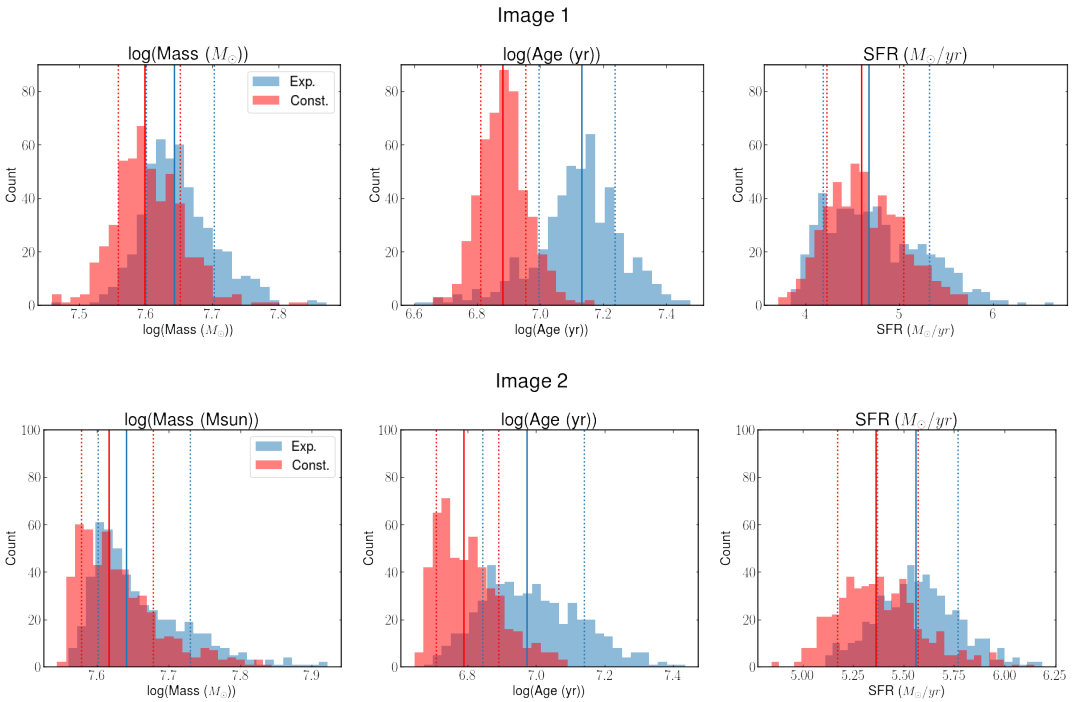

Figure 5.13: The posterior probability distributions of the mass, age, and average star formation rate over the last 10 Myr of Image 1 (top) and Image 2 (bottom). The red histogram represents the posterior when the SFH is constant, while blue represents the delayed exponential SFH. The solid vertical lines show the median of the distribution, and the dotted lines show the 16th and 84th percentiles.

In this analysis we have used two simple, but commonly used, parameterizations for the star formation history of this galaxy. A disadvantage of this approach is that the simplicity of the function used to describe the star formation rate over time can limit the fit to consider only the most recent star formation in the galaxy's history. Simulations predict that star formation in young galaxies is not constant but features multiple bursts of intense star formation separated by quiet periods where the star formation rate is low (Ma *et al.*, 2018). When a single form is used to describe the star formation history, older populations of stars can be ignored in favour of only the brightest new bursts of star formation. If that is the case, then both the mass and the mass-weighted age of the galaxy are likely underestimated. Fig. 5.14 shows examples of star formation histories from galaxies simulated using the Feedback In Realistic Environments (FIRE) project.

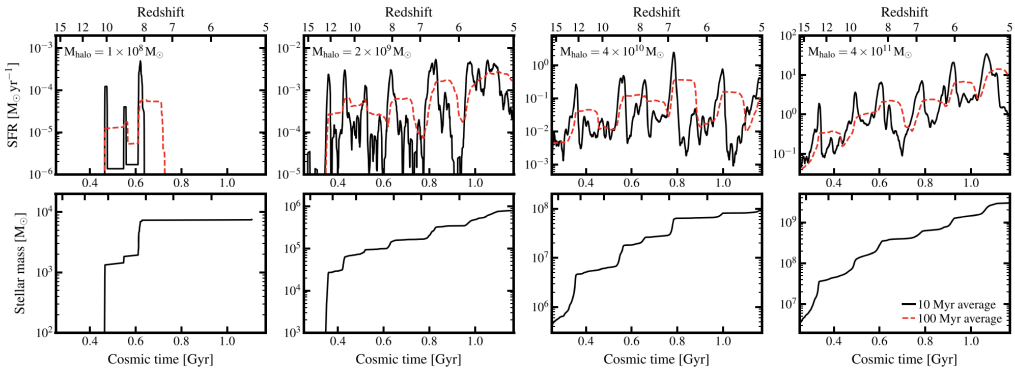

Figure 5.14: The star formation histories (top) and stellar mass formation histories (bottom) of several galaxies with different masses simulated with FIRE. The red dashed lines show the SFR averaged over 100 Myr timescales and the solid black line is the SFR averaged over 10 Myr. Note that the simulations predict many bursts that increase the star formation rate by an order of magnitude or more. Credit: Ma *et al.*, 2018

An alternative approach is to consider non-parametric star formation histories. Instead of using an equation like the delayed exponential described in Equation 3.10 to describe the star formation rate as a function of time, a non-parametric SFH is allowed to vary smoothly over bins in lookback time. This method avoids bias because the user doesn't need to choose a functional form for the star formation history and allows for multiple bursts of star formation. Fig. 5.15 shows some examples of non-parametric star formation histories. The SFH of a simulated galaxy is reconstructed with the non-parametric code Dense Basis (Iyer *et al.*, 2019) with varying numbers of time bins. The time bins are determined by percentiles of mass formed during the bin such that the time interval is smaller when the star formation rate is higher. With relatively few bins, the non-parametric code is able to approximate the true SFH quite closely.

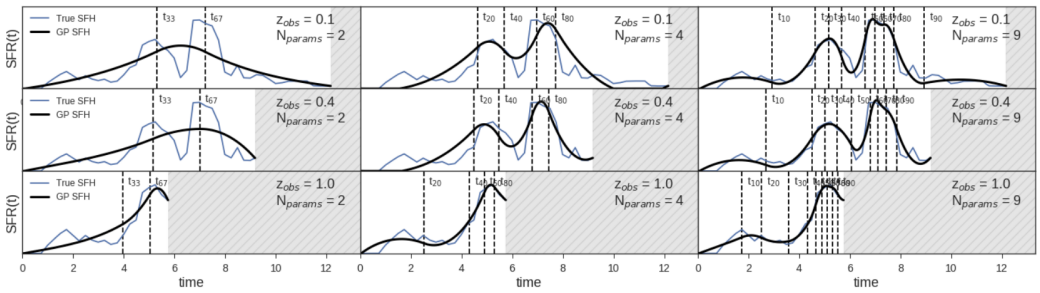

Figure 5.15: An example of a non-parametric SFH form fitted to the star formation history of a simulated galaxy using the code Dense Basis. The blue lines represent the true SFH of the galaxy, while the black lines show the reconstructed SFH calculated over different numbers of bins. Credit: Iyer *et al.*, 2019

Comparing SED fits of System 11 using non-parametric star formation histories with the parametric forms presented here will be a focus of future work for this galaxy.

5.2.4 Other priors

We have demonstrated that the form of the star formation history provided to BAGPIPES can be an assumption that has a significant impact on the final results. In this section, we will briefly explore other priors and their effect on the posterior parameters.

The Calzetti dust attenuation curve used in this project is a commonly used function describing how dust extinction varies with wavelength (e.g. Grillo *et al.*, 2015, Carnall *et al.*, 2018, Strait *et al.*, 2021). It is derived from observations of our local population of starburst galaxies. Starbursts are relatively rare in the local Universe, but are thought to be the closest analogs to galaxies at z>1 (Salim *et al.*, 2018). While dust attenuation curves are used to constrain the properties of high-redshift galaxies, we do not know if these relationships hold at earlier times in the history of the Universe. The properties of dust depend on the stellar populations responsible for its formation and the properties of the interstellar medium surrounding it; both could be very different at high-redshift (Markov *et al.*, 2023).

When the BAGPIPES dust curve prior is changed to the Salim *et al.* (2018) function, the posterior stellar mass increases by approximately $\sim$0.05 dex when the star formation history is a delayed exponential, and $\sim$0.3 dex when the star formation history is constant. The Salim curve is also derived from local galaxies, but using a larger sample than Calzetti and without selecting for high star formation rates. The ages are slightly older and the star formation rate slightly lower. Choice of dust curve can have a similar impact on the results as choice of star formation history.

The ionization parameter log(U) is another quantity that is unknown at high redshifts. However, when it was varied as a prior for BAGPIPES, there was no significant impact on the posterior parameters.

Lastly, I will note that while BAGPIPES does not contain the capability to change the initial mass function, the assumed IMF is also a prior assumption for the SED fits. Papovich *et al.* (2001) found that changing the IMF from the Salpeter (1955) IMF to the Scalo (1986) IMF can change the stellar mass derived from an SED fit by up to 0.6 dex. In addition, the degree to which the IMF evolves with redshift is an open question in astrophysics (Eldridge and Stanway, 2022).

6 Conclusion

In this project, I have constructed a new lens model of Abell 370 with LENSTOOL. Using MUSE spectroscopy of the field, I extracted a catalogue of 280 cluster member galaxies. In conjunction with NIRCAM images and MUSE and NIRISS spectra, I rated the multiple images of Abell 370 by confidence and determined a robust sample of 23 systems that have both very well determined redshifts and morphologies that match between the images. The best-fit lens model features 5 large potentials distributed across the cluster, 4 individually modelled cluster member galaxies, and the other cluster members fit with a mass-to-light ratio. The reduced chi-squared statistic of the fit is 4.23, and the majority of the systems can be reconstructed with minimal spread.

I have also spectroscopically confirmed the redshift of a high-redshift background galaxy in the cluster field. By extracting the spectra of its 2 images from slitless spectra taken with NIRISS and identifying the Lyman break, I find a redshift of 7.69 ± 0.04.

Using the SED fitting code BAGPIPES, the magnification map derived from the lens model, and the spectroscopic redshift of the system, I fit a model spectrum to new photometry data from both HST and JWST. I derive estimated quantities for the mass-weighted age, mass, star formation rate, metallicity, and dust extinction of the galaxy. I explore how those quantities change given two different prior assumptions about the star formation history of the galaxy.

My mass and magnification maps of Abell 370 will continue to improve with further iterations on the model - including more detailed shape information for multiple image systems and cluster members, and changes that will improve the fit on the problem systems. The magnification map will be a useful data product for those wishing to study lensed galaxies in this cluster in the future. I have also contributed a multiply imaged galaxy to the short list of spectroscopically confirmed sources at $z \sim 8$.

7 Appendix

This appendix contains the coordinates and magnitudes for the sample of cluster member galaxies used when lens modeling.

ID	RA (deg)	Dec (deg)	F814W
1	39.9769563	-1.5986203	21.841
2	39.9756001	-1.5977416	21.785
3	39.9718952	-1.5974092	23.302
4	39.9751731	-1.5973908	24.77
5	39.9732177	-1.5991269	20.482
6	39.965416	-1.5945828	25.172
7	39.9769691	-1.5962129	22.13
8	39.9740869	-1.5945067	23.693
9	39.9642227	-1.5947468	23.712
10	39.9721258	-1.5943131	21.237
11	39.9672995	-1.5924207	23.687
12	39.9613968	-1.593398	20.699
13	39.9716002	-1.5913543	24.707
14	39.9769322	-1.5909904	24.539
15	39.9786203	-1.5910352	23.195
16	39.9673561	-1.5904786	23.027
17	39.9695659	-1.5931185	20.06
18	39.9774605	-1.5902591	22.151
19	39.9678455	-1.5897315	24.82
20	39.964304	-1.5912054	20.774
21	39.9682265	-1.5915689	20.645
22	39.9791183	-1.589864	25.947
23	39.9646729	-1.5903461	21.133
24	39.9774716	-1.5887164	24.035
25	39.9617814	-1.5884533	24.979
26	39.9820519	-1.5874015	26.504
27	39.9787352	-1.5882227	23.689
28	39.9806029	-1.5887467	24.873
29	39.9826718	-1.5887767	23.614
30	39.9722387	-1.5893066	21.269
31	39.9697534	-1.5878078	24.289
32	39.9803086	-1.5875343	23.633
33	39.9821618	-1.5873687	24.463
34	39.9753662	-1.5869618	23.261

35	39.9590356	-1.5863073	25.926
36	39.9751965	-1.5879238	21.722
37	39.9659422	-1.5893149	20.767
38	39.9588579	-1.5873171	23.284
39	39.9575339	-1.5864821	22.855
40	39.9607664	-1.5858734	25.155
41	39.9754681	-1.5853537	25.042
42	39.9779768	-1.5848653	28.152
43	39.9710201	-1.5857889	23.816
44	39.9726988	-1.5867304	24.48
45	39.971827	-1.5860762	22.328
46	39.9711214	-1.5868986	20.623
47	39.9772468	-1.5843163	27.826
48	39.9674343	-1.5871787	20.925
49	39.9770982	-1.5836772	30.691
50	39.9719599	-1.5842485	22.8
51	39.9691293	-1.5849785	20.976
52	39.9718157	-1.583978	24.72
53	39.9662523	-1.5838537	26.05
54	39.9677222	-1.5865949	20.65
55	39.9536966	-1.5838313	25.975
56	39.9708941	-1.5845982	21.97
57	39.9724453	-1.5845847	20.985
58	39.965408	-1.5860152	20.65
59	39.972376	-1.584299	21.735
60	39.958143	-1.5836978	24.632
61	39.9679384	-1.5844469	22.069
62	39.9725439	-1.5838548	23.665
63	39.9784616	-1.5839114	22.578
64	39.9859415	-1.583475	23.7
65	39.9667089	-1.5830221	24.558
66	39.9746306	-1.5833807	23.942
67	39.9770587	-1.5847622	22.401
68	39.975796	-1.5858035	19.926
69	39.9784232	-1.5823681	28.981
70	39.9706043	-1.5837763	20.937
71	39.9781084	-1.5833181	25.122
72	39.986011	-1.5827699	24.245
73	39.9782711	-1.5819291	29.348
74	39.9656063	-1.5833139	22.905
75	39.9824768	-1.5821761	24.471
76	39.9797127	-1.5815851	26.4
77	39.971618	-1.5821264	21.428
78	39.9695986	-1.5837928	20.431
79	39.9755466	-1.5814459	24.741

80	39.9694609	-1.5813359	24.978
81	39.9650006	-1.581595	23.422
82	39.9773624	-1.5810042	24.278
83	39.9554308	-1.5812367	23.63
84	39.9495924	-1.5817886	21.262
85	39.96847	-1.5811225	24.002
86	39.9672052	-1.5807714	25.346
87	39.9694521	-1.5806058	24.127
88	39.9767939	-1.5808262	23.456
89	39.9743241	-1.5801316	24.906
90	39.9768166	-1.5804807	24.601
91	39.9800647	-1.5822863	22.111
92	39.973228	-1.5803263	24.75
93	39.9747722	-1.5798954	25.947
94	39.9701427	-1.5807502	23.307
95	39.9722132	-1.5803558	22.612
96	39.9609751	-1.5806572	22.395
97	39.9647358	-1.5798438	24.601
98	39.9738205	-1.5808767	22.09
99	39.9735169	-1.5800878	24.599
100	39.9772659	-1.5818986	20.436
101	39.9694165	-1.5793849	24.753
102	39.9552672	-1.5805652	21.67
103	39.9852756	-1.5804749	23.109
104	39.9611777	-1.5793375	24.568
105	39.9759526	-1.5797222	24.787
106	39.9646302	-1.5802852	21.149
107	39.9682985	-1.5794903	23.461
108	39.9569692	-1.5797864	21.398
109	39.9778445	-1.5792368	24.315
110	39.9603365	-1.5788329	25.863
111	39.9781512	-1.5814445	20.863
112	39.9718825	-1.5797615	22.678
113	39.9562052	-1.5791565	23.389
114	39.9631037	-1.5789192	23.025
115	39.9628631	-1.5783976	23.421
116	39.9809016	-1.5794313	21.044
117	39.9680821	-1.5771587	24.287
118	39.9817248	-1.5785983	21.372
119	39.9688455	-1.5780795	22.169
120	39.9808452	-1.5778606	24.25
121	39.9690958	-1.5786935	20.162
122	39.969223	-1.5770271	23.2
123	39.9858374	-1.5766658	24.547
124	39.9637815	-1.581047	20.128

125	39.9616248	-1.5767659	23.848
126	39.974153	-1.5762772	24.717
127	39.96625	-1.5765057	24.588
128	39.9624068	-1.5764117	24.245
129	39.9851132	-1.5757614	24.688
130	39.9556722	-1.5764114	22.805
131	39.9779802	-1.5758738	24.738
132	39.9632027	-1.575432	27.095
133	39.971331	-1.5822411	20.701
134	39.9712028	-1.5758322	24.116
135	39.9813531	-1.5758612	23.974
136	39.970177	-1.5763075	22.713
137	39.9689394	-1.5758116	24.886
138	39.973887	-1.5764173	22.492
139	39.9743939	-1.575279	24.66
140	39.9751467	-1.5768685	20.676
141	39.976727	-1.5748469	26.909
142	39.9653516	-1.5760308	21.287
143	39.9635904	-1.5750733	24.217
144	39.9731389	-1.5768843	21.449
145	39.9570586	-1.5761366	23.61
146	39.9885808	-1.5747058	23.892
147	39.9587721	-1.5748861	24.27
148	39.9758794	-1.5759121	21.775
149	39.9774471	-1.5764461	20.762
150	39.9831395	-1.5749326	23.546
151	39.977867	-1.5779523	20.798
152	39.978919	-1.5750433	21.989
153	39.981875	-1.5746868	24.2
154	39.9680788	-1.5756368	21.103
155	39.9845156	-1.5763576	20.181
156	39.9748005	-1.5749181	22.135
157	39.9865589	-1.5744439	22.744
158	39.9649673	-1.5755956	21.108
159	39.9669955	-1.5735257	24.865
160	39.9704965	-1.5748791	21.469
161	39.9732552	-1.5735651	24.103
162	39.9643723	-1.5733935	24.929
163	39.9775667	-1.5741989	21.272
164	39.9735622	-1.5743247	22.298
165	39.9684041	-1.5746842	20.539
166	39.9726989	-1.5731645	24.971
167	39.9718141	-1.5747848	21.341
168	39.9825795	-1.5731738	23.921
169	39.9731035	-1.5755063	20.981

170	39.967648	-1.5733946	22.818
171	39.9783732	-1.5743603	21.303
172	39.9597415	-1.5734068	21.267
173	39.9819225	-1.5721741	24.172
174	39.9782538	-1.5718363	24.613
175	39.9780282	-1.5732565	21.757
176	39.9768464	-1.5721164	23.258
177	39.9779644	-1.5716044	23.428
178	39.9883804	-1.5717646	24.176
179	39.9743213	-1.5732464	21.077
180	39.9694032	-1.5736471	20.515
181	39.9882503	-1.5723899	21.858
182	39.9875212	-1.5713428	23.72
183	39.9531681	-1.576023	19.83
184	39.9699388	-1.5713551	24.346
185	39.9610231	-1.572007	21.331
186	39.9819802	-1.5712693	24.294
187	39.9718173	-1.5709613	24.601
188	39.9712886	-1.5709686	23.123
189	39.9708659	-1.5726849	20.564
190	39.9659303	-1.5707292	24.162
191	39.9849011	-1.5748287	19.866
192	39.9628481	-1.5711688	23.923
193	39.9681389	-1.571104	23.113
194	39.9749677	-1.5701802	26.475
195	39.9650572	-1.5713528	20.356
196	39.9813243	-1.5727703	20.528
197	39.9642865	-1.57245	20.873
198	39.9660005	-1.5721155	20.052
199	39.9856146	-1.5708541	22.608
200	39.9655219	-1.5702204	24.698
201	39.989152	-1.5695247	25.778
202	39.9658333	-1.5710638	21.961
203	39.9817972	-1.5708696	21.287
204	39.9756789	-1.5697542	24.224
205	39.9586115	-1.5709409	20.628
206	39.9824436	-1.5721775	20.03
207	39.9729981	-1.56907	24.675
208	39.9649582	-1.5709484	21.892
209	39.9811764	-1.5689598	23.179
210	39.9902296	-1.5699798	21.592
211	39.9673448	-1.569726	21.532
212	39.9708675	-1.5684019	25.037
213	39.9557974	-1.5683276	22.986
214	39.9824416	-1.5683801	22.871

215	39.9654712	-1.5678004	23.602
216	39.983182	-1.5673346	23.671
217	39.9728372	-1.5677093	22.972
218	39.9827542	-1.5676315	22.696
219	39.9722158	-1.5684379	21.997
220	39.9696999	-1.5719049	19.826
221	39.9787615	-1.5666667	24.285
222	39.9705958	-1.5692733	20.797
223	39.9769335	-1.566542	22.568
224	39.9741393	-1.5651108	28.963
225	39.9615516	-1.5668084	23.136
226	39.9709465	-1.5655008	24.663
227	39.9729881	-1.5658651	24.044
228	39.9756083	-1.5667255	22.026
229	39.9791208	-1.5654461	26.077
230	39.974223	-1.5650313	27.004
231	39.9640481	-1.566449	21.818
232	39.9670079	-1.5655307	23.928
233	39.9711046	-1.5660463	21.527
234	39.9805115	-1.5682444	19.94
235	39.980309	-1.5686209	23.497
236	39.9588935	-1.5648211	23.707
237	39.9705715	-1.5653061	21.896
238	39.9759107	-1.5638866	23.271
239	39.9760446	-1.5640082	24.269
240	39.9848719	-1.5666483	20.415
241	39.9671256	-1.5642296	23.287
242	39.9664009	-1.5641007	24.13
243	39.96319	-1.5657814	20.465
244	39.9751562	-1.5644394	21.122
245	39.9607916	-1.5646446	21.406
246	39.9621378	-1.5626678	26.036
247	39.9650028	-1.5640131	21.708
248	39.9621672	-1.5629825	22.59
249	39.9705602	-1.56425	21.442
250	39.9776764	-1.562876	23.65
251	39.9647728	-1.5630615	22.485
252	39.9803883	-1.5643114	20.811
253	39.9782752	-1.562535	24.486
254	39.9572418	-1.5655825	19.938
255	39.9753053	-1.5625135	22.785
256	39.9718599	-1.5621317	24.653
257	39.9698979	-1.5632515	21.606
258	39.9688402	-1.5621561	20.485
259	39.9776418	-1.5653814	20.017

260	39.9759698	-1.5611777	24.639
261	39.9737045	-1.56145	25.73
262	39.9768738	-1.5618034	23.059
263	39.9756319	-1.5613471	22.903
264	39.9759957	-1.563567	20.439
265	39.9786718	-1.5618837	22.795
266	39.9636053	-1.5534928	21.457
267	39.9680822	-1.554542	20.993
268	39.9658197	-1.5550311	24.527
269	39.9671651	-1.5568319	21.389
270	39.9709524	-1.5573456	24.178
271	39.9699503	-1.5578908	24.25
272	39.9769185	-1.5600968	20.74
273	39.97363	-1.5597456	24.734
274	39.9617282	-1.5606504	22.738
275	39.9688904	-1.5615736	20.432
276	39.9648898	-1.5615815	20.046
277	39.9613753	-1.5617568	20.712
278	39.975287	-1.5594756	26.267
279	39.9626138	-1.5625381	20.805
280	39.9618908	-1.5647394	19.793

Bibliography

8

Adams, Nathan J., Christopher J. Conselice, Duncan Austin, *et al.* (Apr. 2023). „EPOCHS Paper II: The Ultraviolet Luminosity Function from $7.5 < z < 13.5$ using 110 square arcminutes of deep, blank-field data from the PEARLS Survey and Public Science Programmes“. In: *arXiv e-prints*, arXiv:2304.13721, arXiv:2304.13721. arXiv: 2304.13721 [astro-ph.GA].

Allingham, Joseph F. V., Mathilde Jauzac, David J. Lagattuta, Guillaume Mahler, Céline Bœhm, Geraint F. Lewis, Dominique Eckert, Alastair Edge, and Stefano Ettori (June 2023). „Joint HST, VLT/MUSE, and XMM-Newton observations to constrain the mass distribution of the two strong lensing galaxy clusters: MACS J0242.5-2132 and MACS J0949.8+1708“. In: 522.1, pp. 1118–1137. arXiv: 2207.10520 [astro-ph.CO].

Arrabal Haro, Pablo, Mark Dickinson, Steven L. Finkelstein, *et al.* (Mar. 2023). „Spectroscopic verification of very luminous galaxy candidates in the early universe“. In: *arXiv e-prints*, arXiv:2303.15431, arXiv:2303.15431. arXiv: 2303.15431 [astro-ph.GA].

Atek, Hakim, Iryna Chemerynska, Bingjie Wang, *et al.* (May 2023). „JWST UNCOVER: Discovery of $z > 9$ Galaxy Candidates Behind the Lensing Cluster Abell 2744“. In: *arXiv e-prints*, arXiv:2305.01793, arXiv:2305.01793. arXiv: 2305.01793 [astro-ph.GA].

Bouwens, R. J., G. Illingworth, R. S. Ellis, P. Oesch, and M. Stefanon (Nov. 2022). „z 2-9 Galaxies Magnified by the Hubble Frontier Field Clusters. II. Luminosity Functions and Constraints on a Faint-end Turnover“. In: 940.1, 55, p. 55. arXiv: 2205.11526 [astro-ph.GA].

Bradač, Maruša, Douglas Clowe, Anthony H. Gonzalez, Phil Marshall, William Forman, Christine Jones, Maxim Markevitch, Scott Randall, Tim Schrabback, and Dennis Zaritsky (Dec. 2006). „Strong and Weak Lensing United. III. Measuring the Mass Distribution of the Merging Galaxy Cluster 1ES 0657-558“. In: 652.2, pp. 937–947. arXiv: astro-ph/0608408 [astro-ph].

Brammer, Gabriel (Mar. 2023). *grizli*. Version 1.8.3. Please cite this software using these metadata.

Bruzual, G. and S. Charlot (Oct. 2003). „Stellar population synthesis at the resolution of 2003“. In: 344.4, pp. 1000–1028. arXiv: astro-ph/0309134 [astro-ph].

Buchner, J., A. Georgakakis, K. Nandra, L. Hsu, C. Rangel, M. Brightman, A. Merloni, M. Salvato, J. Donley, and D. Kocevski (Apr. 2014). „X-ray spectral modelling of the AGN obscuring region in the CDFS: Bayesian model selection and catalogue“. In: 564, A125, A125. arXiv: 1402.0004 [astro-ph.HE].

Byler, Nell, Julianne J. Dalcanton, Charlie Conroy, and Benjamin D. Johnson (May 2017). „Nebular Continuum and Line Emission in Stellar Population Synthesis Models“. In: 840.1, 44, p. 44. arXiv: 1611.08305 [astro-ph.GA].

Cain, Benjamin, Paul L. Schechter, and M. W. Bautz (July 2011). „Measuring Gravitational Lensing Flexion in A1689 Using an Analytic Image Model“. In: 736.1, 43, p. 43. arXiv: 1103.0551 [astro-ph.CO].

Calzetti, Daniela, Lee Armus, Ralph C. Bohlin, Anne L. Kinney, Jan Koornneef, and Thaisa Storchi-Bergmann (Apr. 2000). „The Dust Content and Opacity of Actively Star-forming Galaxies“. In: 533.2, pp. 682–695. arXiv: astro-ph/9911459 [astro-ph].

Carnall, A. C., R. J. McLure, J. S. Dunlop, and R. Davé (Nov. 2018). „Inferring the star formation histories of massive quiescent galaxies with BAGPIPES: evidence for multiple quenching mechanisms“. In: 480.4, pp. 4379–4401. arXiv: 1712.04452 [astro-ph.GA].

Carnall, Adam C., Joel Leja, Benjamin D. Johnson, Ross J. McLure, James S. Dunlop, and Charlie Conroy (Mar. 2019). „How to Measure Galaxy Star Formation Histories. I. Parametric Models“. In: 873.1, 44, p. 44. arXiv: 1811.03635 [astro-ph.GA].

Clowe, Douglas, Maruš a Bradač, Anthony H. Gonzalez, Maxim Markevitch, Scott W. Randall, Christine Jones, and Dennis Zaritsky (Aug. 2006). „A Direct Empirical Proof of the Existence of Dark Matter“. In: *The Astrophysical Journal* 648.2, pp. L109–L113.

Clowe, Douglas, Anthony Gonzalez, and Maxim Markevitch (Apr. 2004). „Weak-Lensing Mass Reconstruction of the Interacting Cluster 1E 0657-558: Direct Evidence for the Existence of Dark Matter“. In: *The Astrophysical Journal* 604.2, pp. 596–603.

Conroy, Charlie and James E. Gunn (Apr. 2010). „The Propagation of Uncertainties in Stellar Population Synthesis Modeling. III. Model Calibration, Comparison, and Evaluation“. In: 712.2, pp. 833–857. arXiv: 0911.3151 [astro-ph.CO].

Conroy, Charlie, James E. Gunn, and Martin White (July 2009). „The Propagation of Uncertainties in Stellar Population Synthesis Modeling. I. The Relevance of Uncertain Aspects of Stellar Evolution and the Initial Mass Function to the Derived Physical Properties of Galaxies“. In: 699.1, pp. 486–506. arXiv: 0809.4261 [astro-ph].

Diego, J. M., P. Protopapas, H. B. Sandvik, and M. Tegmark (June 2005). „Non-parametric inversion of strong lensing systems“. In: 360.2, pp. 477–491. arXiv: astro-ph/0408418 [astro-ph].

Diego, Jose M., Kasper B. Schmidt, Tom Broadhurst, *et al.* (Feb. 2018). „A free-form lensing model of A370 revealing stellar mass dominated BCGs, in Hubble Frontier Fields images“. In: 473.4, pp. 4279–4296. arXiv: 1609.04822 [astro-ph.GA].

Doyon, René, John B. Hutchings, Mathilde Beaulieu, *et al.* (Sept. 2012). „The JWST Fine Guidance Sensor (FGS) and Near-Infrared Imager and Slitless Spectrograph (NIRISS)“. In: *Space Telescopes and Instrumentation 2012: Optical, Infrared, and Millimeter Wave*. Ed. by Mark C. Clampin, Giovanni G. Fazio, Howard A. MacEwen, and Jr. Oschmann Jacobus M. Vol. 8442. Society of Photo-Optical Instrumentation Engineers (SPIE) Conference Series, 84422R, 84422R.

Einstein, Albert (Dec. 1936). „Lens-like action of a star by the deviation of light in the gravitational field“. In: *Science* 84.2188, pp. 506–507.

Eldridge, Jan J. and Elizabeth R. Stanway (Aug. 2022). „New Insights into the Evolution of Massive Stars and Their Effects on Our Understanding of Early Galaxies“. In: 60, pp. 455–494. arXiv: 2202.01413 [astro-ph.GA].

Feroz, F. and M. P. Hobson (Jan. 2008). „Multimodal nested sampling: an efficient and robust alternative to Markov Chain Monte Carlo methods for astronomical data analyses“. In: *Monthly Notices of the Royal Astronomical Society* 384.2, pp. 449–463. eprint: https://academic.oup.com/mnras/article-pdf/384/2/449/3378518/mnras0384-0449.pdf.

Fujimoto, Seiji, Steven L. Finkelstein, Denis Burgarella, *et al.* (Nov. 2022). „ALMA FIR View of Ultra High-redshift Galaxy Candidates at $z \sim$ 11-17: Blue Monsters or Low-z Red Interlopers?“ In: *arXiv e-prints*, arXiv:2211.03896, arXiv:2211.03896. arXiv: 2211.03896 [astro-ph.GA].

Grillo, C., S. H. Suyu, P. Rosati, *et al.* (Feb. 2015). „CLASH-VLT: Insights on the Mass Substructures in the Frontier Fields Cluster MACS J0416.1-2403 through Accurate Strong Lens Modeling“. In: 800.1, 38, p. 38. arXiv: 1407.7866 [astro-ph.CO].

Harikane, Yuichi, Masami Ouchi, Masamune Oguri, Yoshiaki Ono, Kimihiko Nakajima, Yuki Isobe, Hiroya Umeda, Ken Mawatari, and Yechi Zhang (Mar. 2023). „A Comprehensive Study of Galaxies at z 9-16 Found in the Early JWST Data: Ultraviolet Luminosity Functions and Cosmic Star Formation History at the Pre-reionization Epoch“. In: 265.1, 5, p. 5. arXiv: 2208.01612 [astro-ph.GA].

Inoue, Akio K., Ikkoh Shimizu, Ikuru Iwata, and Masayuki Tanaka (Aug. 2014). „An updated analytic model for attenuation by the intergalactic medium“. In: 442.2, pp. 1805–1820. arXiv: 1402.0677 [astro-ph.CO].

Iyer, Kartheik G., Eric Gawiser, Sandra M. Faber, Henry C. Ferguson, Jeyhan Kartaltepe, Anton M. Koekemoer, Camilla Pacifici, and Rachel S. Somerville (July 2019). „Nonparametric Star Formation History Reconstruction with Gaussian Processes. I. Counting Major Episodes of Star Formation“. In: 879.2, 116, p. 116. arXiv: 1901.02877 [astro-ph.GA].

Jakobsen, P., P. Ferruit, C. Alves de Oliveira, *et al.* (May 2022). „The Near-Infrared Spectrograph (NIRSpec) on theiJames Webb/iSpace Telescope“. In: *Astronomy &amp Astrophysics* 661, A80.

Johnson, Traci L. and Keren Sharon (Nov. 2016). „The Systematics of Strong Lens Modeling Quantified: The Effects of Constraint Selection and Redshift Information on Magnification, Mass, and Multiple Image Predictability“. In: 832.1, 82, p. 82. arXiv: 1608.08713 [astro-ph.CO].

Jullo, E. and J. -P. Kneib (May 2009). „Multiscale cluster lens mass mapping - I. Strong lensing modelling“. In: 395.3, pp. 1319–1332. arXiv: 0901.3792 [astro-ph.CO].

Jullo, E., J. -P. Kneib, M. Limousin, Á. Elıasdóttir, P. J. Marshall, and T. Verdugo (Dec. 2007). „A Bayesian approach to strong lensing modelling of galaxy clusters“. In: *New Journal of Physics* 9.12, p. 447. arXiv: 0706.0048 [astro-ph].

JWST User Documentation (Nov. 2022).

Kassiola, Aggeliki and Israel Kovner (Nov. 1993). „Elliptic Mass Distributions versus Elliptic Potentials in Gravitational Lenses“. In: 417, p. 450.

Kawamata, Ryota, Masamune Oguri, Masafumi Ishigaki, Kazuhiro Shimasaku, and Masami Ouchi (Mar. 2016). „Precise Strong Lensing Mass Modeling of Four Hubble Frontier Field Clusters and a Sample of Magnified High-redshift Galaxies“. In: 819.2, 114, p. 114. arXiv: 1510.06400 [astro-ph.GA].

Kneib, J. -P., R. S. Ellis, I. Smail, W. J. Couch, and R. M. Sharples (Nov. 1996). „Hubble Space Telescope Observations of the Lensing Cluster Abell 2218“. In: 471, p. 643. arXiv: astro-ph/9511015 [astro-ph].

Kneib, J. -P., Y. Mellier, B. Fort, and G. Mathez (June 1993). „The distribution of dark matter in distant cluster-lenses : modelling modelling A 370.“ In: 273, p. 367.

Kroupa, P. and C. M. Boily (Nov. 2002). „On the mass function of star clusters“. In: 336.4, pp. 1188–1194. arXiv: astro-ph/0207514 [astro-ph].

Lagattuta, David J, Johan Richard, Franz E Bauer, *et al.* (Mar. 2019). „Probing 3D Structure with a Large MUSE Mosaic: Extending the Mass Model of Frontier Field Abell 370“. In: *Monthly Notices of the Royal Astronomical Society*.

Lagattuta, David J., Johan Richard, Benjamin Clément, *et al.* (Aug. 2017). „Lens modelling Abell 370: crowning the final frontier field with MUSE“. In: 469.4, pp. 3946–3964. arXiv: 1611.01513 [astro-ph.GA].

Limousin, Marceau, Jean-Paul Kneib, and Priyamvada Natarajan (Jan. 2005). „Constraining the mass distribution of galaxies using galaxy-galaxy lensing in clusters and in the field“. In: 356.1, pp. 309–322. arXiv: astro-ph/0405607 [astro-ph].

Limousin, Marceau, Johan Richard, Eric Jullo, *et al.* (Oct. 2007). „Combining Strong and Weak Gravitational Lensing in Abell 1689“. In: 668.2, pp. 643–666. arXiv: astro-ph/0612165 [astro-ph].

Livermore, R. C., T. A. Jones, J. Richard, *et al.* (June 2015). „Resolved spectroscopy of gravitationally lensed galaxies: global dynamics and star-forming clumps on $\sim$100 pc scales at $1 < z < 4$“. In: 450.2, pp. 1812–1835. arXiv: 1503.07873 [astro-ph.GA].

Lotz, J. M., A. Koekemoer, D. Coe, *et al.* (Mar. 2017). „The Frontier Fields: Survey Design and Initial Results“. In: 837.1, 97, p. 97. arXiv: 1605.06567 [astro-ph.GA].

Ma, Xiangcheng, Philip F. Hopkins, Shea Garrison-Kimmel, Claude-André Faucher-Giguère, Eliot Quataert, Michael Boylan-Kolchin, Christopher C. Hayward, Robert Feldmann, and Dušan Kereš (Aug. 2018). „Simulating galaxies in the reionization era with FIRE-2: galaxy scaling relations, stellar mass functions, and luminosity functions“. In: 478.2, pp. 1694–1715. arXiv: 1706.06605 [astro-ph.GA].

Mahler, Guillaume, Mathilde Jauzac, Johan Richard, *et al.* (Mar. 2023). „Precision Modeling of JWST's First Cluster Lens SMACS J0723.3-7327“. In: 945.1, 49, p. 49. arXiv: 2207.07101 [astro-ph.GA].

Markevitch, M. (Jan. 2006). „Chandra Observation of the Most Interesting Cluster in the Universe“. In: *The X-ray Universe 2005*. Ed. by A. Wilson. Vol. 604. ESA Special Publication, p. 723. arXiv: astro-ph/0511345 [astro-ph].

Markov, V., S. Gallerani, A. Pallottini, L. Sommovigo, S. Carniani, A. Ferrara, E. Parlanti, and F. Di Mascia (Apr. 2023). „Dust attenuation law in JWST galaxies at z = 7-8“. In: *arXiv e-prints*, arXiv:2304.11178, arXiv:2304.11178. arXiv: 2304.11178 [astro-ph.GA].

Mason, Charlotte A., Tommaso Treu, Adriano Fontana, *et al.* (Mar. 2017). „First Results from the KMOS Lens-Amplified Spectroscopic Survey (KLASS): Kinematics of Lensed Galaxies at Cosmic Noon“. In: 838.1, 14, p. 14. arXiv: 1610.03075 [astro-ph.GA].

Matharu, Jasleen, Casey Papovich, Raymond C. Simons, *et al.* (Sept. 2022). „CLEAR: The Evolution of Spatially Resolved Star Formation in Galaxies between 0.5 z 1.7 Using Hα Emission Line Maps“. In: 937.1, 16, p. 16. arXiv: 2205.08543 [astro-ph.GA].

Michell, John (1784). „VII. On the means of discovering the distance, magnitude, &c. of the fixed stars, in consequence of the diminution of the velocity of their light, in case such a diminution should be found to take place in any of them, and such other data should be procured from observations, as would be farther necessary for that purpose. By the Rev. John Michell, B.D. F.R.S. In a letter to Henry Cavendish, Esq. F.R.S. and A.S“. In: *Philosophical Transactions of the Royal Society of London* 74, pp. 35–57. eprint: https://royalsocietypublishing.org/doi/pdf/10.1098/rstl.1784.0008.

Molnar, Sandor M., Shutaro Ueda, and Keiichi Umetsu (Sept. 2020). „The Dynamical State of the Frontier Fields Galaxy Cluster Abell 370“. In: 900.2, 151, p. 151. arXiv: 2005.03212 [astro-ph.CO].

Oguri, Masamune (Oct. 2010). *glafic: Software Package for Analyzing Gravitational Lensing*. Astrophysics Source Code Library, record ascl:1010.012. ascl: 1010.012.

Papovich, Casey, Mark Dickinson, and Henry C. Ferguson (Oct. 2001). „The Stellar Populations and Evolution of Lyman Break Galaxies“. In: 559.2, pp. 620–653. arXiv: astro-ph/0105087 [astro-ph].

Richard, Johan, Adélaıde Claeyssens, David Lagattuta, *et al.* (Feb. 2021). „An atlas of MUSE observations towards twelve massive lensing clusters“. In: 646, A83, A83. arXiv: 2009.09784 [astro-ph.GA].

Rieke, G. H., G. S. Wright, T. Böker, *et al.* (July 2015). „The Mid-Infrared Instrument for the James Webb Space Telescope, I: Introduction“. In: *Publications of the Astronomical Society of the Pacific* 127.953, p. 584.

Rieke, Marcia J., Douglas Kelly, and Scott Horner (Aug. 2005). „Overview of James Webb Space Telescope and NIRCam's Role“. In: *Cryogenic Optical Systems and Instruments XI*. Ed. by James B. Heaney and Lawrence G. Burri-

esci. Vol. 5904. Society of Photo-Optical Instrumentation Engineers (SPIE) Conference Series, pp. 1–8.

Saha, Prasenjit, Justin I. Read, and Liliya L. R. Williams (Nov. 2006). „Two Strong-Lensing Clusters Confront Universal Dark Matter Profiles“. In: 652.1, pp. L5–L8. arXiv: astro-ph/0610011 [astro-ph].

Salim, Samir, Médéric Boquien, and Janice C. Lee (May 2018). „Dust Attenuation Curves in the Local Universe: Demographics and New Laws for Star-forming Galaxies and High-redshift Analogs“. In: 859.1, 11, p. 11. arXiv: 1804.05850 [astro-ph.GA].

Salpeter, Edwin E. (Jan. 1955). „The Luminosity Function and Stellar Evolution.“ In: 121, p. 161.

Scalo, J. M. (Jan. 1986). „The initial mass function of massive stars in galaxies Empirical evidence“. In: *Luminous Stars and Associations in Galaxies*. Ed. by C. W. H. De Loore, A. J. Willis, and P. Laskarides. Vol. 116, pp. 451–466.

Schneider, Peter (2006). *Extragalactic Astronomy and Cosmology*. Berlin, Heidelberg: Springer Berlin Heidelberg.

Schneider, Peter, Christopher S. Kochanek, and Joachim Wambsganss (2006). *Gravitational Lensing: Strong, Weak and Micro*. Springer.

Simons, Raymond C., Casey Papovich, Ivelina Momcheva, *et al.* (Dec. 2021). „CLEAR: The Gas-phase Metallicity Gradients of Star-forming Galaxies at 0.6 $<$ z $<$ 2.6“. In: 923.2, 203, p. 203. arXiv: 2011.03553 [astro-ph.GA].

Simons, Raymond C., Casey Papovich, Ivelina G. Momcheva, *et al.* (Mar. 2023). „CLEAR: Survey Overview, Data Analysis and Products“. In: *arXiv e-prints*, arXiv:2303.09570, arXiv:2303.09570. arXiv: 2303.09570 [astro-ph.GA].

Soucail, G., Y. Mellier, B. Fort, G. Mathez, and M. Cailloux (Feb. 1988). „The giant arc in A 370 : spectroscopic evidence for gravitational lensing from a source at Z=0.724.“ In: 191, pp. L19–L21.

Strait, V., M. Bradač, A. Hoag, *et al.* (Dec. 2018). „Mass and Light of Abell 370: A Strong and Weak Lensing Analysis“. In: 868.2, 129, p. 129. arXiv: 1805.08789 [astro-ph.GA].

Strait, Victoria, Maruša Bradač, Dan Coe, *et al.* (Apr. 2021). „RELICS: Properties of z $\geq$ 5.5 Galaxies Inferred from Spitzer and Hubble Imaging, Including A Candidate z $\sim$ 6.8 Strong [O III] emitter“. In: 910.2, 135, p. 135. arXiv: 2009.00020 [astro-ph.GA].

Umetsu, Keiichi, Tom Broadhurst, Adi Zitrin, Elinor Medezinski, and Li-Yen Hsu (Mar. 2011). „Cluster Mass Profiles from a Bayesian Analysis of Weak-lensing Distortion and Magnification Measurements: Applications to Subaru Data“. In: 729.2, 127, p. 127. arXiv: 1011.3044 [astro-ph.CO].

Umetsu, Keiichi, Shutaro Ueda, Bau-Ching Hsieh, Mario Nonino, I. -Non Chiu, Masamune Oguri, Sandor M. Molnar, Anton M. Koekemoer, and Sut-Ieng Tam (Aug. 2022). „Line-of-sight Elongation and Hydrostatic Mass Bias of the Frontier Fields Galaxy Cluster Abell 370“. In: 934.2, 169, p. 169. arXiv: 2203.03647 [astro-ph.CO].

Walsh, D., R. F. Carswell, and R. J. Weymann (1979). „0957 + 561 A, b: Twin quasistellar objects or gravitational lens?“ In: *Nature* 279.5712, pp. 381–384.

Willott, Chris J., René Doyon, Loic Albert, *et al.* (Feb. 2022). „The Near-infrared Imager and Slitless Spectrograph for the James Webb Space Telescope. II. Wide Field Slitless Spectroscopy“. In: 134.1032, 025002, p. 025002. arXiv: 2202.01714 [astro-ph.IM].

Young, P., J. E. Gunn, J. B. Oke, J. A. Westphal, and J. Kristian (Feb. 1988). „The double quasar Q0957 + 561 A, B - a gravitational lens image formed by a galaxy at Z = 0.39“. In: *Astronomy and Astrophysics* 191, p. 507.

Zwicky, F. (1937a). „Nebulae as gravitational lenses“. In: *Physical Review* 51.4, pp. 290–290.

Zwicky, F. (1937b). „On the masses of nebulae and of clusters of nebulae“. In: *The Astrophysical Journal* 86, p. 217.